Effect of domain walls in bilayer graphene in an external magnetic field

Master's Thesis in Physics

Presented by

Nico S. Baßler

13th March, 2020

Institut für Theoretische Physik
Friedrich-Alexander-Universität Erlangen-Nürnberg

Supervisor:
Prof. Dr. Kai P. Schmidt

Abstract

In this thesis, I investigate two-dimensional quantum materials, in particular bilayer graphene systems with layer switching defects, in the presence of an external magnetic field. One method of investigation is by calculating quantum transport and local densities of the systems with recursive Green's function methods. Another is by calculating topological invariants either directly or with local index methods. The theoretical framework for both is developed and different implementations are discussed. Only the transport calculations are performed for the bilayer graphene systems, since the systems in question are too large for topological invariant calculations discussed here.

The effect of linear defects in the integer quantum Hall effects (IQHEs) depends on the particular geometry of the defect. For a defect due to shearing of the upper graphene layer there is plateau formation in the magnetoconductance for large defect regions. For a defect due to tension in the upper graphene layer, there is approximate plateau formation for large defect sizes, with fluctuations of the order σ_0. A direct transition between stacking regions, here called a hard wall model, shows no plateau formation and is not a good model for either of the previously mentioned defects.

Acronyms

BLG bilayer graphene.

HLSW hard wall layer switching wall.

IQHE integer quantum Hall effect.

LDOS local density of states.

LSW layer switching wall.

SLSW shear layer switching wall.

SSH Su Schrieffer Heeger.

TBLG twisted bilayer graphene.

TEM transmission electron microscopy.

TLSW tension layer switching wall.

Contents

Chapter 1

Introduction

Research on Van der Waals heterostructures and other two-dimensional materials has been popular and of great interest in recent years. This is in part due to improvements in the reliability and flexibility in the manufacturing processes of these materials. Another part to this surge of interest is the rich theory of topological insulators [1, 2], which predicts exotic physics in many two-dimensional quantum systems.

One material at the center of both these revolutions has been graphene [3]. It was one of the first materials to be recognized as a two-dimensional topological insulator, although a too weak one [4]. It also was graphene, that spawned interest in the production methods of other two-dimensional materials.

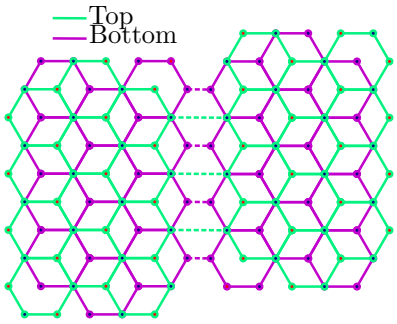

Figure 1.1: Here are two regions of Bernal stacked bilayer graphene (BLG), which are rotated about 180° with respect to each other. There is now AB-stacked graphene on the left and BA-stacked graphene on the right connected by hopping terms. The top layer is green and the bottom layer is magenta.

In particular, the research of bilayer graphene is still an ongoing topic [5, 6] with the recent discovery of anomalous superconductivity of bilayer graphene at certain magic twist angles [7, 8]. The inspiration for this thesis, however, are the properties of domain walls between bilayer graphene materials. The domain walls of interest are domain walls between the two energetically equivalent realizations of the energetically favoured Bernal stacking. A hard wall model for such a domain wall is shown in Figure 1.1. Just as in the Su Schrieffer Heeger (SSH) model [9], this domain wall implies interesting physical properties. In [10], the existence of topologically protected modes propagating along such a domain wall are explored, if an external electric field is applied.

These domain walls naturally form in epitaxially grown bilayer graphene shown in Figure 1.2 leading to a so called mosaic tiling of bilayer graphene. The transport through such networks is of experimental interest, since these naturally appearing defects have very interesting physical properties. In an external electric field, the domain walls between AB and BA stacked graphene lead to topological transport networks, which can be observed experimentally for twisted bilayer

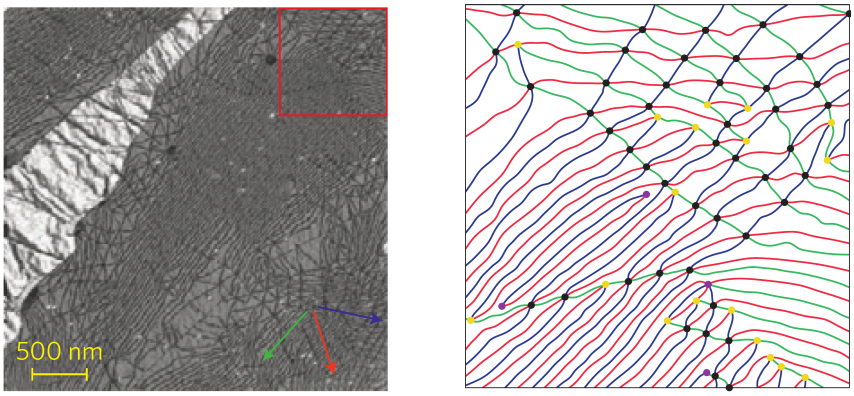

Figure 1.2: Left image: Partial dislocation network in a bilayer membrane originating from epitaxial graphene on SiC(0001). The image shows a composite (or superposition) of three dark-field transmission electron microscopy (TEM) images, taken with the three {1120} reflections, such that the full network of partial dislocations is revealed, providing the mosaic tiling of bilayer graphene. Right image: Partial dislocation network in which the color encodes the crystallographic Burgers vector associated with the partial dislocations as extracted from the individual dark-field TEM data (red square on the left). Extracted including caption from [11].

graphene [12].

The question, that this thesis tries to answer is how the existence of an external magnetic field affects these domain walls or in turn, how these domain walls affect the anomalous IQHE in bilayer graphene [13, 14]. In contrast to the situation with an external electric field, there is no breaking of symmetry or existence of topological invariants, that predict topological edge modes. Thus it is not obvious, how domain walls and integer quantum Hall modes would interact. In particular, the transport through a bilayer graphene defect network like in Figure 1.2 is of great interest and understanding the problem of transport in such networks is the ultimate goal of this work.

There are two usual strategies for calculating edge modes due to the IQHE. One is by calculating the Chern number of the system and employing the bulk-boundary correspondence between the system and vacuum, ensuring topologically protected edge modes [15–20]. The other is by observing the characteristic conductance plateaus by calculating quantum transport through bilayer graphene systems.

The particular systems for which these calculations are to be performed have very complicated geometry and have to be large to mitigate finite-size effects introduced by the length scale of the external magnetic field. There exist tools for quantum transport calculations like KWANT [21], but none of them are particularly very well suited for the implementation of these complicated geometries and ultimately calculating transport properties and invariants for these systems.

Thus my task was to implement a quantum transport program, that could easily implement these systems and do large scale transport calculations [22–24] and invariant calculations on them. There are several methods for the calculations of invariants and quantum transport for these fairly simple, but large, hopping Hamiltonian systems.

The solutions of the quantum transport system for these types of systems is usually performed by using a variation of a recursive Green's function algorithm [25] or by directly using an appropriate sparse solver [21]. Different implementations of these techniques are appropriate

for particular system geometries and in the case of IQHE measurements a very generic solution should be applied.

For invariant calculations there are also a few widely used methods, either involving the calculation of topological invariants by performing Wannier loops [26] or by using theorems about the equivalence of local indices and topological invariants for certain base manifolds and calculating these local indices [27].

The systems ultimately proved too large to perform adequate invariant calculations on with either of the two mentioned methodologies, but the calculation of transport properties was successful.

What follows is a short chapter by chapter preview of the thesis.

First, I will introduce the general transport experiment setup and discuss how Green's functions from nonequilibrium perturbation theory can be used to simulate quantum transport in chapter 2.

In chapter 3 several numerical methods are introduced to facilitate the calculation of the aforementioned Green's functions for large systems. All of these methods seek to split the system into several subsystems and then obtain a total solution from solutions of these partial systems.

To further discuss the IQHE, topological invariants are introduced and in particular the Chern number is discussed in chapter 4. This chapter also includes a more in-depth look into the physics of electrons in an external magnetic field and the stability and regime of the IQHE. In chapter 5 two popular methods for the numerical calculation of the Chern number are introduced. The Wannier charge center method and the Bott index method.

To test both the implementation of the transport calculation and the topological invariant calculation, the Haldane model is introduced in chapter 6 as an analytically solvable model, that still exhibits a topologically nontrivial electronic structure.

Since the discussion of bilayer graphene (BLG) systems with layer switching walls (LSWs) is the ultimate goal of this thesis, a proper background on the material is introduced. First, the electronic properties of single layer graphene with and without external magnetic field are discussed in chapter 7. The same is done for Bernal stacked BLG in chapter 8. In particular the anomalous IQHEs for single and bilayer graphene are introduced and discussed. After that the concept of a LSW for BLG is introduced and a simple hard wall model for it is shown. This chapter also includes a small section about twisted bilayer graphene. More general modelling of hopping integrals for BLG materials is introduced for more complicated BLG geometries.

In chapter 9 all results of calculations for BLG systems are contained. First models of tensile stress and shear stress for a smooth LSW transition are introduced. Then two major simulation setups are shown, a Slab setup and a Hallbar setup and in the following sections are multiple parameter studies for these experimental setups are performed. These parameter studies include transmission and local density of states (LDOS) calculations for select systems.

The specific calculations performed in this chapter are

- Magnetoconductance calculations for every system type.
- A finite size study for various example magnetoconductance calculations.
- A parameter study of numerical interaction cutoff.
- Some magnetoconductance calculations at different Fermi energies to determine the energy dependence of features.
- Parameter studies of further important system parameters (hard wall coupling strength, shear layer switching wall (SLSW) extent, hard wall layer switching wall (HLSW) extent).

and the thesis ends with a concluding summary and outlook.

Chapter 2

Transport Calculation with Green's functions

2.1 The transport experiment

There exist several approaches to calculating quantum transport through a device suited to different sets of problems, but they all describe the same experiment.

Definition 1 (Transport experiment) *A Quantum transport experiment is conducted on a central device/scattering region $\mathcal{D}$ connected to several contacts (leads) at chemical potentials μ_i. It is then the measurement of some quantity due to an applied bias V (encapsulated in the chemical potentials).*

Figure 2.1 and Figure 2.2 are examples for generic transport experiments. I will wall the experiment geometry in Figure 2.1 a **Slab** and the geometry in Figure 2.2 a **Hallbar**.

Figure 2.1: Transport experiment with two terminals to the left and right. For $\mu_1 < \mu_2$ it measures electron transport properties due to an applied voltage $e(\mu_2 - \mu_1)$.

Since a transport experiment is due to the application of an external bias, transport is usually a steady-state nonequilibrium process, even in the zero bias limit. The size of the considered samples is the micrometer regime and the transport experiment is thus a mesoscopic transport experiment, since quantum effects are still very relevant on these length scales, but the system size is much larger than wavelengths of electrons in it.

2.2 Motivation

Since transport is essentially a nonequilibrium problem, a nonequilibrium theory of the system is required to model transport. The main idea is to treat the nonequilibrium interaction as a

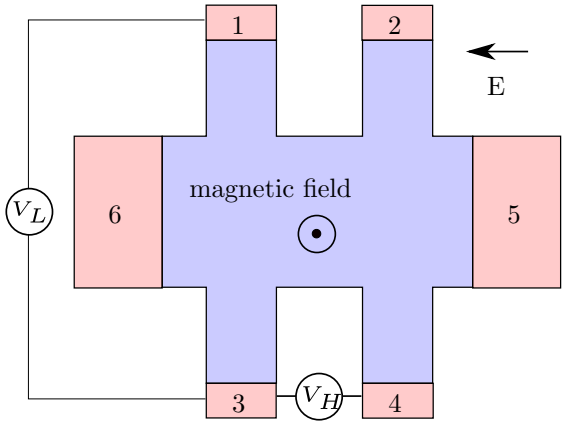

Figure 2.2: Transport experiment with an external magnetic field B. An external bias V is applied between the contacts 6 and 5. The measured quantities are longitudinal voltage V_L and Hall voltage V_H due to the induced chemical potentials at contacts 1,2,3,4.

perturbation to an equilibrium Hamiltonian and use the theory of nonequilibrium perturbation theory to obtain results, i.e. write

$$\mathcal{H} = \mathcal{H}_{\text{equilibrium}} + \mathcal{H}_{\text{nonequilibrium}}. \tag{2.1}$$

There are two canonical choices for $\mathcal{H}_{\text{equilibrium}}$ and $\mathcal{H}_{\text{nonequilibrium}}$:

- $\mathcal{H}_{\text{equilibrium}}$ describes the system, where contacts and scattering region are not coupled and $\mathcal{H}_{\text{nonequilibrium}}$ contains the coupling
- $\mathcal{H}_{\text{equilibrium}}$ describes the system with all leads at the same chemical potential μ and $\mathcal{H}_{\text{nonequilibrium}}$ introduces a bias into the system.

The choice in this thesis will be the first, which is also the most common choice in the literature.

2.3 Equilibrium perturbation theory at $T = 0$

Starting with perturbation theory at $T = 0$ and at equilibrium makes sense when introducing nonequilibrium perturbation theory, since most necessary concepts transfer trivially while complications due to, for example initial correlations are of no concern.

The treatment of many-particle problems was historically very difficult and inaccessible until the methods from quantum field-theory were applied to the problem. There exist many modern strategies of solving many-particle problems, but the most used method is still the simple expansion of the S-Matrix in the appropriate Green's functions and many more advanced methods are based on the concepts, that I will present in the next few pages.

2.3.1 Definition of relevant Green's functions

In the formulation of equilibrium perturbation theory at $T = 0$, six Green's functions are usually defined

Definition 2 (Green's functions in the $T = 0$ equilibrium formalism)

$$\begin{aligned}
G_{\mathrm{ret}}(x_1,t_1,t_2,x_2) &= -i\theta(t_1-t_2)\left\langle\left\{\hat{\psi}(x_1,t_1),\hat{\psi}^\dagger(t_2,x_2)\right\}\right\rangle \\
G_{\mathrm{adv}}(x_1,t_1,t_2,x_2) &= i\theta(t_2-t_1)\left\langle\left\{\hat{\psi}(x_1,t_1),\hat{\psi}^\dagger(t_2,x_2)\right\}\right\rangle \\
G^<(x_1,t_1,t_2,x_2) &= i\left\langle\hat{\psi}(x_1,t_1)\hat{\psi}^\dagger(t_2,x_2)\right\rangle \\
G^>(x_1,t_1,t_2,x_2) &= -i\left\langle\hat{\psi}^\dagger(x_1,t_1)\hat{\psi}(t_2,x_2)\right\rangle \\
G_t(x_1,t_1,t_2,x_2) &= i\left\langle\mathcal{T}\hat{\psi}^\dagger(x_1,t_1)\hat{\psi}(t_2,x_2)\right\rangle \\
G_{\bar{t}}(x_1,t_1,t_2,x_2) &= i\left\langle\bar{\mathcal{T}}\hat{\psi}^\dagger(x_1,t_1)\hat{\psi}(t_2,x_2)\right\rangle
\end{aligned} \tag{2.2}$$

where the time ordering $\mathcal{T}$ and anti-time ordering operator $\bar{\mathcal{T}}$ are defined as

Definition 3 (Time and anti time ordering)

$$\begin{aligned}
\mathcal{T}\left(\hat{A}(t_1)\hat{B}(t_2)\right) &= \begin{cases}\hat{A}(t_1)\hat{B}(t_2) & t_2<t_1\\ \hat{B}(t_1)\hat{A}(t_2) & t_1<t_2\end{cases} \\
\bar{\mathcal{T}}\left(\hat{A}(t_1)\hat{B}(t_2)\right) &= \begin{cases}\hat{B}(t_1)\hat{A}(t_2) & t_2<t_1\\ \hat{A}(t_1)\hat{B}(t_2) & t_1<t_2\end{cases}.
\end{aligned} \tag{2.3}$$

At $T = 0$, the expectation value is defined as

$$\langle\mathcal{A}\rangle_{T=0} = \langle 0|A|0\rangle\,, \tag{2.4}$$

where $|0\rangle$ is the ground state of the system.

G_{ret}, G_{adv}, $G^<$ and $G^>$ are used beyond just the $T = 0$ case, but G_t and $G_{\bar{t}}$ are introduced specifically due to their properties at $T = 0$. Essentially, only four Green's functions are required since

$$\begin{aligned}
G_t(x_1,t_1,t_2,x_2) &= \theta(t_1-t_2)G^>(x_1,t_1,t_2,x_2)+\theta(t_2-t_1)G^<(x_1,t_1,t_2,x_2) \\
G_{\bar{t}}(x_1,t_1,t_2,x_2) &= \theta(t_2-t_1)G^>(x_1,t_1,t_2,x_2)+\theta(t_1-t_2)G^<(x_1,t_1,t_2,x_2)
\end{aligned} \tag{2.5}$$

since the Green's functions are linearly dependent. All six Green's functions have very different physical interpretations, justifying their inclusion:

- Retarded Green's function G_{ret} / Advanced Green's function G_{adv}: Are the retarded and advanced correlation functions of the creation operator. Contains information about spectral properties, densities of states and scattering rates [28].
- Lesser Green's function $G^<$ / Greater Green's function $G^>$: Are related to many observables and the kinetic properties of the system.
- Time ordered Green's function G_t / Anti-time ordered Green's function $G_{\bar{t}}$: Have a simple, systematic perturbation theory.

G_{ret}, $G^<$ and G_t describe electrons and G_{adv}, $G^>$, and $G_{\bar{t}}$ describe holes.
I will be using the short form

$$G(1,2) = G(x_1,t_1,t_2,x_2) \tag{2.6}$$

starting from here.

2.3.2 Perturbation theory of time ordered Green's functions

From now on, the general set-up will be a system Hamiltonian, that is split into a noninteracting part and an interacting part such that

$$\mathcal{H} = \mathcal{H}_0 + \mathcal{H}_{\text{int}} \tag{2.7}$$

and, if not explicitly stated otherwise, the interaction picture will be used, i.e.

$$\begin{aligned} |\psi_I(t)\rangle &= \exp\left(\frac{i}{\hbar}\mathcal{H}_0 t\right)|\psi_S(t)\rangle \\ \hat{A}_I(t) &= \exp\left(\frac{i}{\hbar}\mathcal{H}_0 t\right)\hat{A}_S \exp\left(-\frac{i}{\hbar}\mathcal{H}_0 t\right), \end{aligned} \tag{2.8}$$

where $|\psi_S(t)\rangle$ and $\hat{A}_S$ are state and operator in the Schrödinger picture and $|\psi_I(t)\rangle$ and $\hat{A}_I(t)$ in the interaction picture, respectively. States without subscript are implicitly defined in the interaction picture. The time evolution operator $U(t)$ in the interaction picture can then be written as

$$U(t) = \mathcal{T}\exp\left(-i\int_0^t \mathcal{H}_{\text{int}}(t')\,dt'\right). \tag{2.9}$$

In the discussion of perturbation theory, **adiabatic switch-on** will be relevant and reference to the state $|\psi(-\infty)\rangle$ will be made. This prompts the introduction of the S-Matrix

$$S(t_1,t_2) = \mathcal{T}\exp\left(-i\int_{t_1}^{t_2}\mathcal{H}_{\text{int}}(t)\,dt\right) = \mathcal{U}(t_1)\mathcal{U}^\dagger(t_2), \tag{2.10}$$

which acts on states like

$$|\psi(t_2)\rangle = S(t_1,t_2)\,|\psi(t_1)\rangle\,. \tag{2.11}$$

The precise definition of adiabatic switch-on and the proof for the following statement can be found in [29].

The essential statement is the following: the interaction in the system is zero at $t = -\infty$ and slowly switched on until it is $\mathcal{H}_{\text{int}}$ at $t = 0$. Then, using the S-Matrix corresponding to the switch-on, the following statement

$$|0\rangle_{\text{interacting}} = S(0,-\infty)\,|0\rangle_{\text{noninteracting}} \tag{2.12}$$

is called the **Gell-Mann-Low theorem**, where $|0\rangle$ are the respective ground states. It simply states, that slowly turning on the interaction transforms the noninteracting ground state into the interacting one.

Another required identity is the following

$$\langle 0|_{\text{noninteracting}} = S(\infty,0)\,\langle 0|_{\text{interacting}}\,, \tag{2.13}$$

which assumes, that the interaction is switched off at $t = \infty$. This can only hold true in equilibrium, since interactions are only reversible at equilibrium. Equation 2.12 and Equation 2.13 are inserted into the ground state of the interacting expectation value to rewrite the time-ordered Green's function as

$$G_t(1,2) = \frac{\langle 0|\mathcal{T}S(\infty,-\infty)\hat{\psi}(1)\hat{\psi}^\dagger(2)|0\rangle}{\langle 0|S(\infty,-\infty)|0\rangle} \tag{2.14}$$

such that an expansion of the Green's function may be performed by simply expanding the S-Matrix as an exponential series

$$S(-\infty,\infty) = \sum_{n=0}^{\infty} \frac{(-i)^{n+1}}{n!} \int_{-\infty}^{\infty} dt_1 \dots dt_n \mathcal{T}[\mathcal{H}_{\text{int}}(t_1)\dots\mathcal{H}_{\text{int}}(t_n)]. \tag{2.15}$$

Actually evaluating these expansions will not be of further interest in this thesis, but discussing the general structure of the terms resulting from this expansion will be of use.

Wick's theorem may be used to expand products of many creation and annihilation operators into products of two. These products are two-particle Green's functions and densities, which can be written as Feynman diagrams. All perturbation expansions, that will be discussed from now on allow for an equivalent diagrammatic expansion due to the existence of a Wick's theorem for the expansion of an exponential. As such, many ideas like the Dyson equation are independent of the explicit setting like temperature and equilibrium or nonequilibrium. As a side note, the denominator of the expansion cancels all disconnected diagrams of the numerator and only connected diagrams should be considered in the expansion.

2.3.3 Dyson equation

The Dyson equation is an identity used to re-sum the perturbation expansion automatically. The Dyson equation can be obtained by simply observing, that the existence of a diagram $\mathcal{D}$ implies, that the same diagram glued to itself with a free propagator $\mathcal{D}G_0\mathcal{D}$ exists in a higher order. More explicitly, this is shown in Figure 2.3 for the first order Hartree and Fock diagrams.

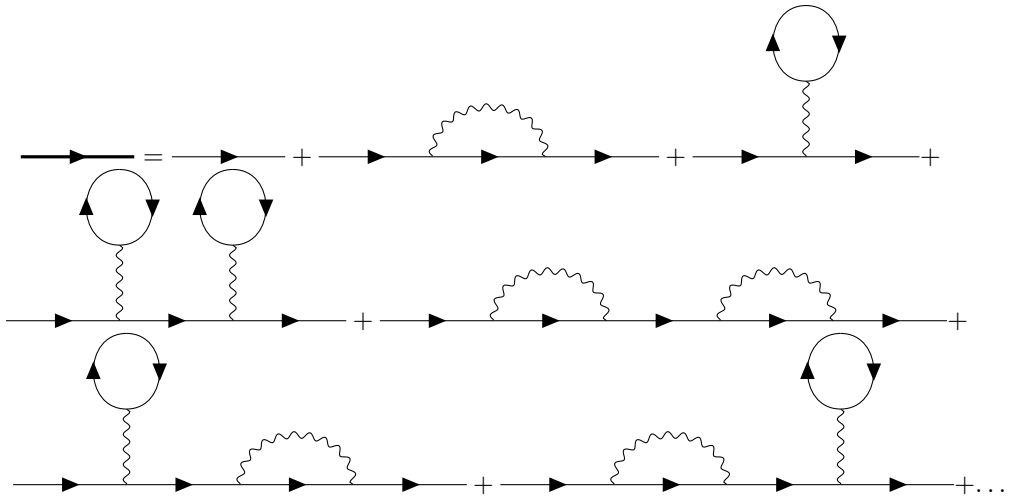

Figure 2.3: Illustration of the Dyson equation

The **proper self-energy** Σ in Figure 2.4 contains all diagrams, that are not disconnected after cutting one connection between vertices. Of course finding the entire self-energy amounts to evaluating the exponential sum to arbitrary order, since diagrams of arbitrary order may appear in the self-energy.

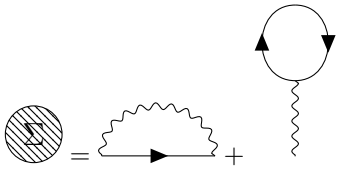

Figure 2.4: Hartree-Fock self energy

As such, approximate self-energies are used for example by choosing a few lower order diagrams such as in Figure 2.4 and using a self-energy comprised of those. However, one must be careful in choosing self-energies, since some cause the violation of conservation laws.

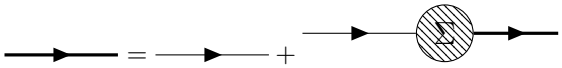

Figure 2.5: Dyson equation in diagrammatic form

Using the proper self-energy, the expansion in Figure 2.4 can be diagramatically rewritten as Figure 2.5, which is a diagrammatic version of the Dyson equation.

Putting the Dyson equation into symbolic formulas from the diagrammatic formulation, one finds

$$\begin{aligned} G &= G_0 + G_0\Sigma G_0 + G_0\Sigma G_0\Sigma G_0 + \ldots = G_0 + G_0\Sigma G \\ G &= \left(G_0^{-1} + \Sigma\right)^{-1}, \end{aligned} \tag{2.16}$$

which will be used extensively in the numerical implementation of the transport calculation. In this case, all Green's functions denoted by G are actually time-ordered Green's functions, but due to the applicability to other perturbation expansions the subscript was intentionally omitted.

2.4 Fluctuation-Dissipation relation

The fluctuation-dissipation theorem is a general concept in physics, that ensures an equation, that relates the fluctuation to the dissipation of some quantity. It is quite general, but for Green's functions is takes the form

$$G^<(\omega) = \eta(\omega)\left[G_{\mathrm{adv}}(\omega) - G_{\mathrm{ret}}(\omega)\right] \sim -2\eta(\omega)\,\mathrm{Im}[G_{\mathrm{ret}}(\omega)], \tag{2.17}$$

since $G^<(\omega)$ is related to the dynamics of the system and $\mathrm{Im}[G_{\mathrm{ret}}(\omega)]$ to the dissipation.

This equality can be shown with the **Lehmann representation** of the Green's function [30] and is also true for self-energies with an analogous proof. It is the first discussed equation, that relates static properties of the system to dynamic properties of the system.

2.5 Equilibrium perturbation theory at $T \neq 0$

The essential difference between $T = 0$ and $T \neq 0$ is the explicit form of the expectation value $\langle \ldots \rangle$. The main problem is the occurrence of $\mathcal{H}$ in the thermal weighting factor in

$$\langle A \rangle = \mathrm{Tr}\left(\mathrm{e}^{-\beta\mathcal{H}} A\right), \tag{2.18}$$

which also has to expanded. So continuing to use the time-ordered Green's function requires two S-Matrix expansions making the diagrammatic theory different and complicated. This problem is solved by a trick, which can also be used to describe arbitrary initial correlations.

2.5.1 Matsubara Green's functions

The key to thermal nonequilibrium perturbation theory are Matsubara Green's functions. First, we now work in the grand canonical ensemble, which simply means, that we replace

$$\begin{aligned} \mathcal{H} \to \mathcal{H} - \mu N + \Omega &= \mathcal{K} + \Omega \\ \mathcal{K} &= \mathcal{H} - \mu N \\ \mathrm{e}^{\beta\Omega} &= \mathrm{Tr}(\mathrm{e}^{-\beta\mathcal{K}}). \end{aligned} \tag{2.19}$$

This is the physical description of a particle ensemble at $T \neq 0$.

The aforementioned trick is the replacement $\tau = it$ in the time ordered Green's function and working in **imaginary time** as introduced by Takeo Matsubara [31]. The reason for this formal trick is the functional similarity between the S-Matrix and the thermal weighting factor. This can be seen by inserting the substitution into the Definition 2 to get

$$\begin{aligned} \mathcal{G}(\tau_1 - \tau_2) &= -\left\langle \mathcal{T}\hat{\psi}(\tau_1)\hat{\psi}^\dagger(\tau_2) \right\rangle \\ &= -\mathrm{Tr}[e^{-\beta(\mathcal{K}-\Omega)}\mathcal{T}e^{\tau_1\mathcal{K}}\hat{\psi}(\tau_1)e^{-(\tau_1-\tau_2)\mathcal{K}}\hat{\psi}^\dagger(\tau_2)e^{-\tau_2\mathcal{K}}]. \end{aligned} \tag{2.20}$$

The quantity $\mathcal{G}$ is called the Matsubara Green's function. Using the time ordering operator and the cyclic permutation property of the trace, this expression can be rewritten as

$$\mathcal{G}(\tau) = -\frac{\mathrm{Tr}[e^{-\beta\mathcal{K}_0}\mathcal{T}U(\beta)\hat{\psi}(\tau)\hat{\psi}^\dagger(0)]}{\mathrm{Tr}[e^{-\beta\mathcal{K}_0}U(\beta)]} \tag{2.21}$$

using the time evolution operator in imaginary time

$$U(\tau) = \mathcal{T}\exp\left(-\int_0^{it} \mathcal{H}_{\mathrm{int}}(t')\,dt'\right). \tag{2.22}$$

where the integration is performed on the interval $[0, i\beta]$. This integration domain is also called the **Matsubara contour** and the time ordering operator now orders imaginary times by their absolute values.

2.5.2 Perturbation theory of Matsubara Green's functions

Matsubara proved the Wick's theorem for Matsubara Green's functions. This Wick's theorem is fundamentally different from the one at $T = 0$. The Wick's theorem at $T = 0$ is an operator identity, whereas the Wick's theorem at $T \neq 0$ includes the thermal averaging included in $\langle \ldots \rangle$.

Given that the Wick's theorem holds, all diagrammatic ideas like the Dyson equation or the cancellation of disconnected diagrams with vacuum polarizations still hold for Matsubara Green's functions. The Matsubara Green's functions are even more benign than time ordered Green's functions since contributions due to disconnected diagrams do not diverge.

The theory of Matsubara Green's functions has some very interesting points, that i have no time to discuss here, but I give a few pointers

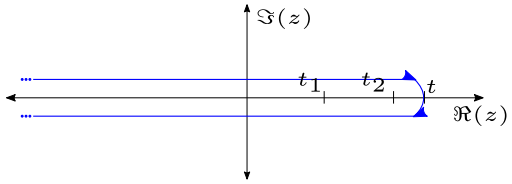

Figure 2.6: Keldysh-Schwinger contour: Iplied to run from $-\infty$ through $t_1, t_2 < t$ and back to $-\infty$ avoiding the reference state at ∞. The contour is entirely on the real axis.

- Depending on whether the system is bosonic or fermionic, the Matsubara Green's function is periodic/antiperiodic in the interval $[0, i\beta]$. This means in frequency space, the Matsubara Green's function is discrete
- Other Green's functions can be obtained from the Matsubara Green's function by analytic continuation. For example the retarded Green's function can be recovered by considering the real frequencies of the analytically continued Matsubara Green's function in the frequency domain.
- The evaluation of diagrams is analogous to the $T = 0$ case, but the integrals over $[-\infty, \infty]$ have to be replaced by integrals over $[0, i\beta]$.
- In frequency space this leads to infinite sums rather than integrals due to the discrete frequencies in the Fourier decomposition, which are often easier to solve by contour integration.

2.6 Nonequilibrium perturbation theory

The essential difference between equilibrium and nonequilibrium problems is reversibility. Since nonequilibrium problems cause irreversible changes to the system, adiabatic switch off does not imply that $|\psi(-\infty)\rangle = |\psi(\infty)\rangle$ and in general any reference to $|\psi(\infty)\rangle$ should be avoided when not at equilibrium. Depending on the specifics of the interactions and switch-ons, this problem may be solved by introducing the concept of **contour ordering** on appropriate contours.

2.6.1 Contour ordered Greens functions

If the system hamiltonian is quadratic in the creation/destruction operators before switch-on, the **Schwinger-Keldysh contour** $\mathcal{C}$, see Figure 2.6, is used as a basis of the perturbative expansion and in the case of initial correlations, the **Kadanoff-Baym contour** $\mathcal{C}^*$, see Figure 2.7, is used to first thermalize the system towards some initial correlations. Discussing initial correlations is not necessary since transport is a steady-state equilibrium problem and the Schwinger-Keldysh switch-on procedure can be used without problem.

The main identity justifying the introduction of contour ordered Green's functions is obtained by rewriting the operator time evolution

$$\hat{A}(t) = U^\dagger(t) A_S U(t) = \mathcal{T}_\mathcal{C}\left[\exp\left(-i \oint_\mathcal{C} \mathcal{H}_{\text{int}}\, d\tau\right) \hat{A}_S\right] \tag{2.23}$$

with the contour S-Matrix

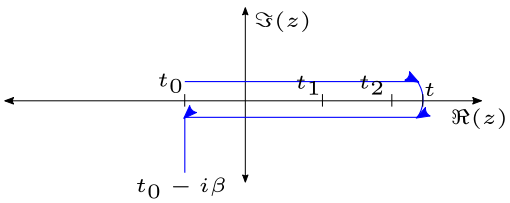

Figure 2.7: Kadanoff-Baym contour: Is a mixture between to Schwinger contour for finite times and the Matsubara imaginary time to handle nonequilibrium interactions and arbitrary initial density matrices.

$$S_{\mathcal{C}}^{\mathcal{H}_{\text{int}}} = \exp\left(-i \oint_{\mathcal{C}} \mathcal{H}_{\text{int}}(\tau)\, d\tau\right). \tag{2.24}$$

The contour ordered Green's function is then defined like the time ordered Green's function

$$G_C(1,2) = -i \left\langle \mathcal{T}_c \hat{\psi}(1)\hat{\psi}^\dagger(2) \right\rangle, \tag{2.25}$$

where times are now assigned to a branch on the Schwinger contour and the contour ordering operator is defined as

$$\mathcal{T}_{\mathcal{C}}(\hat{A}(t_1)\hat{B}(t_2)) = \begin{cases} \hat{A}(t_1)\hat{B}(t_2) & t_2 <_{\mathcal{C}} t_1 \\ \hat{B}(t_1)\hat{A}(t_2) & t_1 <_{\mathcal{C}} t_2, \end{cases} \tag{2.26}$$

where the only difference to time ordering is the smaller relation, which now orders along the contour, see the arrows in the contour plots Figure 2.6 and Figure 2.7. It can be shown, that this expression has a simple perturbation theory. The contour ordered Green's function is related to $G^<$, $G^>$, G_{t} and $G_{\bar{\text{t}}}$ by

$$G_C(t_1,t_2) = \langle T_C \psi(t_1)\psi^\dagger(t_2)\rangle = \begin{cases} G^<(t_1,t_2) & t_1 \in C_1, t_2 \in C_2 \\ G^>(t_1,t_2) & t_1 \in C_2, t_2 \in C_1 \\ G_{\text{t}}(t_1,t_2) & t_1 \in C_1, t_2 \in C_1 \\ G_{\bar{\text{t}}}(t_1,t_2) & t_1 \in C_2, t_2 \in C_2, \end{cases} \tag{2.27}$$

which can easily be seen by considering the cases, since t_1 and t_2 being on different contours implies a fixed order and t_1 and t_2 being on the same contour implies either time or anti-time ordering.

2.6.2 Perturbation theory of contour ordered Green's functions

Just as in the previous cases, the properties of the trace and the contour ordering operator can be used to rewrite the definition of the contour ordered Green's function

$$G_C(1,2) = -i \left\langle \mathcal{T}_C S_C^{\mathcal{H}_{\text{int}}} \hat{\psi}_0(1)\hat{\psi}_0^\dagger(2) \right\rangle_{t_0}, \tag{2.28}$$

where the expectation value $\langle \ldots \rangle_{t_0}$ is taken with respect to the density matrix and states at time t_0, which are assumed to be noninteracting.

Wick's theorem holds for contour ordered Green's functions too and the only difference to the $T = 0$ case is the substitution of all integrals over the interval $[-\infty, \infty]$ with integrals over

the Schwinger-Keldysh contour. The main point is, that the Schwinger Keldysh contour never references the point at $t = \infty$ and simply returns to $-\infty$ instead, which is a well defined reference state.

2.6.3 Analytic continuation formulas

Actually doing calculations with contour integrals is cumbersome and the expressions in Equation 2.27 can be used to simplify quantities of the form

$$C(t_1, t_2) = \oint_c A(t_1, \tau) B(\tau, t_2)\, d\tau, \tag{2.29}$$

which appear frequently in the perturbation expansion and other important expressions like the Dyson equation. The most important product expressions concern the greater and retarded part of a product

$$C^<(t_1, t_2) = \int_{-\infty}^{\infty} A_{\mathrm{ret}}(t_1, \tau) B^<(\tau, t_2) + A^<(t_1, \tau) B_{\mathrm{adv}}(\tau, t_2)\, d\tau \tag{2.30}$$

and

$$C_{\mathrm{ret}} = \int_{-\infty}^{\infty} A_{\mathrm{ret}}(t_1, \tau) B_{\mathrm{ret}}(\tau, t_2)\, d\tau. \tag{2.31}$$

The lesser part of a quantity $C^<$ simply assumes, that $t_1 \in C_1, t_2 \in C_2$ and the retarded part is defined by writing it as linear combination of the other four Green's functions defined in Definition 2

$$G_{\mathrm{ret}}(1, 2) = \theta(t_1 - t_2)[G^>(1, 2) - G^<(1, 2)] \tag{2.32}$$

The first of the two equations requires deformation of the contour to be derived, which is a valid operation as long as both t_1 and t_2 always lie on the deformation.

2.6.4 Quantum kinetic formulas: Keldysh equation

From now on, the integrals over interior variables are omitted and indicated by the order of multiplication. This is mainly done since integration will later be replaced by matrix multiplication, for which the expression take the exact forms provided below.

The analytic continuation formula is required to deduce the Keldysh equation. Using Equation 2.30 in the Dyson equation for contour ordered Green's functions gives

$$\begin{aligned} G^< &= (G_{0,C} + G_{0,C}\Sigma_C G_C)^< \\ &= G_0^< + G_{0,\mathrm{ret}}\Sigma_{\mathrm{ret}} G^< + G_{0,\mathrm{ret}}\Sigma^< G_{\mathrm{adv}} + G_0^<\Sigma_{\mathrm{adv}} G_{\mathrm{adv}}, \end{aligned} \tag{2.33}$$

which is the first iteration step and can be rewritten by repeatedly plugging the equation into itself to yield the infinite order iterate

$$G^< = (1 + G_{\mathrm{ret}}\Sigma_{\mathrm{ret}}) G_0^< (1 + G_{\mathrm{adv}}\Sigma_{\mathrm{adv}}) + G_{\mathrm{ret}}\Sigma^< G_{\mathrm{adv}}, \tag{2.34}$$

which is called the Keldysh equation. The first term contains the initial conditions and always vanishes in the case of macroscopic transport theory to yield the simplified Keldysh equation without initial conditions

$$G^< = G_{\text{ret}}\Sigma^< G_{\text{adv}}. \tag{2.35}$$

The Keldysh equation is a quantum kinetic equation in integral form. It connects the kinetics of the system $G^<$ to the static properties of the system contained in G_{adv} and G_{ret}.

2.7 Definition of Observables

Now that the general theory has been set up, I want to extract useful observables from the formalism and the prime candidates are conductivity, local particle current and local particle density. Both of the local quantities are expressions of the lesser Green's function.

The current observable can be found by considering the time derivative of the particle density operator

$$J = -e\left\langle \dot{N} \right\rangle = -\frac{ie}{\hbar}\left\langle [\mathcal{H}, N] \right\rangle \tag{2.36}$$

and on a lattice, the bond current between sites i and j can be written as

$$J_{ij}(t) = t_{ij}G^<_{ji}(t) - t_{ji}G^<_{ij}(t). \tag{2.37}$$

Transport is a steady state equilibrium problem and the current is time independent. Since the quantities calculated in the simulation are Green's functions in the energy domain, the current must be written in terms of these functions

$$J_{ij} := J_{ij}(0) = \int_{-\infty}^{\infty} t_{ij}G^<_{ji}(E) - t_{ji}G^<_{ij}(E)\, dE \tag{2.38}$$

The particle density is found similarly, but the relation to the lesser Green's function is more obvious

$$\rho_i := \rho_i(0) := \left\langle \hat{\psi}_i^\dagger(0)\hat{\psi}_i(0) \right\rangle = \int_{-\infty}^{\infty} G_{ii}(E)\, dE \tag{2.39}$$

For now consider a two-terminal structure with two chemical potentials μ_L for the left lead and μ_R for the right lead and assume, that $\mu_L > \mu_R$, i.e. electrons flow from left to right. Then using the fluctuation-dissipation relation for the self energy in the Keldysh equation

$$\begin{aligned} \Gamma_i(E) &= \eta_i(E)[G_{\text{adv},i}(E) - G_{\text{ret},i}(E)] \\ G^< &= G_{\text{ret}}\Sigma^< G_{\text{adv}} = G_{\text{ret}}[\eta_L\Gamma_L + \eta_R\Gamma_R]G_{\text{adv}} \\ &= \eta_R G_{\text{ret}}(\Gamma_L + \Gamma_R)G_{\text{adv}} - (\eta_R - \eta_L)G_{\text{ret}}\Gamma_L G_{\text{adv}} \end{aligned} \tag{2.40}$$

where the left term can be identified with **persistent currents**, that do not contribute to the charge transport and the right term as the **transport current**.

$$J_{ij} = \int_{-\infty}^{\infty} \eta_R(E) i_{\text{pers}}(E) + (\eta_L(E) - \eta_R(E)) i_{\text{trans}}(E)\, dE \tag{2.41}$$

$$i_{\text{pers}} = t_{ij}[G_{\text{ret}}(\Gamma_L + \Gamma_R)G_{\text{adv}}]_{ji} - t_{ji}[G_{\text{ret}}(\Gamma_L + \Gamma_R)G_{\text{adv}}]_{ij} \tag{2.42}$$

$$i_{\text{trans}} = t_{ij}[G_{\text{ret}}\Gamma_L G_{\text{adv}}]_{ji} - t_{ji}[G_{\text{ret}}\Gamma_L G_{\text{adv}}]_{ij}. \tag{2.43}$$

The quantity of interest when discussing the spectral current is usually the transport current, since it is related to the conductivity measurement, whereas the persistent current does not contribute to conductivity.

It can be shown, that the persistent current vanishes for time reversal symmetry and is related to, for example circular currents due to an external magnetic field [32].

A similar distinction can be made for the particle density such that

$$\rho(E) = \rho_{\mathrm{pers}}(E) + \rho_{\mathrm{trans}}(E) \tag{2.44}$$

the density consists of contributions corresponding to persistent and transport currents (definitions analogous to the currents).

These considerations may be extended to multiple terminals with arbitrary terminal structures. In the zero bias limit, only the distinction between source/injected electron and sink is important and all sources may be thought of as a left lead and all sinks as a right lead yielding the same expressions as for two terminal structures.

An expression for the conductance or transmission from one lead to another can be found from the Fisher-Lee relations for the calculation of transport from scattering matrices and leads to the simple expression

$$\mathcal{T}(E) = \mathrm{Tr}\left(\Gamma_L G_{\mathrm{ret}} \Gamma_R G_{\mathrm{adv}}\right), \tag{2.45}$$

for the transmission at zero temperature and zero bias. The conductance can be obtained by multiplying the transmission by the conductance quantum $\sigma_0 = \frac{2e^2}{\hbar}$. For nonzero temperatures the zero bias limit of the transmission reads

$$\mathcal{T} = \int_{-\infty}^{\infty} \frac{\partial \eta(E)}{\partial E} \mathcal{T}(E)\, dE. \tag{2.46}$$

Chapter 3

Implementation of transport calculation

3.1 Outline of calculation

The main problems of solving the transport equation are the following

- Inverting a very large $\mathcal{H}$ ($\sim 10^6 \times 10^6$).
- Obtaining Green's function of semi-infinite system (leads).

To illustrate this, I will describe the main steps of doing a transport calculation, assuming zero bias and no self-consistent terms in the self-energy

- Obtain G_{lead} and corresponding self-energy.
- Invert $E + i0^+ - \mathcal{H}(E) - \Sigma_{\text{ret}}(E)$ with a smart strategy.
- Use fluctuation-dissipation relation and Keldysh equation to get $\Sigma^<$.
- Use Keldysh equation to obtain $G^<$.
- Obtain observables from $G^<$.

Let me discuss the matrix formalism used in a finite difference calculation in more detail.

3.2 Inversion of Hamiltonian

Let me first show, why one can write

$$G_{\text{ret}} = (E + i0^+ - \mathcal{H}(E) - \Sigma_{\text{ret}}(E))^{-1}. \tag{3.1}$$

For this the expression for the single particle Green's function matrix is rewritten with matrices, omitting the subscript for the retarded Green's function

$$[(E + i\eta)\mathbb{1} - \boldsymbol{H}]\boldsymbol{G} = \mathbb{1}. \tag{3.2}$$

For the following discussion assume a system with only two leads, but the extension to arbitrary terminal structures is trivial. The second assumption is no interaction between left and right lead. Using the Hamiltonian in the block form

$$\boldsymbol{H} = \begin{pmatrix} \boldsymbol{H}_{\mathrm{L}} & \boldsymbol{V}_{\mathrm{LC}} & 0 \\ \boldsymbol{V}_{\mathrm{LC}}^{\dagger} & \boldsymbol{H}_{\mathrm{C}} & \boldsymbol{V}_{\mathrm{RC}}^{\dagger} \\ 0 & \boldsymbol{V}_{\mathrm{RC}} & \boldsymbol{H}_{\mathrm{R}} \end{pmatrix}, \qquad \boldsymbol{G} = \begin{pmatrix} \boldsymbol{G}_{\mathrm{L}} & \boldsymbol{G}_{\mathrm{LC}} & \boldsymbol{G}_{\mathrm{LR}} \\ \boldsymbol{G}_{\mathrm{CL}} & \boldsymbol{G}_{\mathrm{C}} & \boldsymbol{G}_{\mathrm{CR}} \\ \boldsymbol{G}_{\mathrm{RL}} & \boldsymbol{G}_{\mathrm{RC}} & \boldsymbol{G}_{\mathrm{R}} \end{pmatrix} \tag{3.3}$$

where L denotes the left lead, C the central region and R the right lead. The choice of this block structure is somewhat arbitrary and essentially depends on the choice of lattice enumeration in the implementation. The dimension of the matrices involving the central region is finite, but the matrix dimension of the lead Hamiltonians is infinite, since they are usually modeled by a semi-infinite chain. It is thus necessary to reduce the problem to a finite dimensional one.

These conditions lead to a block matrix equation, using $\boldsymbol{E} = (E + i\eta)\mathbb{1}$

$$\begin{pmatrix} \boldsymbol{E} - \boldsymbol{H}_{\mathrm{L}} & -\boldsymbol{V}_{\mathrm{LC}} & 0 \\ -\boldsymbol{V}_{\mathrm{LC}}^{\dagger} & \boldsymbol{E} - \boldsymbol{H}_{\mathrm{C}} & -\boldsymbol{V}_{\mathrm{RC}}^{\dagger} \\ 0 & -\boldsymbol{V}_{\mathrm{RC}} & \boldsymbol{E} - \boldsymbol{H}_{\mathrm{R}} \end{pmatrix} \begin{pmatrix} \boldsymbol{G}_{\mathrm{L}} & \boldsymbol{G}_{\mathrm{LC}} & \boldsymbol{G}_{\mathrm{LR}} \\ \boldsymbol{G}_{\mathrm{CL}} & \boldsymbol{G}_{\mathrm{C}} & \boldsymbol{G}_{\mathrm{CR}} \\ \boldsymbol{G}_{\mathrm{RL}} & \boldsymbol{G}_{\mathrm{RC}} & \boldsymbol{G}_{\mathrm{R}} \end{pmatrix} = \mathbb{1} \tag{3.4}$$

thus leading to the matrix equation for the center block

$$-\boldsymbol{V}_{\mathrm{LC}}^{\dagger}\boldsymbol{G}_{\mathrm{LC}} + (\boldsymbol{E} - \boldsymbol{H}_{\mathrm{C}})\boldsymbol{G}_{\mathrm{C}} - \boldsymbol{V}_{\mathrm{RC}}^{\dagger}\boldsymbol{G}_{\mathrm{RC}} = \mathbb{1} \tag{3.5}$$

and to get the required $\boldsymbol{G}_{\mathrm{CL}}$ and $\boldsymbol{G}_{\mathrm{CR}}$, two other blocks give

$$\begin{aligned} (\boldsymbol{E} - \boldsymbol{H}_{\mathrm{L}})\boldsymbol{G}_{\mathrm{LC}} - \boldsymbol{V}_{\mathrm{LC}}\boldsymbol{G}_{\mathrm{C}} &= 0 \\ (\boldsymbol{E} - \boldsymbol{H}_{\mathrm{R}})\boldsymbol{G}_{\mathrm{RC}} - \boldsymbol{V}_{\mathrm{RC}}\boldsymbol{G}_{\mathrm{C}} &= 0 \end{aligned} \tag{3.6}$$

leading to the final expression

$$\begin{aligned} \mathbb{1} &= (\boldsymbol{E} - \boldsymbol{H} - \boldsymbol{\Sigma})\boldsymbol{G} \\ \boldsymbol{\Sigma} &= \boldsymbol{V}_{\mathrm{LC}}^{\dagger}(\boldsymbol{E} - \boldsymbol{H}_{\mathrm{L}})^{-1}\boldsymbol{V}_{\mathrm{LC}} + \boldsymbol{V}_{\mathrm{RC}}^{\dagger}(\boldsymbol{E} - \boldsymbol{H}_{\mathrm{R}})^{-1}\boldsymbol{V}_{\mathrm{RC}} \\ \boldsymbol{\Sigma} &= \boldsymbol{V}_{\mathrm{LC}}^{\dagger}\boldsymbol{G}_{\mathrm{L}}\boldsymbol{V}_{\mathrm{LC}} + \boldsymbol{V}_{\mathrm{RC}}^{\dagger}\boldsymbol{G}_{\mathrm{R}}\boldsymbol{V}_{\mathrm{RC}} \end{aligned} \tag{3.7}$$

where the self-energy could be identified by comparison with Equation 3.1 and it naturally splits into a component due to left and right lead $\boldsymbol{\Sigma}_{\mathrm{L}}$ and $\boldsymbol{\Sigma}_{\mathrm{R}}$. This may be generalized to

$$\begin{aligned} \boldsymbol{\Sigma} &= \sum_{n} \boldsymbol{\Sigma}_{n} \\ \boldsymbol{\Sigma}_{n} &= \boldsymbol{V}_{\mathrm{C}n}\boldsymbol{G}_{n}\boldsymbol{V}_{n\mathrm{C}} \end{aligned} \tag{3.8}$$

for an arbitrary number of terminals and matrix structure. These self-energies are finite matrices and it is possible to do finite matrix calculations once Σ has been determined.

3.2.1 General strategy

The systems studied are quite large (order of 1×10^5 sites) and the matrices cannot be fully inverted for this reason. The structure of the problem, i.e. short range single particle interaction and local influence of the contacts, leads to methods in which only a few matrix elements of the

Green's function are evaluated. This makes the discussion of systems on this scale feasible and these methods are generically called recursive Green's function methods. [33]

The method, that is optimal for the discussion of given system strongly depends on the system geometry, since the general idea behind all these methods is to divide the system into smaller subsystems. Then the Green's function of these subsystems is determined and the systems are glued together by some prescription, for example the Dyson equation.

3.2.2 Discrete Dyson equation

In two of the following three methods, the Dyson equation on a lattice is used to connect Green's functions of partial systems to the Green's function of the complete system. For this, we consider a problem of the form

$$\begin{aligned} \boldsymbol{H}_{\mathcal{L}} &= \sum_{i\in \mathrm{L}} \epsilon_i \hat{c}_i^\dagger \hat{c}_i + \sum_{<i,j>\in \mathrm{L}} t_{ij} \hat{c}_i^\dagger \hat{c}_j + \mathrm{h.c.} \\ \boldsymbol{H}_{\mathrm{R}} &= \sum_{i\in \mathrm{R}} \epsilon_i \hat{c}_i^\dagger \hat{c}_i + \sum_{<i,j>\in \mathrm{R}} t_{ij} \hat{c}_i^\dagger \hat{c}_j + \mathrm{h.c.} \\ \boldsymbol{V}_{\mathrm{LR}} &= \sum_{<i,j>, i\in \mathrm{L}, j\in \mathrm{R}} V_{ij} \hat{c}_i^\dagger \hat{c}_j + \mathrm{h.c.} \end{aligned} \tag{3.9}$$

and the self-energy due to the interaction $\boldsymbol{V}_{\mathrm{LR}}$. The resulting self-energy will be $\boldsymbol{\Sigma} = \boldsymbol{V}_{\mathrm{LR}}$. To obtain this expression, consider some terms of the diagrammatic expansion, omitting the index condition and absorbing the hermitian conjugate into the sum

$$\begin{aligned} \left\langle \boldsymbol{V}_{\mathrm{LR}} \hat{c}_k \hat{c}_l^\dagger \right\rangle &= \left\langle \left[\sum_{<i,j>} V_{ij} \hat{c}_i^\dagger \hat{c}_j \right] \hat{c}_k \hat{c}_l^\dagger \right\rangle = \sum_{<i,j>} V_{ij} \left\langle \hat{c}_i^\dagger \hat{c}_j \hat{c}_k \hat{c}_l^\dagger \right\rangle \\ &= \sum_{<i,j>} V_{ij} \left\langle \hat{c}_k \hat{c}_i^\dagger \right\rangle \left\langle \hat{c}_j \hat{c}_l^\dagger \right\rangle = \sum_{<i,j>} V_{ij} \boldsymbol{G}^0_{ki} \boldsymbol{G}^0_{jl} = [\boldsymbol{G}^0 \boldsymbol{V} \boldsymbol{G}^0]_{kl}. \end{aligned} \tag{3.10}$$

To obtain the higher orders one observes, that only terms of the kind $\boldsymbol{G}^0\boldsymbol{V}\boldsymbol{G}^0 + \boldsymbol{G}^0\boldsymbol{V}\boldsymbol{G}^0\boldsymbol{V}\boldsymbol{G}^0 + \ldots$ can appear for connected diagrams and the combinatorics are equivalent to those in the proof of the original Dyson equation prompting the identification $\boldsymbol{\Sigma} = \boldsymbol{V}_{\mathrm{LR}}$.

Thus the Dyson equation for a discrete lattice with hopping interaction between sites is

$$\boldsymbol{G} = \boldsymbol{G}^0 + \boldsymbol{G}^0 \boldsymbol{V}_{\mathrm{LR}} \boldsymbol{G}, \tag{3.11}$$

when the perturbation is $\boldsymbol{V}_{\mathrm{LR}}$ and the physical intuition is gluing partial systems L and R together with $\boldsymbol{V}_{\mathrm{LR}}$.

3.2.3 Knitting

In the paper [34], a recursive method based on the Dyson equation is introduced, where only one site is added to the system at a time. For a square lattice, this would be described by Figure 3.1.

The site, that is added is denoted by $\mathcal{A}$, as in Figure 3.1 and then the different matrix elements of the new Green's function $\boldsymbol{G}^{[\mathcal{A}]}$ due to the Dyson equation are considered. Define an index ordering such that $\alpha < \mathcal{A} < \beta$, then call α to the left of $\mathcal{A}$ and β to the right of $\mathcal{A}$.

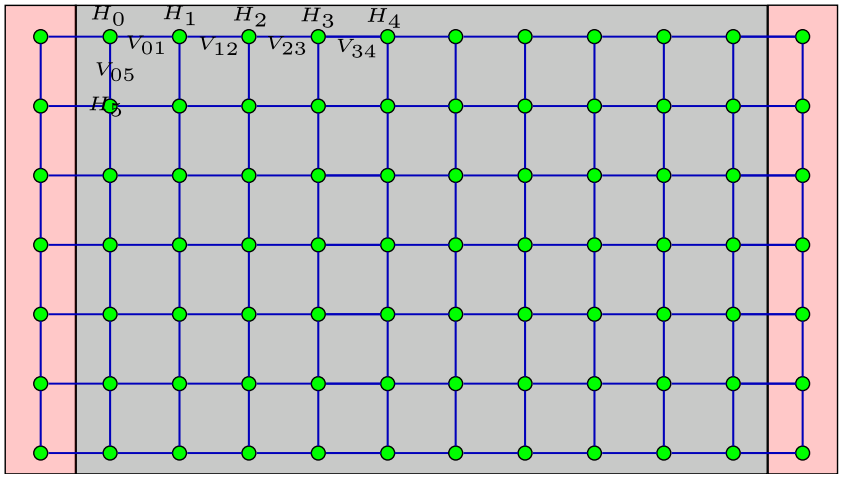

Figure 3.1: Schematic of cutting the system into single sites for a square lattice. The interaction terms are then the matrices from the newly added point to the rest of the system.

$$
\begin{aligned}
\langle \mathcal{A}|\boldsymbol{G}^{[\mathcal{A}]}|\mathcal{A}\rangle &= \langle \mathcal{A}|\boldsymbol{G}^{[\mathcal{A}-1]} + \boldsymbol{G}^{[\mathcal{A}-1]}\boldsymbol{V}^{[\mathcal{A}]}\boldsymbol{G}^{[\mathcal{A}]}|\mathcal{A}\rangle \\
&= \langle \mathcal{A}|\boldsymbol{G}^{[\mathcal{A}-1]} + \boldsymbol{G}^{[\mathcal{A}-1]}\boldsymbol{V}^{[\mathcal{A}]}\boldsymbol{G}^{[\mathcal{A}-1]}\boldsymbol{V}^{[\mathcal{A}]}\boldsymbol{G}^{[\mathcal{A}]}|\mathcal{A}\rangle \\
&= \left(E - E^{[\mathcal{A}]} - \sum_{ij} \boldsymbol{V}^{[\mathcal{A}]}_{\mathcal{A}i}\boldsymbol{G}^{[\mathcal{A}-1]}_{ij}\boldsymbol{V}^{[\mathcal{A}]}_{j\mathcal{A}}\right)^{-1} \\
\langle \alpha|\boldsymbol{G}^{[\mathcal{A}]}|\mathcal{A}\rangle &= \langle \alpha|\boldsymbol{G}^{[\mathcal{A}-1]} + \boldsymbol{G}^{[\mathcal{A}-1]}\boldsymbol{V}^{[\mathcal{A}]}\boldsymbol{G}^{[\mathcal{A}]}|\mathcal{A}\rangle = \sum_i \boldsymbol{G}^{[\mathcal{A}-1]}_{\alpha i}\boldsymbol{V}^{[\mathcal{A}]}_{i\mathcal{A}}\boldsymbol{G}^{[\mathcal{A}]}_{\mathcal{A}\mathcal{A}} \\
\langle \mathcal{A}|\boldsymbol{G}^{[\mathcal{A}]}|\beta\rangle &= \langle \mathcal{A}|\boldsymbol{G}^{[\mathcal{A}-1]} + \boldsymbol{G}^{[\mathcal{A}]}\boldsymbol{V}^{[\mathcal{A}]}\boldsymbol{G}^{[\mathcal{A}-1]}|\beta\rangle = \sum_i \boldsymbol{G}^{[\mathcal{A}]}_{\mathcal{A}\mathcal{A}}\boldsymbol{V}^{[\mathcal{A}]}_{\mathcal{A}i}\boldsymbol{G}^{[\mathcal{A}-1]}_{i\beta} \\
\langle \alpha|\boldsymbol{G}^{[\mathcal{A}]}|\beta\rangle &= \langle \alpha|\boldsymbol{G}^{[\mathcal{A}-1]} + \boldsymbol{G}^{[\mathcal{A}-1]}\boldsymbol{V}^{[\mathcal{A}]}\boldsymbol{G}^{[\mathcal{A}]}|\beta\rangle = \boldsymbol{G}^{[\mathcal{A}-1]}_{\alpha\beta} + \sum_i \boldsymbol{G}^{[\mathcal{A}-1]}_{\alpha i}V_{i\mathcal{A}}\boldsymbol{G}^{[\mathcal{A}]}_{\mathcal{A}\beta} \\
&= \boldsymbol{G}^{[\mathcal{A}-1]}_{\alpha\beta} + \boldsymbol{G}^{[\mathcal{A}]}_{\alpha\mathcal{A}}\boldsymbol{G}^{[\mathcal{A}]}_{\mathcal{A}\beta}/\boldsymbol{G}^{[\mathcal{A}]}_{\mathcal{A}\mathcal{A}}
\end{aligned}
\tag{3.12}
$$

are the fundamental equations of this method for calculation of the retarded Green's function. The matrix $\boldsymbol{V}^{[\mathcal{A}]}$ only contains the hopping terms including the newly added site $\mathcal{A}$. The discussion in [34] also reduces memory footprint by evaluating some additional formulas similar to Equation 3.12 and using these formulas to omit the storage of particular matrix elements.

Even with optimizations this method is slow compared to the other methods presented in the following two chapters, but can be used for arbitrary geometries.

3.2.4 Cutting into stripes

Cutting the system into stripes as discussed in [33] is fundamentally not different from adding to the system site by site. The explicit equations for the implementation are quite different and are usually written in matrix form. This method is very well suited for the geometry illustrated in

Figure 3.2 for obvious reasons, but the strict geometry requirement is also the limitation for this method.

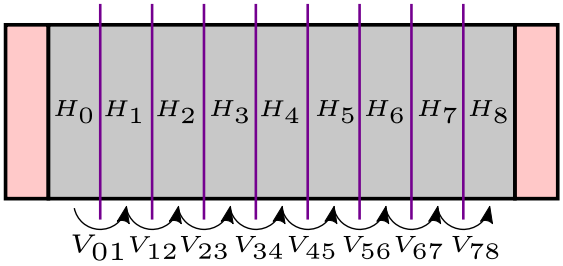

Figure 3.2: Schematic cutting of a bar-shaped system into stripes. In general, the number of stripes is arbitrary and the geometry of the system can deviate from the sketch. As always, the leads are in red and the central region in grey.

We again consider matrix elements, but now the $|n\rangle$ refer to the slice states, in the sense $|n\rangle = \sum_i |n_i\rangle$ where n denotes the nth stripe as in Figure 3.2.

The recursion is split into two parts, a sweep from the left to the right electrode and a sweep from the right to the left electrode. Then $\boldsymbol{G}^{\mathrm{L}}_n$ is the Green's function of the n-th slice due to the left-to-right sweep and $\boldsymbol{G}^{\mathrm{R}}_n$ the same for the right-to-left sweep. The essential difference is, that $\boldsymbol{G}^{\mathrm{L}}_n$ is the Green's function of the n-th slice including all interactions with the system to the left of slice n and $\boldsymbol{G}^{\mathrm{R}}_n$ is the Green's function of the n-th slice including all interactions with the system to the right of slice n. To obtain the full Green's function including interactions with the rest of the system, the information of $\boldsymbol{G}^{\mathrm{L}}_n$ and $\boldsymbol{G}^{\mathrm{R}}_n$ has to be combined, hence the need for two sweeps. The same discussion goes for matrices of the form $\boldsymbol{G}^{\mathrm{L}}_{0,n}$ and $\boldsymbol{G}^{\mathrm{R}}_{n,N}$ for N slices in total.

The left and right sweeps can be obtained with similar considerations as for the knitting equations, yielding the expressions

$$\boldsymbol{G}^{\mathrm{L}}_{n,n} = \left(\boldsymbol{E} - \boldsymbol{H}_n - \boldsymbol{V}_{n,n-1}\boldsymbol{G}^{\mathrm{L}}_{n-1,n-1}\boldsymbol{V}_{n-1,n}\right)^{-1} \tag{3.13}$$

$$\boldsymbol{G}^{\mathrm{L}}_{0,n} = \boldsymbol{G}^{\mathrm{L}}_{0,n-1}\boldsymbol{V}_{n-1,n}\boldsymbol{G}^{\mathrm{L}}_{n,n} \tag{3.14}$$

$$\boldsymbol{G}^{\mathrm{R}}_{n,n} = \left(\boldsymbol{E} - \boldsymbol{H}_n - \boldsymbol{V}_{n,n+1}\boldsymbol{G}^{\mathrm{R}}_{n+1,n+1}\boldsymbol{V}_{n+1,n}\right)^{-1} \tag{3.15}$$

$$\boldsymbol{G}^{\mathrm{R}}_{N,n} = \boldsymbol{G}^{\mathrm{R}}_{N,n+1}\boldsymbol{V}_{n+1,n}\boldsymbol{G}^{\mathrm{R}}_{n,n}. \tag{3.16}$$

This information is somewhat redundant, since the right sweep equations directly follow from the left sweep equations. The combination into the diagonal elements of Green's function for the whole system is given by

$$\boldsymbol{G}_{n,n} = (\boldsymbol{E} - \boldsymbol{H}_n - \boldsymbol{V}_{n,n-1}\boldsymbol{G}^{\mathrm{L}}_{n-1,n-1}\boldsymbol{V}_{n-1,n} - \boldsymbol{V}_{n,n+1}\boldsymbol{G}^{\mathrm{R}}_{n+1,n+1}\boldsymbol{V}_{n+1,n})^{-1} \tag{3.17}$$

Other matrix elements can be obtained with equations of the type

$$\boldsymbol{G}_{0,n} = \boldsymbol{G}^{\mathrm{L}}_{0,n-1}\boldsymbol{V}_{n-1,n}\boldsymbol{G}_{n,n} \tag{3.18}$$

$$\boldsymbol{G}_{N,n} = \boldsymbol{G}^{\mathrm{R}}_{N,n+1}\boldsymbol{V}_{n+1,n}\boldsymbol{G}_{n,n}. \tag{3.19}$$

One can also define recursive equations for the lesser Green's function $\boldsymbol{G}^{<}$, but in my experience, explicitly performing the Keldysh equation with sparse matrix methods is simpler and faster.

3.2.5 Block-Gaussian inversion

The block-Gaussian inversion is described in [35] and is fundamentally different from the previous methods, but essentially still works by splitting the system into appropriate subsystems. This procedure produces a Hamiltonian with a block structure and with a block-Gaussian inversion only select matrix elements of the inverse may be calculated. This is especially useful for sparse Hamiltonian matrices. Since the efficiency of block-based methods strongly depends on the size of the largest occurring block, this quantity must be minimized by the appropriate choice of subsystems. I will describe an algorithm for the determination of such a block-Hamiltonian. The exact choice of algorithm depends on the matrix elements and as such the observables one wants to calculate. For this call α, β lead indices and $\mathcal{A}$ an index in the central region.

- Calculation of conductivity tensor $\Rightarrow G_{\alpha\beta}$ must be determined
  - Define the first block $\mathcal{B}_0$, the sites contained in the left lead and the last block $\mathcal{B}_N$, the sites contained in the right lead.
  - Starting from $n = 1$, define $\mathcal{B}_{n+1}$ by collecting all sites with hopping elements connected to $\mathcal{B}_n$, but not contained in $\mathcal{B}_n$ or $\mathcal{B}_N$.
  - If any site connected to $\mathcal{B}_n$ is contained in $\mathcal{B}_N$, call $\mathcal{B}_n = \mathcal{S} \setminus \left[\bigcup_{i=0}^{n-1} \mathcal{B}_i \cup \mathcal{B}_N\right]$, where $\mathcal{S}$ is the entire system. After this $\mathcal{S} = \bigcup_{i=0}^{N} \mathcal{B}_i$.
- Calculation of local current $\Rightarrow G_{\alpha\mathcal{A}}$ and $G_{\mathcal{A}\beta}$ must be determined
  - Instead of defining a first and last Block, just define the first block $\mathcal{B}_0$ as the collection of all lead sites.
  - Starting from $n = 1$, define $\mathcal{B}_{n+1}$ by collecting all sites with hopping elements connected to $\mathcal{B}_n$, but not contained in $\mathcal{B}_n$ until $\mathcal{B}_{n+1} = \emptyset$

These two procedures produce collections of sites $\{\mathcal{B}_0, \mathcal{B}_1, \ldots, \mathcal{B}_N\}$ where $\mathcal{B}_n$ is only connected to $\mathcal{B}_{n-1}$ and $\mathcal{B}_{n+1}$. By choosing an indexing scheme such that for $i \in \mathcal{B}_n$ and $j \in \mathcal{B}_m$ the implication $n < m \Rightarrow i < j$ holds, the resulting Hamiltonian will automatically have the desired tridiagonal block structure. Of course these are only two examples of indexing schemes, which are convenient to work with.

The Hamilton matrices, that are produced by these procedures have two characteristic block structures which can both be solved with the methods discussed in [35]. The contents of the block Gaussian inversion can essentially be condensed into a few simple matrix block equations. First define the matrix

$$\boldsymbol{a} = \boldsymbol{E} - \boldsymbol{H} - \boldsymbol{\Sigma} \tag{3.20}$$

with previously defined blocks $\boldsymbol{a}_{ij}$. The elimination is then split into a left-looking and a right-looking elimination with auxiliary matrices $\boldsymbol{c}$ and $\boldsymbol{d}$

$$\boldsymbol{d}^{\mathrm{L}}_{ii} = \boldsymbol{a}_{ii} + \boldsymbol{c}^{\mathrm{L}}_{i-1}\boldsymbol{a}_{i-1,i} \qquad \text{where } i = 2, 3, \ldots, n \text{ and } \boldsymbol{d}^{\mathrm{L}}_{11} = \boldsymbol{a}^{\mathrm{L}}_{11} \tag{3.21}$$

$$\boldsymbol{c}^{\mathrm{L}}_{i} = -\boldsymbol{a}_{i+1,i}(\boldsymbol{d}^{\mathrm{L}}_{ii})^{-1} \qquad \text{where } i = 1, 2, \ldots, n-1 \tag{3.22}$$

$$\boldsymbol{d}^{\mathrm{R}}_{ii} = \boldsymbol{a}_{ii} + \boldsymbol{c}^{\mathrm{R}}_{i+1}\boldsymbol{a}_{i+1,i} \qquad \text{where } i = n-1, \ldots, 2, 1 \text{ and } \boldsymbol{d}^{\mathrm{R}}_{nn} = \boldsymbol{a}^{\mathrm{R}}_{nn} \tag{3.23}$$

$$\boldsymbol{c}^{\mathrm{R}}_{i} = -\boldsymbol{a}_{i-1,i}(\boldsymbol{d}^{\mathrm{R}}_{ii})^{-1} \qquad \text{where } i = n, \ldots, 3, 2 \tag{3.24}$$

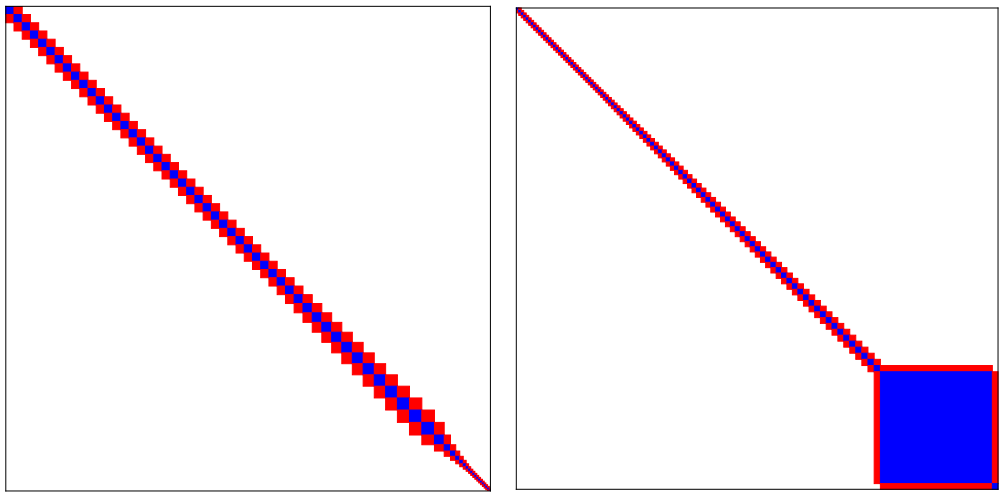

Figure 3.3: In blue are the blocks and in red the interaction between them. Both are for a Hallbar geometry. On the left the electron injection and electron drain lead are combined and required to be the topmost block. On the right, the source lead is required to be the top block and the drain lead is the bottom block. The right method actually produces smaller blocks for a square geometry.

which can be combined to give select blocks of the Green's function

$$\boldsymbol{G}_{ii} = (-\boldsymbol{a}_{ii} + \boldsymbol{d}_{ii}^{\mathrm{L}} + \boldsymbol{d}_{ii}^{\mathrm{R}}) \tag{3.25}$$

$$\boldsymbol{G}_{ij} = \boldsymbol{G}_{ii}\boldsymbol{c}_{i+1}^{\mathrm{R}}\boldsymbol{c}_{i}^{\mathrm{R}}\ldots\boldsymbol{c}_{j}^{\mathrm{R}} \qquad \text{for } i < j \tag{3.26}$$

$$\boldsymbol{G}_{ij} = \boldsymbol{G}_{ii}\boldsymbol{c}_{i-1}^{\mathrm{L}}\boldsymbol{c}_{i-2}^{\mathrm{L}}\ldots\boldsymbol{c}_{j}^{\mathrm{R}} \qquad \text{for } i > j. \tag{3.27}$$

These are reminiscent of the equations for a system cut into stripes. The stripe method can be combined with the blocking algorithm to handle more arbitrary geometries, but the block inversion is essentially equivalent in that case. A proper derivation is given in [35] and not reproduced here.

3.3 Lead self-energies

To calculate the system Green's functions, the lead self-energies must first be determined. Leads are contacts with a certain chemical potential and are usually modeled by semi-infinite chains, that are attached to the central region. The exact structure of this chain should be irrelevant for the calculations, since it merely serves to inject Bloch-waves into the system. That aside, any surface can be modeled by an appropriate semi-infinite chain this way [36]. When an external magnetic field is introduced, the choice of magnetic field in the leads may lead to reflection of ingoing Bloch waves and as such and it is usually best to match the structure of the lead to the structure of the central region to avoid these problems.

The two main methods for determining the self-energy of a semi-infinite chain are by iteration or by direct solution of the Schrödinger equation for Bloch waves.

3.3.1 Slice Iteration

The iterative method is essentially quite simple, since it is formally just a left to right sweep of repeating stripes.

The Dyson equation gives the Green's functions of the chain

$$\begin{aligned}
\boldsymbol{G}_{0,0} &= (\boldsymbol{E}-\boldsymbol{H})^{-1} + (\boldsymbol{E}-\boldsymbol{H})^{-1}\boldsymbol{V}\boldsymbol{G}_{1,0} \\
\boldsymbol{G}_{1,0} &= (\boldsymbol{E}-\boldsymbol{H})^{-1}\boldsymbol{V}^{\dagger}\boldsymbol{G}_{0,0} + (\boldsymbol{E}-\boldsymbol{H})^{-1}\boldsymbol{V}\boldsymbol{G}_{2,0} \\
&\vdots \\
\boldsymbol{G}_{n,0} &= (\boldsymbol{E}-\boldsymbol{H})^{-1}\boldsymbol{V}^{\dagger}\boldsymbol{G}_{n-1,0} + (\boldsymbol{E}-\boldsymbol{H})^{-1}\boldsymbol{V}\boldsymbol{G}_{n+1,0}.
\end{aligned} \tag{3.28}$$

However, a large number of stripes are required for the Green's function to actually converge. The exact number depends on the specific system and the required accuracy of the result, but generically one needs more than 10^4 stripes for a satisfactory result.

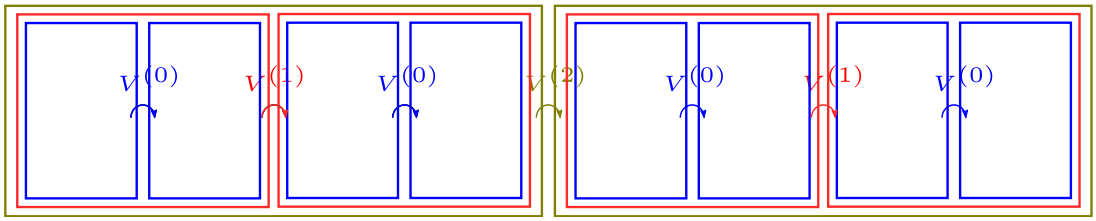

Figure 3.4: Schematic rendering of the iteration procedure. After evaluating Green's functions of two segments, they are combined into one and the new effective Hamiltonian and interaction matrices are considered.

For this reason, a trick is used to compute a system with 2^n stripes in n steps. The essential idea is illustrated in Figure 3.4 and a proof is given in [37]. Since $V_{n+1} = V_n$ and $H_{n+1} = H_n$, an effective surface Hamiltonian $\boldsymbol{H}_s^{(i)}$ for the sites on the right of the combined stripes can be defined. In the same manner, an effective interaction to the left $\boldsymbol{V}^{\dagger,(i)}$ and right $\boldsymbol{V}^{(i)}$ and an effective bulk Hamiltonian with two chains to the left and right $\boldsymbol{H}^{(i)}$ can be defined.

The equations for these quantities can be written as

$$\boldsymbol{G}^{(i)} = (\boldsymbol{E}-\boldsymbol{H}^{(i)})^{-1} \tag{3.29}$$

$$\boldsymbol{V}^{(i)} = \boldsymbol{V}^{(i-1)}\boldsymbol{G}^{(i-1)}\boldsymbol{V}^{(i-1)} \qquad \boldsymbol{V}^{(0)} = \boldsymbol{V} \tag{3.30}$$

$$\boldsymbol{V}^{\dagger,(i)} = \boldsymbol{V}^{\dagger,(i-1)}\boldsymbol{G}^{(i-1)}\boldsymbol{V}^{\dagger,(i-1)} \qquad \boldsymbol{V}^{\dagger,(0)} = \boldsymbol{V}^{\dagger} \tag{3.31}$$

$$\boldsymbol{H}^{(i)} = \boldsymbol{H}^{(i-1)} + \boldsymbol{V}^{(i-1)}\boldsymbol{G}^{(i-1)}\boldsymbol{V}^{\dagger,(i-1)} + \boldsymbol{V}^{\dagger,(i-1)}\boldsymbol{G}^{(i-1)}\boldsymbol{V}^{(i-1)} \qquad \boldsymbol{H}^{(i)} = \boldsymbol{H}^{(i)} \tag{3.32}$$

$$\boldsymbol{H}_s^{(i)} = \boldsymbol{H}^{(i-1)} + \boldsymbol{V}^{(i-1)}\boldsymbol{G}^{(i-1)}\boldsymbol{V}^{\dagger,(i-1)} \qquad \boldsymbol{H}_s^{(i)} = \boldsymbol{H}^{(i)} \tag{3.33}$$

The Green's function $\boldsymbol{G}^{(i)}$ is not the Green's function for the right surface of the chain, but the bulk of the chain. The surface Green's function needed to calculate the self-energy of the lead in question is

$$\boldsymbol{G}_s = \lim_{i\to\infty}\left(\boldsymbol{E}-\boldsymbol{H}_s^{(i)}\right)^{-1}, \tag{3.34}$$

where, in practice, $i \sim 15$ suffices, since it corresponds to $2^{15} = 32768$ stripes to the left of the lead-device contact.

3.3.2 Solution of the Schrödinger equation

Instead of using the Dyson equation to calculate the self-energy of a semi-infinite chain, the Schrödinger equation for such a chain can be directly solved. The discrete Schrödinger equation for a wavefunction $\Psi = (\mathbf{c}_0, \ldots, \mathbf{c}_n, \ldots)^T$ reads

$$-\boldsymbol{V}\mathbf{c}_{i-1} + (\boldsymbol{E} - \boldsymbol{H})\mathbf{c}_i - \boldsymbol{V}^\dagger \mathbf{c}_{i+1} = 0 \tag{3.35}$$

and using the periodicity to get Bloch waves, i.e. $\mathbf{c}_i = \lambda \mathbf{c}_{i-1}$ one can rewrite it as the quadratic eigenvalue equation

$$\boldsymbol{V}\mathbf{u}_n(\pm) + (\boldsymbol{E} - \boldsymbol{H})\lambda_n(\pm)\mathbf{u}_n(\pm)\boldsymbol{V}^\dagger \lambda_n^2(\pm)\mathbf{u}_n(\pm) = 0 \tag{3.36}$$

where $\pm$ indicates the propagation direction, right going $(+)$ and left going $(-)$. This cubic eigenvalue equation can be rewritten as a generalized eigenvalue equation [38]

$$\left[\begin{pmatrix} \boldsymbol{E} - \boldsymbol{H} & \boldsymbol{V} \\ \mathbb{1} & 0 \end{pmatrix} - \lambda \begin{pmatrix} -\boldsymbol{V}^\dagger & 0 \\ 0 & \mathbb{1} \end{pmatrix}\right] \begin{pmatrix} \mathbf{c}_i \\ \mathbf{c}_{i-1} \end{pmatrix} = 0. \tag{3.37}$$

For further discussion define

$$\boldsymbol{A} = \begin{pmatrix} \boldsymbol{E} - \boldsymbol{H} & \boldsymbol{V} \\ \mathbb{1} & 0 \end{pmatrix}, \qquad \boldsymbol{B} = \begin{pmatrix} -\boldsymbol{V}^\dagger & 0 \\ 0 & \mathbb{1} \end{pmatrix}, \qquad \mathbf{v} = \begin{pmatrix} \mathbf{c}_i \\ \mathbf{c}_{i+1} \end{pmatrix} \tag{3.38}$$

to rewrite Equation 3.37 into

$$\boldsymbol{A}\mathbf{v} = \lambda \boldsymbol{B}\mathbf{v}. \tag{3.39}$$

Some general remarks can be made about equations of this form: In general, $\boldsymbol{V}$ and $\boldsymbol{V}^\dagger$ are singular and $\boldsymbol{E} - \boldsymbol{H}$ has full rank. This implies, that $\boldsymbol{A}$ and $\boldsymbol{B}$ are also singular and the equation

$$\boldsymbol{B}^{-1}\boldsymbol{A}\mathbf{v} = \lambda \mathbf{v} \tag{3.40}$$

can generally not be formed for two-dimensional systems.

The Bloch states are usually classified by two criteria. Left going or right going and propagating or evanescent. The direction of the wave is identified by considering the sign of the velocity

$$v_n(\pm) = \frac{2a}{\hbar} \operatorname{Im}(\lambda_n(\pm)\mathbf{v}_n(\pm)\boldsymbol{V}_n^\dagger \mathbf{v}_n(\pm)) \tag{3.41}$$

The states come in pairs, for every right propagating wave, there is a left propagating one [39]. This is physically obvious, since an infinite chain is left-right inversion symmetric.

Evanescent modes can be identified by the magnitude of the corresponding eigenvalue

- $|\lambda_n(+)| < 1$: right-going evanescent modes
- $|\lambda_n(-)| < 1$: left-going evanescent modes
- $|\lambda_n(\pm)| = 1$: propagating modes

These classifications are obvious since $\mathbf{c}_i = \lambda \mathbf{c}_{i-1}$. Due to this classification, a cutoff δ is usually defined to omit all eigenvalues, that are not in the range

$$\lambda_n(\pm) \in \left[\frac{1}{\delta}, \delta\right] \tag{3.42}$$

since their contribution will be negligible and will only ruin the numerical accuracy due to very large or small values.

There are a few methods for solving such an equation

- Solve $\boldsymbol{A}\mathbf{v} = \lambda \boldsymbol{B}\mathbf{v}$ directly by applying a routine such as ZGGEV from LAPACK.
- Do a shift invert spectral transformation and determine the shift-inverted eigenvalues and eigenvectors with a normal diagonalization algorithm such as ZGEEV from LAPACK [40].
- Do a shift invert spectral transformation and solve the transformed equation with Krylov-space based methods using tricks like partitioning the space of eigenvalues and using different shift-invert parameters in different regions. [40]

Using the solution of this equation, the surface Green's function can be constructed by defining the Bloch matrices

$$\boldsymbol{F}(\pm) = \sum_{\lambda_n(\pm)} \lambda_n(\pm)\mathbf{c}_n(\pm)\widetilde{\mathbf{c}}_n(\pm), \tag{3.43}$$

where $\widetilde{\mathbf{c}}_n$ is the dual basis of $\mathbf{c}_n$. The surface Green's functions can then be expressed as

$$\begin{aligned} \boldsymbol{g}_L(E) &= \boldsymbol{F}_L^{-1}(-)(\boldsymbol{B}_L^\dagger)^{-1} \\ \boldsymbol{g}_R(E) &= \boldsymbol{F}_R(+)\boldsymbol{B}_R^{-1} \end{aligned} \tag{3.44}$$

for the surface of a left and a right lead respectively, where the subscript identifies the matrices for the respective leads [41, 42].

3.4 Calculation of $G^<$

The publications [33] and [34] define recursion methods to calculate matrix elements of $\boldsymbol{G}^<$, but in this implementation, the matrix multiplication

$$\boldsymbol{G}^< = \boldsymbol{G}_{\mathrm{ret}}\boldsymbol{\Sigma}^<\boldsymbol{G}_{\mathrm{adv}} = \boldsymbol{G}_{\mathrm{ret}}\boldsymbol{\Sigma}^<\boldsymbol{G}_{\mathrm{ret}}^\dagger \tag{3.45}$$

is explicitly performed. If all matrix elements of $\boldsymbol{G}^<$ are calculated, this procedure is expensive, since $\boldsymbol{G}^<$ is not a sparse matrix. If the sparse matrix multiplication algorithm is extended to only calculate a few matrix elements of $\boldsymbol{G}^<$, this calculation is sped up significantly. The required matrix elements are the diagonal elements for the particle density and the entries with nonzero hopping for the particle current.

Chapter 4

Topology in two-dimensional materials

4.1 Free electrons in an external magnetic field

Including electromagnetic interactions in a Hamiltonian is achieved by replacing the derivative with a covariant derivative for the electrodynamical gauge field $\boldsymbol{A}$

$$\hat{\mathcal{H}} |\psi\rangle = \left[\frac{1}{2m} \left(\hat{\boldsymbol{p}} - q\hat{\boldsymbol{A}}(\boldsymbol{r}) \right)^2 + \hat{\boldsymbol{V}}(\boldsymbol{r}) \right] |\psi\rangle \,. \tag{4.1}$$

Assuming a magnetic field in z-direction and no external electric field

$$\nabla \times \boldsymbol{A} = B\boldsymbol{e}_z. \tag{4.2}$$

This equation has no unique solution for $\boldsymbol{A}$ and we have to choose a gauge to do physics. One choice is the Landau gauge

$$\boldsymbol{A} = xB\boldsymbol{e}_y \tag{4.3}$$

and another choice of interest is the symmetric gauge

$$\boldsymbol{A} = \frac{B}{2}(\boldsymbol{e}_y - \boldsymbol{e}_x). \tag{4.4}$$

Solving the Schrödinger equation for these two choices leads to discoveries about the motion of electrons in an external magnetic field. The classical solution would be the cyclotron motion of electrons and the application of an electric field at the same time would lead to a Hall drift perpendicular to the external electric field leading to cross-conductance.

Quantum mechanically, the application of an external magnetic field leads to a condensation of the band structure into highly degenerate Landau-levels. Of course, there is no inclusion of electronic structure in the Hamiltonian, but its inclusion would make a simple discussion infeasible. As such, there is some hand-waving involved in the following discussion.

For the Landau gauge, the wave functions of the electrons become

$$\psi_{n,k}(x, y, z) \sim e^{iky} H_n(x + kl_B^2) e^{-(x+kl_B^2)^2/2l_B^2} \tag{4.5}$$

where H_n is a Hermitian polynomial and $l_B = \sqrt{\frac{\hbar}{eB}}$ is the magnetic length. For the symmetric gauge, the wave functions of the lowest levels with $n = 0$ are

$$\psi_{n,m}(x, y, z) = \left(\frac{z}{l_B}\right)^m e^{-|z|^2/4l_B^2}. \tag{4.6}$$

These eigenstates are degenerate with respect to an angular momentum quantum number m. The corresponding energy levels are those of the harmonic oscillator

$$E_n = \hbar\omega_B(n + \frac{1}{2}) \tag{4.7}$$

with the cyclotron frequency $w_B = \frac{qB}{m}$. These energy levels are highly degenerate. Every energy level has a degeneracy of

$$D = \frac{eBA}{\phi_0}, \quad \phi_0 = \frac{2\pi\hbar}{e}, \tag{4.8}$$

where ϕ_0 is the magnetic flux quantum.

The degeneracy can be physically interpreted semiclassically by parcelling the area A of the sample into parcels of area $2\pi l_B^2$, such that

$$D = \frac{A}{2\pi l_B^2}. \tag{4.9}$$

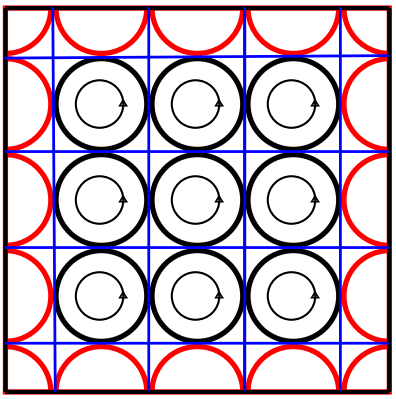

Figure 4.1: Each cyclotron orbit of an electron is enclosed in a parcel of size $2\pi l_B^2$ in blue. The total area of the material is A.

This is illustrated in the comic Figure 4.1. This by no means describes the physics of the situation adequately, since a simple change of gauge can yield nonlocal bulk states for which this picture clearly does not apply.

4.2 The integer quantum Hall effect

From classical computations, one would expect the conductivity

$$\rho_{xy} = \frac{B}{ne}, \tag{4.10}$$

where n is the density of electrons. Measurements however show, that

$$\rho_{xy} = \frac{2\pi\hbar}{e^2}\frac{1}{n} \tag{4.11}$$

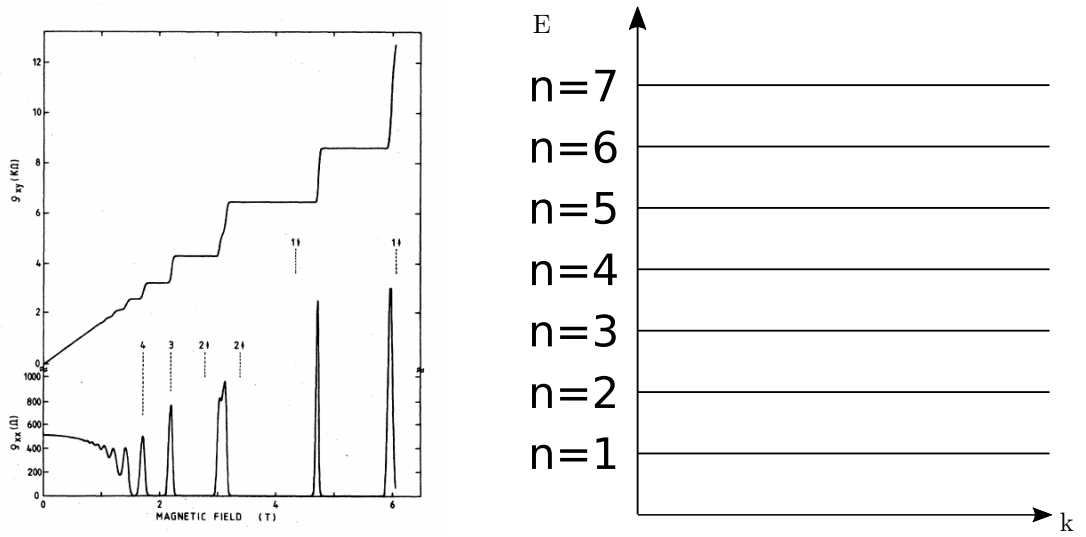

Figure 4.2: Taken from [43]. The original measurement of the quantum Hall effect by K.Klitzing. At the bottom is the longitudinal resistivity and on top is the cross resistivity or Hall resistance (since it is scale independent). There are clearly formed plateaus at specific regions of magnetic field. On the left are the momentum independent Landau levels of a 2D infinite electron gas.

as observed in the initial measurement of the quantum Hall effect in Figure 4.2. This measurement was done in a fairly clean sample at low temperatures. These two expressions coincide, if

$$n = \frac{B}{\phi_0}\nu \tag{4.12}$$

and indeed, at these densities the expressions do coincide.

From this calculation however, one would naively not expect the formation of Landau levels in a clean sample. This is due to the nontrivial contribution of a macroscopic number of bulk states to the transport of electrons. There is no guarantee for the formation of nice plateaus as we see them.

It is well known, that the IQHE is associated with the skipping motions of edge states due to the external magnetic field illustrated semiclassically in Figure 4.3. Bulk states however also contribute to the conductivity in a clean material. The suppression of the contribution due to bulk states is due to the presence of **disorder** in the material. Disorder causes localization of bulk states, but due to the extended nature of edge states due to the skipping motion, they can not be localized. Thus only the edge states of a given Landau level contribute to transport and the plateaus are recovered.

This is of course only true for certain types of defects, that actually only affect bulk states. If the defects have certain structure, such that they might lead to the backscattering of the edge states, the conductivity must be smaller than that of the quantum Hall effect. This is an aspect

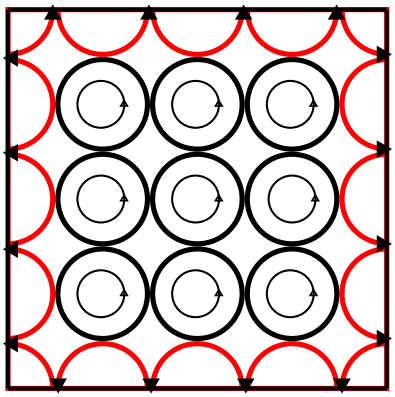

Figure 4.3: A comic of the skipping motions and cyclotron orbits, electrons perform, when an external magnetic field in the z-direction is applied. In this case, the magnetic field points in positive z direction.

of the study of the stability of topological phases with respect to certain types of disorder and this is an active area of research.

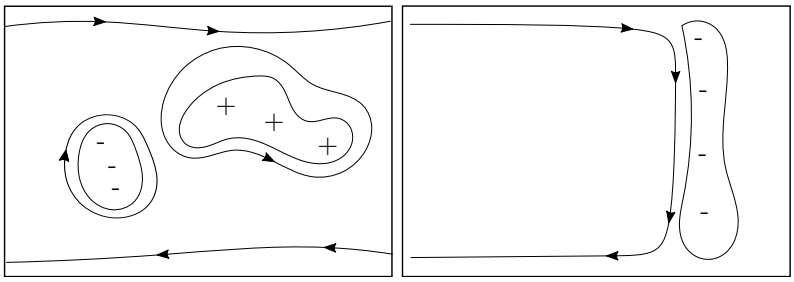

Figure 4.4: On the left and on the right are depictions of a material with some random potential as disorder. This potential will form regions of higher potential and regions of lower potentials around which bulk states localize, turning anti-clockwise around maxima and clockwise around minima. The left image would lead to a quantum Hall effect. In the right case, the material is too small or the disorder too large and causes a hindrance to the IQHE.

The localization of edge states is displayed in Figure 4.4, on the left only bulk states are insulating, but on the right backscattering of edge modes occurs. This would imply, that the right kind of line defect might disturb the IQHE.

4.3 The Berry connection and Berry curvature

The Berry phase, Berry connection, Berry curvature and Chern number of a band structure are uniquely determined by its topology. As such it is no surprise, that they are concepts of differential geometry and algebraic topology. These terms can not only be discussed for band structures, but more general Hamiltonians, that depend on adiabatic parameters.

First, we write the Hamiltonian of the system in question in the following way

$$\mathcal{H}(t) = \mathcal{H}(\mathbf{R}(t), \lambda_1(t), \ldots, \lambda_n(t)) \tag{4.13}$$

where we distinguish fast variables $\mathbf{R}(t)$, which are quantities we usually solve for, like particle positions and slow parameters $\mathcal{P} = \{\lambda_1(t), \ldots, \lambda_n(t)\}$. This differentiation is introduced such that the adiabatic theorem may be applied with respect to the slow change of the Hamiltonian with respect to $\mathcal{P}$. Conversely, these variables may be identified as those for which the adiabatic theorem may be applied.

Let me now define the mathematical terms for the case of a two-dimensional band structure to make things concrete. The manifold of parameters, the crystal momenta p_x, p_y, is the two torus $\mathcal{T}$ due to the their periodicity condition. The most important fact is the nontriviality of the fundamental group of the two-torus, since it is not simply connected. This allows the study of nontrivial fiber bundles defined with the torus as the base space.

Define for every pair of momenta p_x, p_y the vector space of occupied states and denote it as $\mathcal{B}(\mathbf{p})$. Since the number of occupied states is independent of momentum, these vector spaces are isomorphic. For now, assume they are finite dimensional and of dimension n for the number of occupied states. The structure group and connection on this fiber bundle is recognized with some physical insight.

One recognizes, that the dynamical phase evolution of a given starting state is not the correct solution of the adiabatically time evolved Hamiltonian prompting the definition of a geometric phase to correct the solution. The accumulation of this phase around a loop is nonzero and the connection associated with this parallel transport is called the Berry connection

$$\mathcal{A} = \langle \mathcal{P} | \, \mathrm{d}(|\mathcal{P}\rangle) \tag{4.14}$$

with d being the exterior derivative in parameter space and $|\mathcal{P}\rangle$ being a local section of a vector bundle. Since the geometrical phase is an element of $U(n)$ in the general case, we recognize our construct as a $U(n)$ bundle. The Berry curvature is simply the curvature of the Berry connection, which is canonically defined as

$$\mathcal{F} = \mathrm{d}\mathcal{A} + \mathcal{A} \wedge \mathcal{A}, \tag{4.15}$$

where the second term might seem unfamiliar and we will omit it promptly. Since we are interested in noninteracting electrons, i.e. the IQHE, the term $\mathcal{A} \wedge \mathcal{A}$ turns out to vanish, which is a commutativity condition on the derived geometrical phases connected to degeneracies of initial states.

The connection between parallel transport, geometrical phases, and Berry connection and curvature is the following

$$|\mathcal{P}(0)\rangle = \exp\left(- \oint_C \mathcal{A} \right) |\mathcal{P}(1)\rangle \tag{4.16}$$

$$|\mathcal{P}(0)\rangle = \exp\left(- \oint_S \mathcal{F} \right) |\mathcal{P}(1)\rangle \,, \tag{4.17}$$

where C is the mentioned closed loop of parameters and S is a surface bounded by that loop. The exponential factor is recognized as the geometrical phase and it is now obvious, that the connection and curvature characterize the holonomies in the total space. Physically, nontrivial curvature does not imply a nontrivial fiber bundle, but the nontrivial integral across the parameter space does.

This classification of fiber bundles is due to the theory of characteristic classes and more specifically, Chern classes of a complex vector bundle. This theory implies the definition of Chern classes, Chern characters and Chern numbers. Now, one might wonder why there is only ever talk of **the** Chern number of a band structure (at least in two and three dimensions). This is simple due to the fact, that the definitions become very simple in two and three spatial dimensions.

The Chern class of a curvature $\mathcal{F}$ is defined as the expression

$$c(\mathcal{F}) = \det\left(\mathbb{1} + \frac{i\mathcal{F}}{2\pi}\right) \tag{4.18}$$

$$= 1 + c_1(\mathcal{F}) + \ldots + c_n(\mathcal{F}), \tag{4.19}$$

where $c_1(\mathcal{F})$ is a $2j$ form called the j-th Chern class. They clearly vanish for $2j$ larger than the dimension of the base manifold. As a result, there is only one nontrivial Chern class for dimensions two and three

$$c_1(\mathcal{F}) = \det\left(\frac{i\mathcal{F}}{2\pi}\right) = \mathrm{tr}\left(\frac{i\mathcal{F}}{2\pi}\right) \tag{4.20}$$

assuming the curvature has been diagonalized. The Chern numbers are then integrals of particular sums of Chern classes, but in this case, they all reduce to

$$c = \int_S c_1(\mathcal{F}). \tag{4.21}$$

The more commonly used versions of the curvature and connection are recovered by multiplication with a factor of i.

4.4 Restricted Chern numbers

Concepts such as the spin Chern number are not real topological invariants, but approximate topological invariants. The essential idea is to split the parameter manifold. This split could be into a spin up part and a spin down part. In the case of graphene, one often considers the valley spin and splits the manifold accordingly. This is justified by a low scattering probability between the parts of the manifold. One then considers the manifolds as disconnected components and defines Chern Numbers on these disconnected components. They are then named after the variable, which has been used to separate the manifold, such as spin-Chern number or valley-spin-Chern number, etc.

4.5 (Restricted) Chern numbers and edge physics

In this section, Chern numbers may denote a real Chern number or a restricted Chern number depending on the circumstance. Witten describes in his lectures about topological phases in physics [44], how the introduction of a boundary into a system can cause edge localized states to fix a failure to be gauge invariant in a field theoretical model. This statement has not yet been proven in general, but there exist arguments for specific types of Hamiltonians [45] [46] and generalizations [47].

Most commonly referred to as the bulk-boundary correspondence is the relation between topological edge modes and the difference in Chern numbers at a material boundary, i.e.

$$n = \Delta c \tag{4.22}$$

that the number of modes equals the difference in Chern numbers. There also exist statements about the properties of the modes, for example the chirality due to spin-Chern numbers.

Chapter 5

Calculation of topological invariants

Now that some theory on the nature of topological invariants and their relevance for condensed matter systems has been established, there is the question of how one might do a numerical calculation of these invariants given some available electronic structure.

The two methods, I investigated are the methods due to T.Loring [48] and A. Soluyanov and D. Vanderbilt [49] [26].

The first method essentially exactly calculates a closed parameter loop with the use of dimensional reduction techniques and hybrid Wannier charge centers.

The second method involves local indices from K-theory to use the noncommutativity of the position operators due to the nonlocalized states in topological phases. The equivalence of Chern number and Bott index, which is calculated, is shown in [27].

The methods are well explained in the respective publications, so I will only shortly summarize the original discussions.

5.1 Bott index

The mathematical background behind showing the equivalence of Bott index and Chern number, even in certain limits, is very involved. Therefore I will only mention the publications in which the Bott index was extensively discussed and mention some of the fields involved in passing. The following discussion is essentially a summary of [50].

The procedure relies on the definition of periodic position observables

$$\hat{U} = \exp\left(\frac{2\pi i}{L_x}\hat{x}\right), \quad \hat{V} = \exp\left(\frac{2\pi i}{L_y}\hat{y}\right), \tag{5.1}$$

where L_x, L_y are the sizes of a square system, that form a torus for which the invariant is calculated. This is required such that the operator norm of position operators is not extensive. I also define the operator $\hat{\mathcal{P}}$ onto occupied states. Then the projected periodic position observables

$$\hat{U}_1 = \hat{\mathcal{P}}^\dagger \hat{U} \hat{\mathcal{P}}, \quad \hat{V}_1 = \hat{\mathcal{P}}^\dagger \hat{V} \hat{\mathcal{P}} \tag{5.2}$$

obey certain relations. For a reasonable (bounded, gapped) Hamiltonian and large system sizes L_x, L_y

$$\hat{U}_1\hat{U}_1^\dagger \approx \hat{U}_1^\dagger\hat{U}_1 \approx 1 \tag{5.3}$$

$$\hat{U}_1\hat{U}_1^\dagger \approx \hat{U}_1^\dagger\hat{U}_1 \approx 1 \tag{5.4}$$

$$\left[\hat{U}_1, \hat{V}_1\right] \approx 0. \tag{5.5}$$

The last relation would not hold for position operators, since they have extensive operator norm. Matrices with such commutation relations are called **approximately commuting matrices**. A K-theoretic approach to define indices for such approximate relations exists and prompts the definition of the Bott index

$$\mathrm{Bott}(U, V, P) = \mathrm{Re}\left(\frac{1}{2\pi i}\log\left(\hat{U_1}\hat{V_1}\hat{U_1}^\dagger\hat{V_1}^\dagger\right)\right) \tag{5.6}$$

An algorithm due to these definition is as follows

- Define position operators $\hat{X}$ and $\hat{Y}$ for your system
- Find the projector $\hat{P}$ onto the occupied states of the system
- Define quantities

$$U = \hat{P}\exp\left(i\hat{X}\right)\hat{P} + (\mathbb{1} - \hat{P}) \tag{5.7}$$

$$V = \hat{P}\exp\left(i\hat{Y}\right)\hat{P} + (\mathbb{1} - \hat{P}), \tag{5.8}$$

  the exponentials of the projections of the position operators.

- Compute all eigenvalues λ_i of the commutator $VUV^\dagger U^\dagger$
- The Bott index is

$$c = \mathrm{Re}\left(\sum_i \log(\lambda_i)\right) \tag{5.9}$$

Physically, it is clear, that the noncommutativity of the position observables is contained in this number. The exact equality to the Chern number is nontrivial, but a proof exists for the torus in [51].

5.2 Wilson loops for hybrid Wannier functions

The calculation of the Chern number via hybrid Wannier functions has been implemented in the package z2pack, which is available on GitHub. For this thesis, the method has been reimplemented as an exercise in understanding the algorithm and to use the internal format for band structures directly for the calculation. This section is mainly a summary of [52] and [49].

An important point of this calculation is the local $U(n)$ gauge freedom of the n Bloch functions of occupied bands. For nonzero Chern number, the choice of gauge can not be made such that all Bloch bands are smooth. This can quite easily be seen by considering

$$C = \frac{1}{2\pi}\oint_{\partial\Sigma} A \neq 0 \tag{5.10}$$

for the gauge field, the Berry connection A. From complex analysis, this implies, that a pole lies inside the closed loop $\partial\Sigma$. Thus a global choice of gauge can not be smooth.

This property can also discussed from a position space perspective. To fix the gauge, one usually chooses the **maximally localized** Wannier functions, which are achieved by maximizing a functional corresponding to the localization of the associated charge. There is a significant difference between one dimension and two or higher dimensions in the ability to construct such functions.

In one dimension it turns out, that given the projector onto occupied states $\mathcal{P}$, the maximally localized Wannier functions are obtained by $\mathcal{P}\hat{x}\mathcal{P}$, which are smooth in position space.

In two dimensions, the choice is made difficult due to $[\mathcal{P}\hat{x}\mathcal{P}, \mathcal{P}\hat{y}\mathcal{P}] \neq 0$. Thus localization in two spatial directions is nontrivial for a nonzero Chern number of the occupied bands.

A much simpler solution than trying to define two dimensional Wannier functions is obtained by considering **hybrid Wannier functions** by only performing the Fourier transformation in one spatial coordinate

$$|R_x k_y n\rangle = \frac{1}{2\pi} \int_{BZ_{|x}} dk_x e^{ik_x R_x} |\psi_{n\boldsymbol{k}}\rangle \,, \tag{5.11}$$

where $|\psi_{n\boldsymbol{k}}\rangle$ are Bloch functions in some gauge. Now we can reduce the two-dimensional problem into two one-dimensional components if the system is considered one-dimensional with external parameter k_y. Once this is done, hybrid Wannier charge centers can be considered, just as for one dimension since the hybrid Wannier functions are by definition localized in the position variable

$$x_n(k_y) = \langle 0 k_y n | \hat{x} | 0 k_y n \rangle \,. \tag{5.12}$$

In one dimension it can be shown, that the Wannier charge centers are related to the Berry phase using the identity for one dimension

$$x_n = \langle 0n | \, \hat{x} \, | 0n \rangle = \frac{i}{2\pi} \oint A_n(k) dk \tag{5.13}$$

for the n-th band. When k_y is considered an external parameter, this immediately transfers to expressions for hybrid Wannier charge centers. Using this identity, one can express the Chern number as difference of Wannier charge centers. For now, consider only a single band.

$$x_n(\pi) - x_n(-\pi) = \frac{1}{2\pi} \left[\oint A_x(k_y = \pi) dk_x \oint A_x(k_y = -\pi) dk_x \right] \tag{5.14}$$

$$= \frac{1}{2\pi} \int_{BZ} [\nabla \times \boldsymbol{A}]_z = \frac{1}{2\pi} \int_{BZ} \mathcal{F} = C \tag{5.15}$$

where $x_n(\pi) - x_n(-\pi)$ symbolically means the difference in hybrid charge centers after a closed parameter loop in the Brillouin zone. The case for multiple bands is obtained by summing over all occupied bands as usual. Physically, this is quite clear, since the difference in charge centers is the charge pumped due to the winding of the Berry phase. The number of pumped charges is understood to be the Chern number.

Since the Chern number is a winding number in one dimensions, the calculation required is simply the calculation of the winding number of the function $x_n(k_y)$ in one dimension. One such calculation for the Haldane model is shown in Figure 5.1 for a parameter choice, such that the Chern number is one.

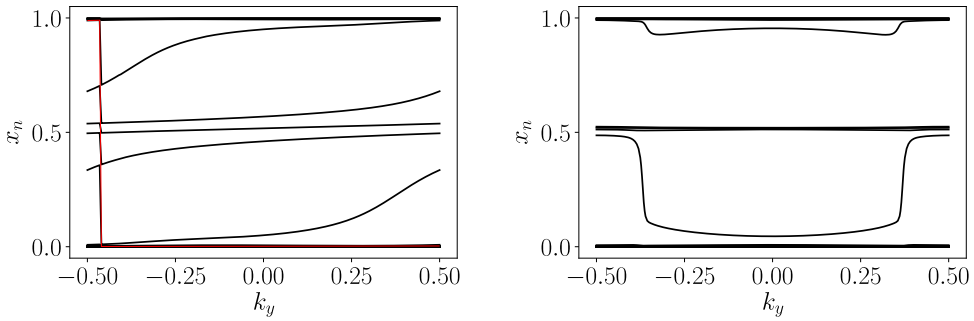

Figure 5.1: On the left is a plot for a Haldane system in a nontrivial topological state with Chern number one. Marked in red is the Wannier charge center belonging to the surface state in the gap. On the right are Wannier charge centers in of the Haldane model in a trivial phase and there is no charge center, that winds around the circle.

Now that the theoretical background of hybrid Wannier charge centers and their relations is explored to some extent, though more material is contained in [52], let us see, how Wannier charge centers are found by matrix calculations. I will essentially sum up the discussion in [49].

- Find the Bloch states $|u_{k,n}\rangle$ for your system.
- Calculate overlap matrices between different momenta

$$M_{n,m}^{k_1,k_2} = \langle u_{k_1,n} | u_{k_2,m} \rangle \tag{5.16}$$

  for a fixed momentum in one direction.

- Take the Hermitian part of the overlap matrix, which is obtained by performing a SVD $M = V\Sigma W^\dagger$ and replacing the overlap matrix with this Hermitian matrix $\mathcal{M} = VW^\dagger$
- The Wannier charge centers can be recovered as the eigenvalues of the Wilson loop

$$\Lambda = \mathcal{M}^{k_0,k_1}\mathcal{M}^{k_1,k_2}\dots\mathcal{M}^{k_{n-1},k_n}. \tag{5.17}$$

  Label them by the fixed momentum value WLOG, the y direction $x_i(k_y)$.

- The Chern number due to these charge centers is

$$C = \sum_n x_n(k_y = 2\pi) - \sum_n x_n(k_y = 0) \tag{5.18}$$

A short explanation on the intuition behind this algorithm is in order. The condition of the hermiticity of overlap matrices is simply the condition that the Bloch states be parallel transported along the Berry connection. The matrix Λ obtained due to these transformations clearly sum up the local gauge transformations to yield a non-Abelian hybrid Berry phase. Due to the relation between Wannier charge centers and the Berry phase in Equation 5.13, the argument of the phase can be found to be a hybrid Wannier charge center.

Chapter 6

Haldane model

6.1 Description of Haldane model

The Haldane model was introduced by Haldane [53] in order to show, that the essential requirement for an IQHE is the breaking of time reversal symmetry instead of simply the presence of an external magnetic field. The Haldane model is a two-dimensional tight-binding model defined on the honeycomb lattice, that extends the graphene nearest neighbour model by next nearest neighbour hopping terms. These hopping terms are constructed in such a way, that they break time reversal symmetry, without any net magnetic flux through the graphene unit cell.

The Haldane model can be written as

$$H_{\text{Haldane}} = H_{\text{Graphene}} + H_{\text{Asymmetry}} + H_{\text{Onsite}} \tag{6.1}$$

where

$$H_{\text{Graphene}} = -t \sum_i \left(a_i^\dagger b_{i+\delta_1} + a_i^\dagger b_{i+\delta_2} + a_i^\dagger b_{i+\delta_3} \right) + \text{h.c.} \tag{6.2}$$

is the usual nearest neighbour Graphene Hamiltonian,

$$H_{\text{Onsite}} = M \sum_i a_i^\dagger a_i - M \sum_i b_i^\dagger b_i \tag{6.3}$$

is an onsite term, that breaks AB symmetry and

$$H_{\text{Asymmetry}} = - t_2 \sum_i e^{i\phi} \left(a_i^\dagger a_{i+\nu_1} + a_{i+\nu_1}^\dagger a_{i-\nu_3} + a_{i-\nu_3}^\dagger a_i \right) \tag{6.4}$$

$$- t_2 \sum_i e^{-i\phi} \left(b_i^\dagger b_{i+\nu_1} + b_{i+\nu_1}^\dagger b_{i-\nu_3} + b_{i-\nu_3}^\dagger b_i \right) \tag{6.5}$$

the important term, which breaks time inversion symmetry without external magnetic field.

From the Figure 6.1, one can clearly see, that any honeycomb contains zero net flux, since the A sublattice contributes the same magnitude, but different sign flux than the B sublattice.

The vectors used in the definition are the nearest neighbour vectors $\delta_1, \delta_2, \delta_3$ and the second nearest neighbour vectors in clockwise direction ν_1, ν_2, ν_3 for Graphene.

Explicitly

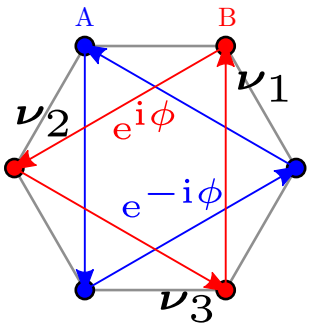

Figure 6.1: A honeycomb sketch of the Haldane model. In black are the nearest neighbour hoppings of strength t_1 and in blue and red are the second nearest neighbour hopping between A and B sublattices with amplitude t_2 respectively. The phase factor in a counter-clockwise loop is indicated in the corresponding color.

$$\delta_1 = a\begin{pmatrix}0\\1\end{pmatrix}, \quad \delta_2 = \frac{a}{2}\begin{pmatrix}-1\\\sqrt{3}\end{pmatrix}, \quad \delta_3 = \frac{a}{2}\begin{pmatrix}-1\\-\sqrt{3}\end{pmatrix} \tag{6.6}$$

and

$$\nu_1 = a\begin{pmatrix}\sqrt{3}\\0\end{pmatrix}, \quad \nu_2 = \frac{a}{2}\begin{pmatrix}-\sqrt{3}\\3\end{pmatrix}, \quad \nu_3 = \frac{a}{2}\begin{pmatrix}-\sqrt{3}\\-3\end{pmatrix}. \tag{6.7}$$

The model can be exactly solved by Fourier transformation and written in the Pauli matrix basis as

$$\mathcal{H}(\boldsymbol{k}) = \left[-2t_2\cos(\phi)\sum_{i=1}^{3}\cos(\boldsymbol{k}\boldsymbol{\nu}_i)\right]\mathbb{1} \tag{6.8}$$

$$+\left[2M - 2t_2\sin(\phi)\sum_{i=1}^{3}\sin(\boldsymbol{k}\boldsymbol{\nu}_i)\right]\boldsymbol{\sigma}_z \tag{6.9}$$

$$+\left[-t\sum_{i=1}^{3}\cos(\boldsymbol{k}\boldsymbol{\delta}_i)\right]\boldsymbol{\sigma}_x + \left[-t\sum_{i=1}^{3}\sin(\boldsymbol{k}\boldsymbol{\delta}_i)\right]\boldsymbol{\sigma}_y \tag{6.10}$$

Using this analytical solution, Haldane argumented the phase diagram in Figure 6.2.

This phase diagram shows the Chern number depending on the parameters of the system. Since the Chern number corresponds to the plateau number, there are clearly regions in which the system exhibits an IQHE.

The phase diagram can be motivated by examining the band structures of the graphene armchair and zigzag nanoribbons for different system parameters and observing surface states in the band gap in the parameter subspace, where an IQHE is exhibited by the system. Except at $M = 0$, the system is either a classical insulator in the white areas and a system in the quantum Hall phase with surface states in the gap in the blue and red areas.

6.2 Results for the Haldane model

In the following section, I will apply the developed methods to an analytically solvable system with nontrivial topology of the band structure. A system intimately related to classical IQHEs is the Haldane model of graphene, since it exhibits only one plateau. As such it is an optimal testing ground.

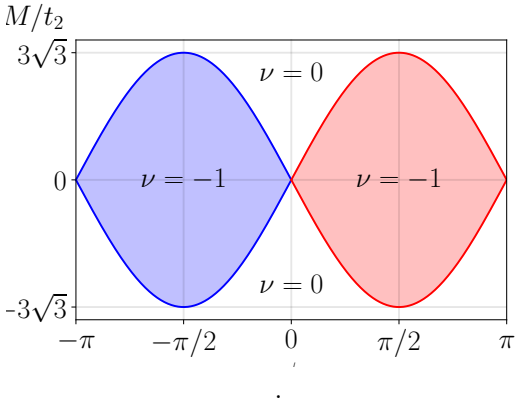

Figure 6.2: Phase diagram of the Haldane model originally calculated in [53]. The parameter ν is the plateau number and the Chern number. The condition for an IQHE is $|M/t_2| < 3\sqrt{3}|\sin(\phi)|$

For the explicit calculations, I always used an extended model including multiple unit cells in both spatial directions. For the calculation of the Bott index this is a requirement and for the calculations with Wannier charge centers it is a preparation for the case of an external magnetic field.

6.2.1 Calculation of topological invariants for the Haldane model

In this section, the model is always the classical Haldane model. We should reproduce the phase diagram in Figure 6.2.

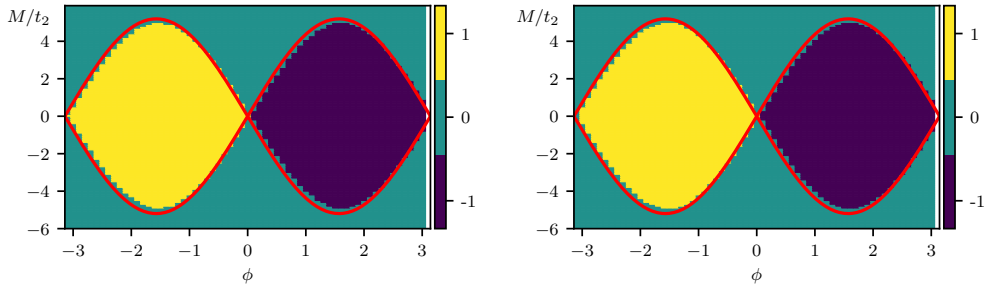

Figure 6.3: In these figures is the phase diagram of the classic Haldane system calculated with the two methods described in the theoretical part. In both cases, an extended system with multiple unit cells was considered, a larger system for the Bott index. On the left is a calculation with Wannier charge centers and on the left is a calculation of the Bott index. Both methods faithfully recreate the phase diagram for systems of sufficient size.

Such a check of the methods is produced in Figure 6.3 for an extended system. Transport calculations for this model are shown in the left plot of Figure 6.4. Wannier charge centers have the advantage, that they already produce accurate results for a system containing a single unit cell. For the calculation of the Bott index, multiple unit cells are required for good convergence of the local index method. The Wannier charge center method however requires hundreds of matrix

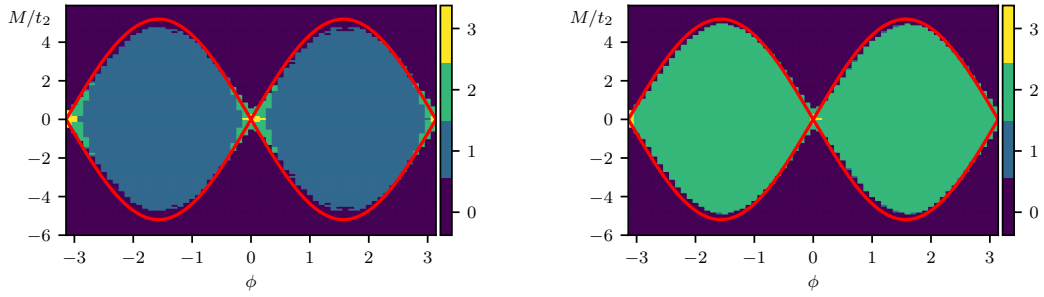

Figure 6.4: Transport trough two different Haldane systems. To the left the system considered is the usual Haldane model without modification and aside from the numerical problems in the semimetal regime, the IQHE is apparent. On the right hand side, the system is a Haldane system with layer switching and shows transport of two modes in the topologically nontrivial regime.

operations of matrices of the system size to converge, whereas the Bott index method requires approximately ten matrix operations.

6.2.2 Calculation of transport for the Haldane model with LSW

The model used in this section is a slightly modified Haldane model. Imagine the system to be extended $L_x/2$ to the left and right of the origin and $L_y/2$ to the top and bottom of the origin and bisect it at the $x = 0$ line. Now invert the flux below this line and keep it constant above the line such that a boundary between a flux ϕ and a flux $-\phi$ is formed.

There is a difference in Chern numbers of two, whenever the classical system is in a nontrivial phase and a difference of zero whenever the classical system is insulating. Therefore on would expect the formation of two topologically protected modes at the boundary.

The transport calculations in Figure 6.4 show exactly the expected behavior.

Chapter 7

Background on graphene

Since this thesis will mainly be dealing with graphene based system, I will now introduce a basic model of single layer graphene and describe some known properties of the system such as the linear dispersion and the anomalous IQHE.

7.1 Graphene tight binding model

An illustration of the primitive vectors and nearest neighbour vectors as defined for the Haldane model is given in Figure 7.1

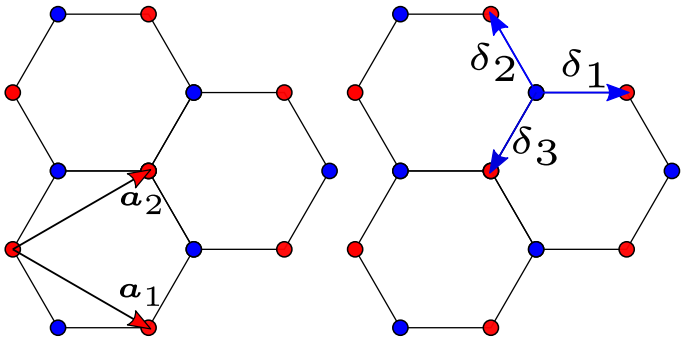

Figure 7.1: The red sites denote the A sublattice and the blue sites the B sublattice of the triangular lattice. On the left is a honeycomb lattice with the unit vectors $\boldsymbol{a}_1$ and $\boldsymbol{a}_2$. The vectors pointing from a site of the A sublattice to all nearest neighbours are $\boldsymbol{\delta}_i$ on the right.

The simplest model for graphene is the nearest neighbour tight binding model already defined in Equation 6.2 for the Haldane model.

For higher order neighbour terms like next nearest neighbour interaction and so on higher order vectors are required. This is tedious and note very informative, but one can always write

$$\mathcal{H} = \sum_i \epsilon_i \hat{a}_i^\dagger \hat{a}_i + t \sum_{\langle i,j \rangle} \hat{a}_i^\dagger \hat{a}_j + t_2 \sum_{\langle\langle i,j \rangle\rangle} \hat{a}_i^\dagger \hat{a}_j + \ldots, \tag{7.1}$$

where the notation of the sublattice in the creation and annihilation operators has been

dropped and $\hat{a}_i^\dagger$ simply denote all lattice sites. As is convention $\langle \ldots \rangle$ denote nearest neighbours, $\langle\langle \ldots \rangle\rangle$ next nearest neighbours etc..

7.2 Electronic structure of graphene

The nearest neighbour model of graphene can be analytically solved by Fourier transformation with the solution

$$\epsilon(\boldsymbol{k}) = \pm t\sqrt{3 + f(\boldsymbol{k})} - t' f(\boldsymbol{k}) \tag{7.2}$$

$$f(\boldsymbol{k}) = 2\cos\left(\sqrt{(}3)k_y a\right) + 4\cos\left(\frac{\sqrt{3}}{2}k_y a\right)\cos\left(\frac{3}{2}k_x a\right). \tag{7.3}$$

Here, t is the nearest neighbour hopping integral and t' the next nearest neighbour term. The resulting band structure is illustrated in Figure 7.2,

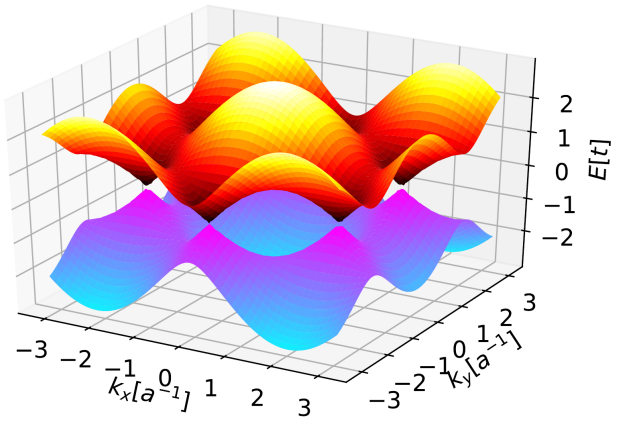

Figure 7.2: Band structure of nearest neighbour graphene bulk using the analytic expression in Equation 7.2. The dispersion is linear at several points, the so called Dirac points, in the Brillouin zone.

The Dirac points of the band structure are located at the following k-points in the Brillouin zone

$$\boldsymbol{K} = \left(\frac{2\pi}{3a}, \frac{2\pi}{3\sqrt{3}a}\right), \quad \boldsymbol{K}' = \left(\frac{2\pi}{3a}, -\frac{2\pi}{3\sqrt{3}a}\right). \tag{7.4}$$

The illustration in Figure 7.2 contains more than the Brillouin zone of the graphene unit cell leading to the inclusion of six Dirac points.

For transport experiments and the IQHE for that matter, nanoribbons are of more interest, since they represent finite systems with edges. The two naturally occurring edge patterns of graphene are armchair and zigzag, corresponding to a horizontal and a vertical cut respectively. They are illustrated in Figure 7.3.

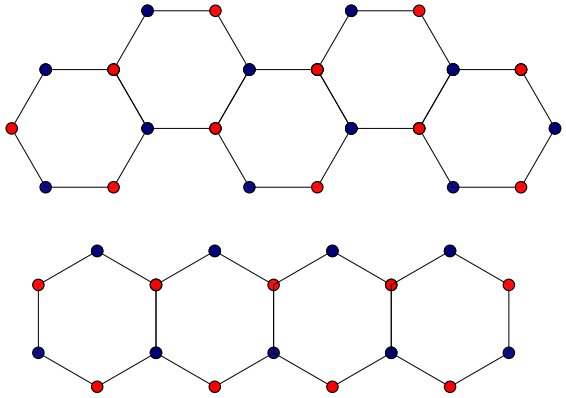

Figure 7.3: In this figure, the two natural edge configurations of graphene are illustrated. The upper one is called an armchair edge and the lower one (rotated by 90 degrees wrt. Figure 7.1) are called zigzag edges.

The 1d band structure of N stacks of nanoribbons would then show the physical properties of a transport setup for a clean sample. These band structures are plotted in Figure 7.4.

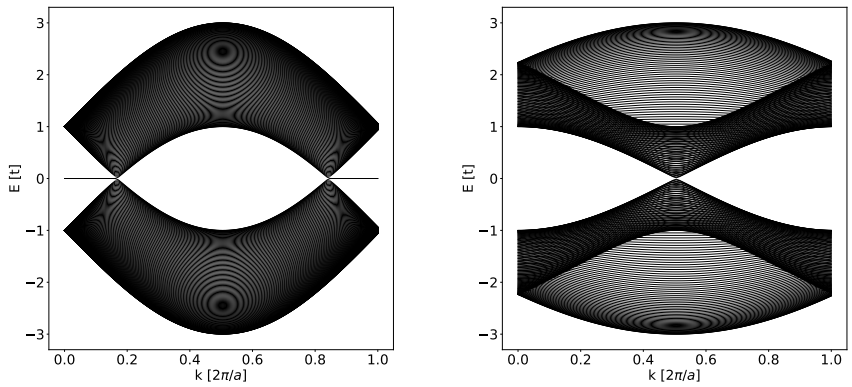

Figure 7.4: On the left is the 1d band structure of a stack of many zigzag nanoribbons and on the right the same for armchair nanoribbons. The linear dispersion and zero energy edge mode at the zigzag edges can clearly be observed.

The band structures in Figure 7.4 are also for the nearest neighbour tight binding model without disorder or magnetic field. Other edge patterns and defects may also appear in graphene [54] and are certainly under investigation [55]. Armchair and zigzag edges however are the most commonly discussed and most naturally occur at the material edge.

The zigzag armchair pattern characteristically exhibits a zero energy mode, which is not present in the armchair edge pattern. It is for this reason, that layer transitions at zigzag borders will later be of more interest.

7.3 The anomalous integer quantum Hall effect of graphene

Since graphene can be modeled with relativistic massless Dirac fermions, the theory of Landau levels must be derived from the Dirac equation instead of the Schrödinger equation and this leads to a conductance formula of the form [56]

$$\sigma_{xy} = -\frac{2e^2}{h}(2n+1), \quad n = 0, 1, 2, \ldots \tag{7.5}$$

while the conductance for a simple semiconductor with the same degeneracies would be

$$\sigma_{xy} = -\frac{4e^2 n}{h}, \quad n = 0, 1, 2, \ldots \tag{7.6}$$

The zeroth Landau level is irrespective of the magnitude of the external magnetic field or energy and thus represents the zero energy modes due to the linear spectrum in absence of a magnetic field.

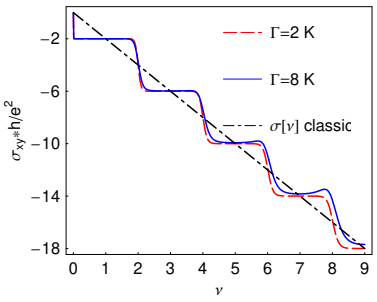

Figure 7.5: Γ is the width of the Lorentzian used to model the landau levels for T=3K. This shows the relation Equation 7.5 for Landau levels with finite width. Taken from [56].

The Landau levels are thus at integers $n = 2, 6, 10, 14, \ldots$. This is shown in the illustration in Figure 7.5. It is called an anomalous IQHE, since the conductivity is not zero on the first plateau and the height of the first plateau is half that of the others.

Chapter 8

Background on bilayer graphene

Bilayer graphene is the generic name of any system consisting of two stacked layers of graphene. Depending on the **twist-angle** θ between the two sheets, the physical properties will vary vastly. The choice of twist angle also corresponds to the choice of stacking for some specific choice of angle, where the material is identified by the sublattice sites stacked on top of each other.

Given the two atom unit cell of graphene, the triangular sublattice containing only the first site is called the A sublattice and the sublattice containing the second basis atom is called the B sublattice.

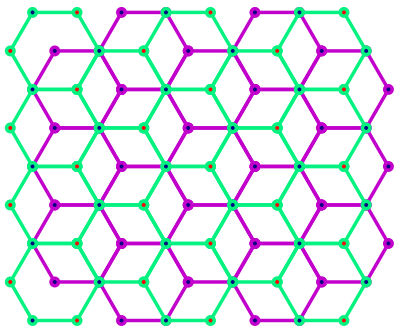

Figure 8.1: Illustration of Bernal stacked BLG. The green sheet is on top and the magenta sheet is on bottom. The blue and red indicate the A and B sublattice respectively for both sheets.

The most common stacking in nature is AB or **Bernal stacking** shown in Figure 8.1, since it is energetically favorable. AB stacking implies, that the site of the A sublattice of the upper layer is on top of the B sublattice of the lower layer. Since this is the energetically most favored geometry, BLG with any other twist angle is called strained.

Another relevant stacking is AA stacking where the twist angle is defined to be zero and the sublattice site A is on top of the sublattice site A and the sublattice site B is on top of the sublattice site B.

Recently magic twist angle BLG with a twist angle of 1.16° or 1.05° has become a popular topic, since it exhibits unconventional superconductivity [57].

8.1 Tight binding model

The Hamiltonian naturally splits into three parts

$$H_{\text{BLG}}^{(\text{AB})} = H_{\text{graphene}}^{(\text{lower})} + H_{\text{graphene}}^{(\text{upper})} + H_{\text{int}}^{\text{AB}}. \tag{8.1}$$

The Hamiltonian $H_{\text{graphene}}^{(\text{lower})}$ and $H_{\text{graphene}}^{(\text{upper})}$ are the ones described in Equation 6.2 for the upper and lower sheet of graphene. Writing the contributions out

$$H_{\text{graphene}}^{(\text{lower})} = -t \sum_i \left(\left(a_i^{(1)}\right)^\dagger b_{i+\delta_1}^{(1)} + \left(a_i^{(1)}\right)^\dagger b_{i+\delta_2} + \left(a_i^{(1)}\right)^\dagger b_{i+\delta_3}^{(1)} \right) + \text{h.c.} \tag{8.2}$$

$$H_{\text{graphene}}^{(\text{upper})} = -t \sum_i \left(\left(a_i^{(2)}\right)^\dagger b_{i+\delta_1}^{(2)} + \left(a_i^{(2)}\right)^\dagger b_{i+\delta_2} + \left(a_i^{(2)}\right)^\dagger b_{i+\delta_3}^{(2)} \right) + \text{h.c.} \tag{8.3}$$

$$H_{\text{int}}^{\text{AB}} = -t_z \sum_i \left(a_i^{(2)}\right)^\dagger b_i^{(1)} + \text{h.c.}. \tag{8.4}$$

For the upper and lower sheet, different creation and annihilation operators are used. In this case, the stacking is explicitly Bernal stacking and the corresponding band structure is shown in Figure 8.2.

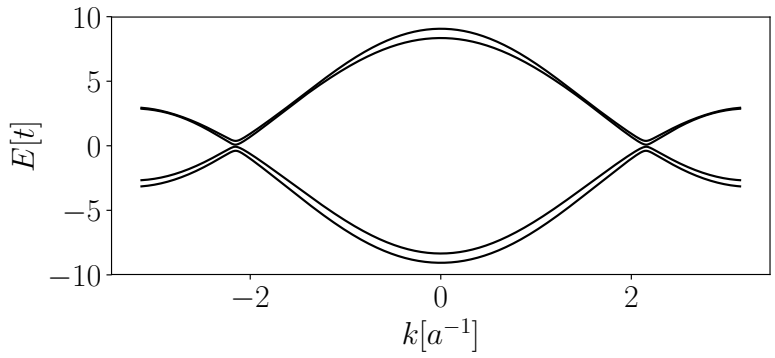

Figure 8.2: band structure of nearest neighbour BLG bulk describing the line $f(k) = k$ in k-space.

The band structure of BLG is remarkably different from that of graphene. The band structure still closes at the K-points defined in Equation 7.4, but the dispersion is no longer linear like for a single sheet of graphene. The dispersion for BLG is quadratic and the electrons can thus no longer be modeled with the Dirac equation close to the Fermi energy.

The model can quite easily be generalized to arbitrary twist angles by choosing an appropriate interaction term H_{int}. Of course, this term becomes quite complicated for any other stacking than AA, AB or BA since the unit cell of the lattice becomes larger. For AA stacking, the interaction term takes the form

$$H_{\text{int}}^{\text{AA}} = -t_z \sum_i \left(\left(a_i^{(2)}\right)^\dagger a_i + \left(b_i^{(2)}\right)^\dagger b_i \right) + \text{h.c.}. \tag{8.5}$$

As with graphene, the transport properties can more easily be seen by inspecting the nanoribbons of the material. The geometries of the nanoribbons, which are usually discussed are just the same as for graphene: Armchair and zigzag, shown in Figure 8.3.

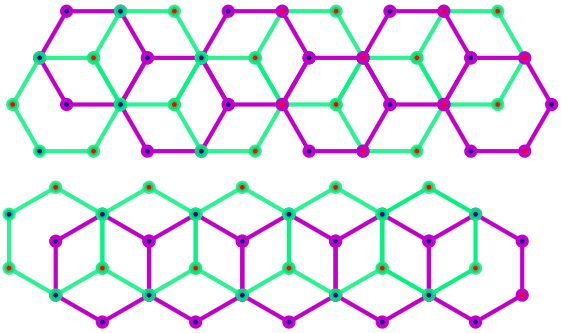

Figure 8.3: Corresponding zigzag and armchair nanoribbons for Bernal stacked BLG. The armchair nanoribbon is on top and the zigzag nanoribbon (rotated) is on the bottom.

The one dimensional band structures of these nanoribbons are respectively shown in Figure 8.4.

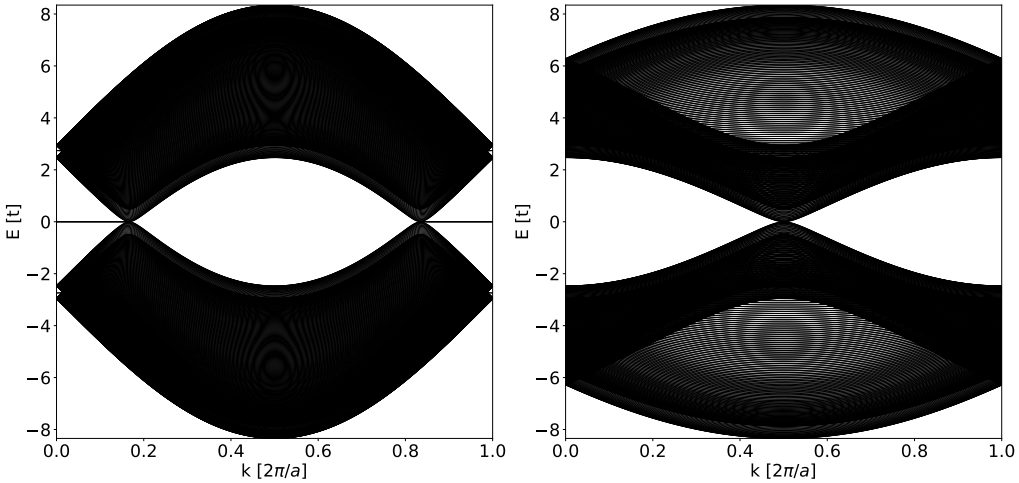

Figure 8.4: Band structures of Bernal stacked BLG nanoribbons. On the left is the zigzag nanoribbon and on the right is the armchair nanoribbon electronic structure.

Aside from the dispersion at the K-points, the nanoribbon band structures in Figure 8.4 are quite similar to those of graphene in Figure 7.3. Just as for the bulk band structure, the single sheet band structure is doubled, but shifted upwards and downwards, as expected.

8.2 Anomalous integer quantum Hall effect

The IQHE for Bernal stacked BLG is also anomalous, but different from single layer graphene. This is sensible, since the derivation of the conductance formula relied on the modeling of the electrons with a Dirac equation, which is obviously no longer possible. However, one can make topological arguments [58] to derive a conductance formula of the form

$$\sigma_{xy} = -\frac{8e^2}{h}(n+1), \quad n = 0, 1, 2, \ldots \tag{8.6}$$

The conductance step at zero energy is now no longer half the degeneracy of the other steps, but the same. This implies, that the anomaly is simply a plateau at zero energy, but the plateau step is as expected. The behavior of the different types of IQHEs is illustrated in Figure 8.5.

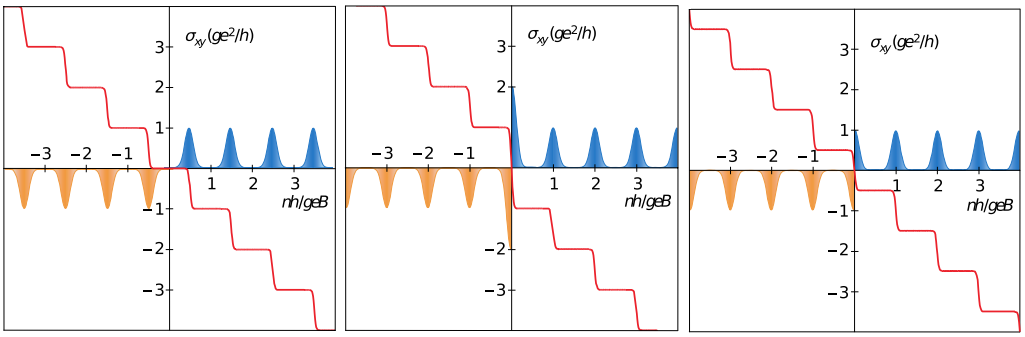

Figure 8.5: Hall conductance diagrams for three different types of materials in red. In blue are the landau levels of electrons and in orange landau levels of holes. On the left is the IQHE of a conventional superconductor and in the middle and on the right are anomalous IQHEs. Taken from [58].

There are three different types from left to right.

- Normal semiconductor: There is no conductance at zero energy.
- BLG: There is conductance at zero energy and the height of the plateau is the same as the first plateau of the semiconductor.
- Graphene: There is conductance at zero energy, but the height of the plateau is half that of the first plateau of the semiconductor.

The difference is due to the intrinsically different electron behavior around the point, where valence band and conduction band touch.

8.3 Bilayer graphene with layer switching wall

Now that the BLG material has shortly been discussed, I want to proceed to BLG with a so called LSW.

The LSW for Bernal stacked BLG at the zigzag edge is illustrated in Figure 8.6. Such domain walls have historically exhibited some interesting physical properties (polyacytelene) and as we will later see this domain wall also has physically interesting properties in an external electric field just like the Haldane model.

The model for the domain transition is quite crude, since it is rarely such a solid wall but rather an extended area, where the linear defect is situated. As such this is only a model for potentially more complicated smooth transitions, some of which will be discussed later. The LSW model consists of two separate BLG models for the left and the right region and two terms connecting the lower and the upper layer respectively.

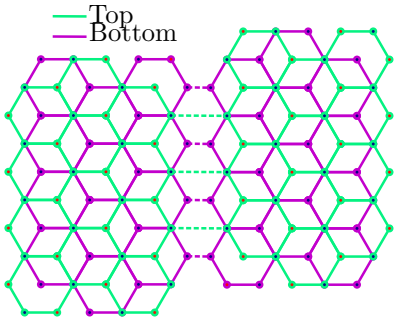

Figure 8.6: Here are two regions of Bernal stacked BLG, which are rotated about 180° with respect to each other. There is now AB-stacked graphene on the left and BA-stacked graphene on the right connected by hopping terms. The top layer is green and the bottom layer is magenta.

$$H_{\mathrm{LSW}}^{(1)} = -t_{\mathrm{LSW}}^{(1)} \sum_{\langle i,j \rangle} \left(a_i^{(1,L)}\right)^\dagger b_j^{(1,R)} + \mathrm{h.c.} \tag{8.7}$$

$$H_{\mathrm{LSW}}^{(2)} = -t_{\mathrm{LSW}}^{(2)} \sum_{\langle i,j \rangle} \left(a_i^{(2,L)}\right)^\dagger b_j^{(2,R)} + \mathrm{h.c.}, \tag{8.8}$$

where superscripts for left (L) and right (R) are now used to determine on which side of the LSW the site is. The index (1) refers to the lower layer and the index (2) refers to the upper layer. It has to be mentioned, that the angled brackets in the two terms refer to the nearest neighbour within the sheet in the other region.

The full Hamiltonian including the LSW will then read

$$H_{\mathrm{LSW}} = H_{\mathrm{BLG}}^{(\mathrm{AB,L})} + H_{\mathrm{BLG}}^{(\mathrm{BA,R})} + H_{\mathrm{LSW}}^{(1)} + H_{\mathrm{LSW}}^{(2)}. \tag{8.9}$$

Two sheets, which are coupled with the full graphene hopping integral $t_{\mathrm{LSW}} = t$ will be called **fully coupled** and the case $t_{\mathrm{LSW}} = 0$ will be called the **decoupled** regime.

8.4 Hopping integrals for arbitrary bilayer graphene systems

In the case of twist angles differing from the usual Bernal stacking or different distances between atoms due to defects like shear or tension, the model described in [59] is used to model the hopping integrals by appropriately adding models for the $pp\pi$ and for the $pp\sigma$ overlap integrals in bilayer graphene.

$$-t(\boldsymbol{R}_i, \boldsymbol{R}_j) = V_{pp\pi}\left[1 - \left(\frac{\boldsymbol{d}_z}{\|\boldsymbol{d}\|}\right)^2\right] + V_{pp\sigma}\left(\frac{\boldsymbol{d}_z}{\|\boldsymbol{d}\|}\right)^2 \tag{8.10}$$

$$V_{pp\pi} = V_{pp\pi}^0 \exp\left(-\frac{\|\boldsymbol{d}\| - a_0}{\delta}\right) \tag{8.11}$$

$$V_{pp\sigma} = V_{pp\sigma}^0 \exp\left(-\frac{\|\boldsymbol{d}\| - d_0}{\delta}\right), \tag{8.12}$$

where $\boldsymbol{d} = \boldsymbol{R}_i - \boldsymbol{R}_j$ is the site distance. The overlap integrals $V_{pp\pi}^0 \approx -2.7\,\mathrm{eV}$ and $V_{pp\sigma}^0 \approx 0.48\,\mathrm{eV}$ are the overlap integrals for Bernal stacked intralayer and interlayer nearest neighbour

overlaps respectively. The length $d_0 = 0.335\,\mathrm{nm}$ is the interlayer distance, $a_0 = 0.142\,\mathrm{nm}$ is the intralayer distance and $\delta = 0.184a$ is the modeled hopping integral decay length.

Depending on the complexity of the numerical discussion of the system and the desired accuracy of the results, an appropriate cutoff distance for these hopping integrals must be chosen. The generic BLG Hamiltonian can then be written as

$$H_{\mathrm{TBLG}} = -\sum_{(i,j)} t(\boldsymbol{R}_i, \boldsymbol{R}_j)\, |i\rangle \langle j| + \mathrm{h.c.}, \tag{8.13}$$

where the bracket (i, j) denotes the proper cutoff.

8.5 Bilayer graphene with layer switching wall in an external electric field

This section is dedicated to reviewing the main results from [60] and introducing an example of a weak topological invariant. It serves as a motivation for investigating domain walls in general as well.

Consider an LSW with bulk BLG to the left and right of it, rotated by 180° with respect to each other. They are denoted AB and BA stacking to emphasize the transition from left to right side by rotation about 180° or reflection along the LSW. The left and the right bulk have thus the same energy spectrum and physical properties. This symmetry is broken by application of an external electric field. This symmetry breaking causes the formation of topological currents along the LSW.

The Berry curvature is [60]

$$\Omega_\nu(\boldsymbol{q}) = \frac{-2\mu\nu\gamma\Delta q^2}{q^4 + \gamma^2\Delta^2}, \tag{8.14}$$

where Δ is the difference in onsite potential between sheets, $\nu = 1$ when closer to $\boldsymbol{K}$ and $\nu = -1$ when closer to $\boldsymbol{K}'$, γ is a normalized energy scale of the system and $\mu = 1$ for AB stacking and $\mu = -1$ for BA stacking.

Integrating this over the whole Brillouin zone gives zero. However, one can define valley spin Chern numbers, where the Brillouin zone is only integrated in the valley corresponding to $\boldsymbol{K}$ or $\boldsymbol{K}'$ respectively and get

$$N_\nu = -\mu\nu\,\mathrm{sign}(\Delta). \tag{8.15}$$

This implies, that crossing an LSW yields a absolute difference in valley Chern number of two for each valley. Due to the bulk boundary correspondence, there should be two topologically protected modes propagating at the LSW.

These topologically protected modes can be seen in the one dimensional band structures of the materials including the LSW in Figure 8.7. For all three tunneling parameters between left and right region, the topologically protected chiral edge modes in yellow and green are present. For $t^{(1)}_{\mathrm{LSW}} > \Delta$, there appears a third gapless mode due to the splitting of the initially gapless magenta bands. This is due to the fact, that the LSW tunneling induces valley scattering and invalidates valley isospin as a good quantum number.

This valley Chern number is not an actual topological invariant, since the only the total Chern number is an invariant, since the entire Brillouin zone must be integrated to define a topological invariant. The topological protection of the edge modes is broken by scattering between the valleys $\boldsymbol{K}$ and $\boldsymbol{K}'$ as seen in the discussion of Figure 8.7.

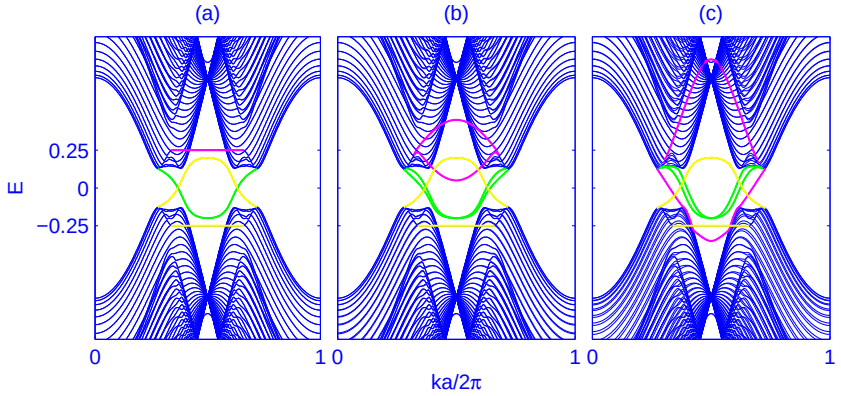

Figure 8.7: Gapless modes in external electric field $\Delta = 0.5$ gapping the BLG. In all cases $t^{(2)}_{\mathrm{LSW}} = 0$ and $t^{(1)}_{\mathrm{LSW}} = 0.0, 0.2, 0.6$ from left to right. Green ,yellow and magenta states have degeneracy two. Taken from [60].

8.6 Transport through layer switching wall networks in bilayer graphene and production methods

As discussed, AB and BA stacking are energetically equivalent. In the production of BLG sheet, regions of AB and BA stacking appear naturally with domain walls between them due to the energy degeneracy. Depending on the production method, the density of these linear defects varies.

I want to focus on the production method used in the experimental setup of [11] described in [61, 62], since I wish to examine the dislocation network modeled by the hard wall model mentioned earlier and other models, which will be introduced in chapter 9.

The graphene layers are grown on a substrate, in this case SiC, by epitaxy. LSWs as described previously naturally form in this process.

An example for these dislocation networks in shown in Figure 8.8. An the length scale of 100 nm, there are tens of LSWs along a line, depending on the exact local geometry of the material.

The particular nature of these defects depends on their origin, but a reasonable model for defects along the respective nanoribbons are sheared and tensed regions of the system leading to a smooth transition between the stackings [63]. Models for tensile and shear transition will be discussed in chapter 9.

8.7 Bilayer graphene with twist angle

As mentioned, BLG can be classified by a twist angle θ with respect to the initial AA stacking and the images in Figure 8.9 contain some twist angle BLG systems.

One remark is on the size of the unit cell. It should be clear, that the unit cell for 0° is simply the single graphene layer unit cell. The 60° case is Bernal stacked graphene and the unit cell only contains 4 sites as well. For 30°, the unit cell is clearly larger and for 15° it is even larger still. In general, a supercell for the resulting Moire pattern must be defined. Especially small twist angles are of interest since the recent discovery of unconventional superconductivity at magic twist angles 1.16° and 1.05° [57].

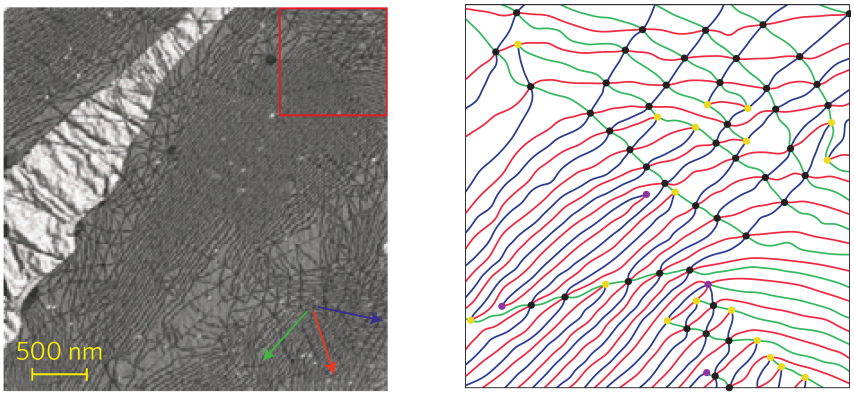

Figure 8.8: Left image: Partial dislocation network in a bilayer membrane originating from epitaxial graphene on SiC(0001). The image shows a composite (or superposition) of three dark-field TEM images, taken with the three {1120} reflections, such that the full network of partial dislocations is revealed, providing the mosaic tiling of bilayer graphene. Right image: Partial dislocation network in which the color encodes the crystallographic Burgers vector associated with the partial dislocations as extracted from the individual dark-field TEM data (red square on the left). Extracted including caption from [11].

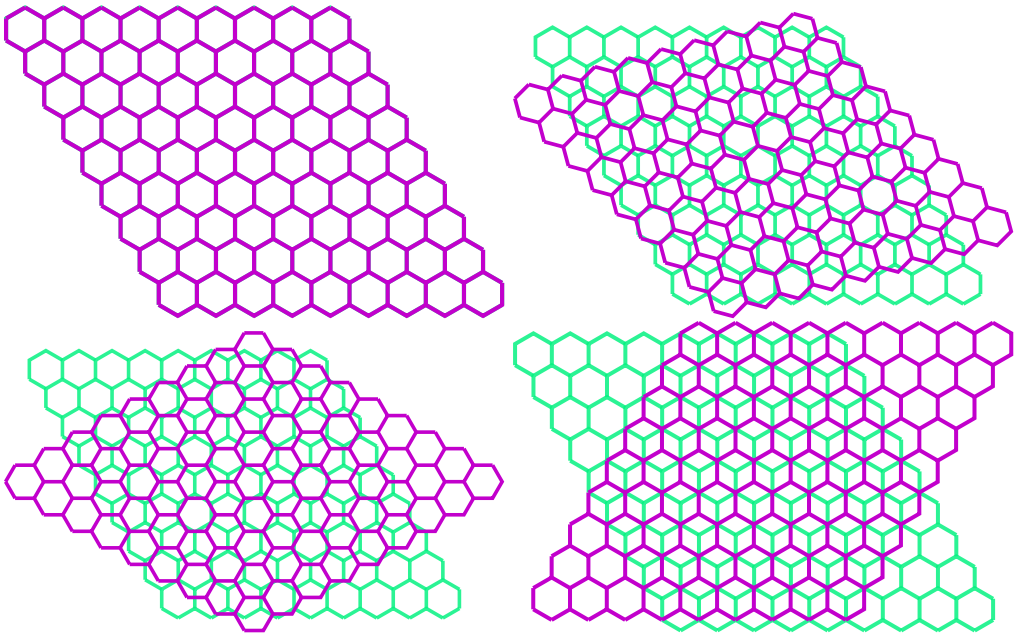

Figure 8.9: Here are some examples for twisted bilayer graphene (TBLG) with large twist angles. The twist angles are from top left to bottom right $\theta = 0°$, $\theta = 15°$, $\theta = 30°$ and $\theta = 60°$. The rotation center is directly on one site of the B sublattice of the upper layer. For these diagrams, the coloring of sites is omitted.

Chapter 9

Results for bilayer graphene

There are several models for a BLG system with LSW, depending on the particular situation. In this thesis, a hard wall model for the LSW, a LSW due to shear and a LSW due to tension will be investigated.

The initial goal of the implementation of several invariant calculations described in previous chapters, either with direct Chern number calculations or local index calculations, was to apply them to the models mentioned. However, these systems must be large enough to support edge modes due to the IQHE without finite-size effects, since the external magnetic field induces a natural length scale into the problem. The system sizes required for the elimination of finite-size effects are simply too large to apply any of these methods, since they require the diagonalization of a significant part of the total system Hamiltonian.

The implementation of the transport calculation however was adequate to handle systems large enough such that finite-size effects could be controlled. The rest of this chapter contains these transport calculations.

9.1 Bilayer graphene models

Layer switching in a real material usually occurs due to tension or shear in the system as shown in Figure 9.1.

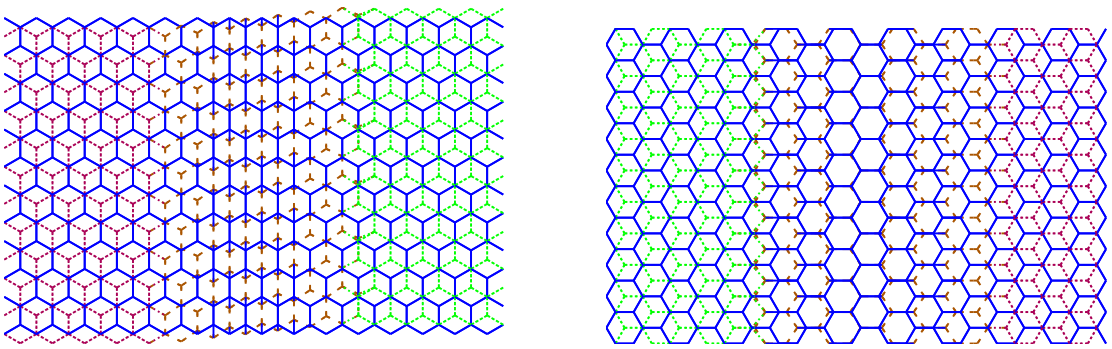

Figure 9.1: Heterogeneous systems with LSWs containing BLG under shear (left) and tension (right). The lower layer is the solid blue lattice. The upper layer is in both cases either dotted or striped in green, orange and red respectively. Only the nearest neighbour terms are shown.

The SLSW is along the armchair nanoribbon direction and the tension layer switching wall (TLSW) is along the zigzag nanoribbon direction. Depending on the interaction cutoff (see description of system parameters for definition) in the numerical discussion this model is fairly realistic when describing a system in which layer switching occurs smoothly.

A simplification for the layer switching due to tension which is often used, for example when discussing protected topological modes in an external electric field, is the HLSW model depicted in Figure 9.2. On the left is a homogeneous system as reference.

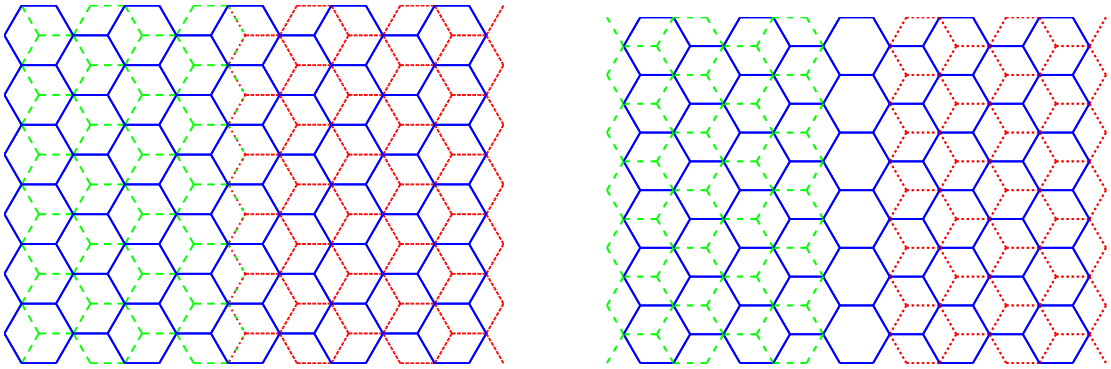

Figure 9.2: Homogeneous and HLSW system. The lower layer is in blue and the upper layer is striped or dotted in red and green. On the left is a homogeneous AB stacked BLG system, which will be used as a reference system. On the right is the hard wall model for a LSW at the zigzag nanoribbon. The upper layer is decoupled, but any effective interaction may be of interest, in particular a fully covered upper layer.

The same simplification is in principle possible for an LSW in the zigzag nanoribbon direction, i.e. for the LSW due to shear. This simplification however is not discussed in the mainstream literature as far as I am aware.

To discuss the details of the IQHE, a system with only one terminal to measure conductivity is not sufficient. The generic measurement apparatus, which I will call a Hallbar from now on, is shown in Figure 9.3.

The region of interest, i.e. the sheared and tensed parts of the system are inserted in the middle of the Hallbar. This allows for discussion of the longitudinal and transverse conductance and for the observation of reflection due to the introduced LSWs. Electrons in this geometry are injected from R and BL.

For the following discussion of sheared, tensed and hard wall systems I introduce the following definitions and nomenclature

- L_t: Tension length parameter. The width of the TLSW is $2L_t a_{cc}$. The quantity $1 + 1/L_t$ is the magnitude of the tension applied.
- L_s: Shear length parameter. The width of the SLSW is $0.57L_s a$. The quantity $1/L_t$ is the magnitude of the shear applied.
- N_T: Number of sites in the transmission calculation.
- N_L: Number of sites in the LDOS calculation.
- D_c: Cutoff distance for hopping integrals between layers in the LSW, where the graphene layers are thought of as being at the same distance as two nearest carbon atoms within a

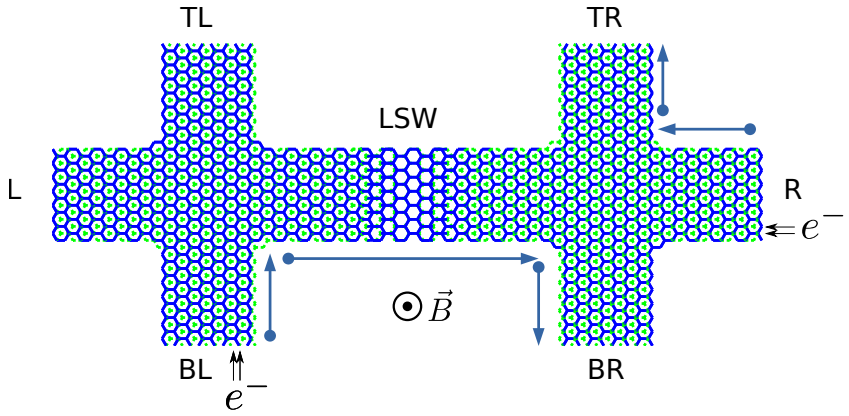

Figure 9.3: Hallbar system with TLSW. The lower graphene layer is solid blue and the upper layer is striped green. This is the generic system which will be used to discuss the IQHE in inhomogenous or homogeneous BLG systems in this section. It is a six-terminal structure with a lead applied at each of the labels L, R, BL, BR, TL and TR. The electron propagation in a homogeneous medium is indicated by blue arrows. The electron injection electrodes are also indicated with arrows. R stands for *right*, L stands for *left*, T stands for *top* and B stands for *bottom*.

layer, $d_0 = a_{cc}$. The interaction within a layer is always a nearest neighbour interaction. This parameter only makes sense in the context of sheared or tensed systems.

- $\phi^{-1}_{\mathrm{LDOS}}$: Magnetic field value for the LDOS calculation. This value represents a physical magnetic field, but the Fermi energies for the transport calculations were chosen to be very large to suppress finite size effects. For this reason the resulting magnetic fields would be unphysically large. Thus this is kept as a parameter $\phi^{-1}_{\mathrm{LDOS}}$ and not converted into a Tesla. I still argue for the genericity of the results in section 9.8.
- E_F: Fermi energy at which the calculations take place.

Here a_{cc} is the graphene carbon-carbon distance and a is the lattice spacing. The following parameters are fixed in all calculations presented in this chapter

- The Fermi energy, at which the calculation is performed is $E_F = 0.35t \approx 0.95\,\mathrm{eV}$
- A random onsite disorder for all calculations is Gaussian noise with a width of $\Delta = 0.05t$ around zero.

The following sections will be the discussions of calculations of densities and conductance diagrams for the various systems that were just introduced.

9.2 Results for AB stacking bilayer graphene

First, I review the IQHE results for a homogeneous BLG system as reference. Spin is not accounted for in these calculations, so the results have to be multiplied by two for comparison with real systems.

The calculations of transport and LDOS are displayed in Figure 9.4. The results show the plateaus expected for an anomalous IQHE for BLG. The conductance at zero energy is $\sigma = 2\sigma_0$

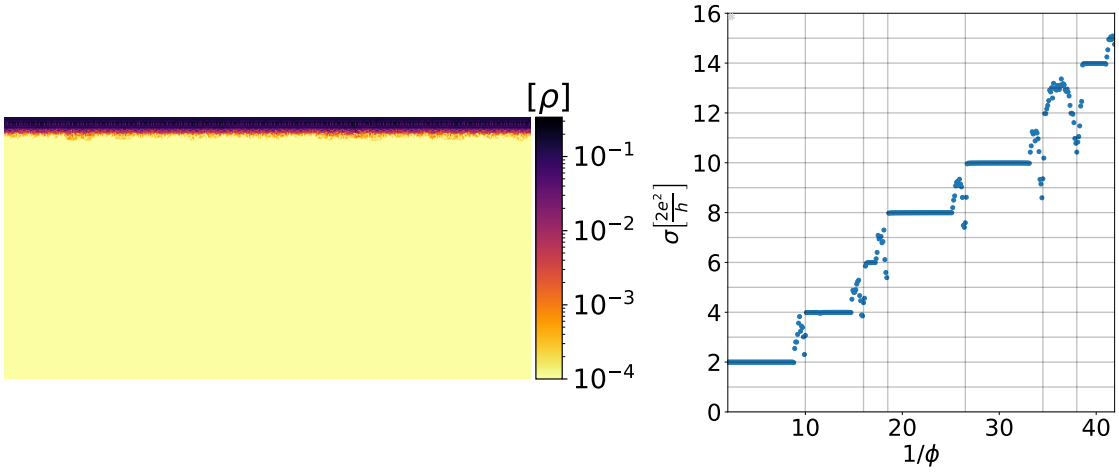

Figure 9.4: **Slab plot** for a homogeneous AB stacked system. On the left is a logarithmic plot of the LDOS ρ due to electron injection from L with a cutoff at 1×10^{-4}. The symbols for left and right electrode are adopted from Figure 9.3. On the right is the corresponding transmission diagram from L to R. The LDOS calculation is performed at an external magnetic field $\phi_{\mathrm{LDOS}}^{-1} = 10.5\phi_0^{-1}$. The number of sites contained in the system used for the LDOS calculation is $N_L \approx 6.5 \times 10^5$. The number of sites contained in the system used for the transmission calculation is $N_T \approx 6.5 \times 10^5$.

and the plateau transition steps have height $\sigma = 2\sigma_0$ as well. The widths of the plateaus vary due to the electronic structure of bilayer graphene at zero magnetic field causing the condensation of bulk states into Landau levels at electronic structure dependent energies.

Another reference calculation is performed and shown in Figure 9.5 for the Hallbar geometry introduced in Figure 9.3.

The results for the LDOS and the transmission calculations are as expected for a system in the IQHE regime. The LDOS shows localization of edge states with consistent magnetic current direction (clockwise). The plateau width is the same as for the **Slab plot** in Figure 9.4. However, the characteristic longitudinal conductances of the IQHE at the plateau transitions can also be observed in the transmission plot. The delocalization and scattering into states, that may transmit to any of the sink electrodes, is expected at the plateau transitions.

9.3 Results for hard wall model

The HLSW system as sketched in Figure 9.2 is a simple model for a transition between stacking regimes of BLG. Whether the hard wall is a good model for either sheared or tensed systems is the central interest of this discussion. Since the hopping elements, particularly in the upper layer, are effective interactions between the stacking regions, they may be tuned freely. The LDOS plot does not show many details of the electron transmission. Due to this, I will only show an example for the LDOS in a slab and for the LDOS in a Hallbar for each system type. Further studies of dependencies on system parameters are performed by only examining the transmission calculations and not the LDOS calculations.

The transmission calculation through a slab in Figure 9.6 of a hard wall system already shows significant differences to the homogeneous BLG system, in the LDOS and the transmission function. There is no clearly defined plateau structure in the transmission function, which would

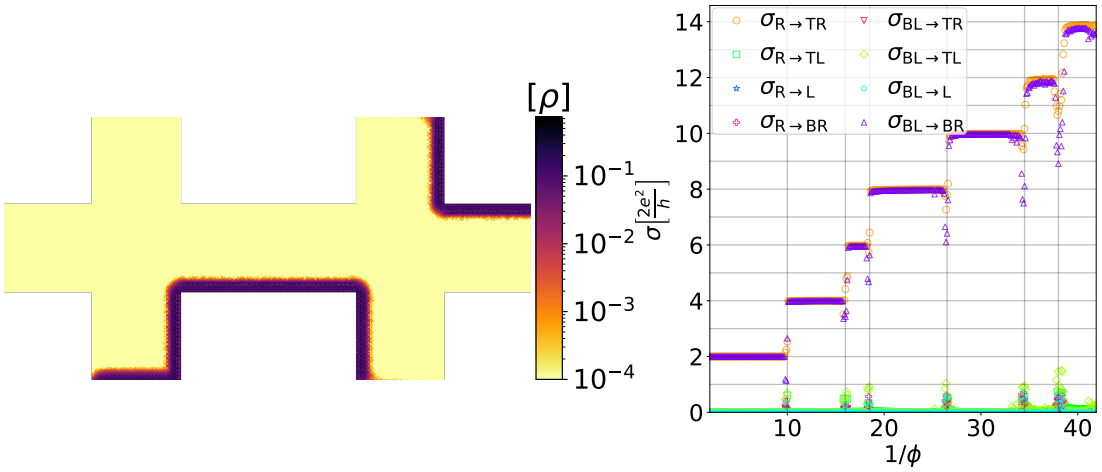

Figure 9.5: **Hallbar plot** for a homogeneous AB stacked Hallbar system. On the left is a logarithmic plot of the LDOS due to electron injection from the lower left and right lead with a cutoff at 1×10^{-4}. On the right are the elements of the conductance tensor. The different conductances always have different colors and marker styles. The indices for the conductances are as indicated in Figure 9.3. The LDOS calculation is performed at an external magnetic field $\phi_{\text{LDOS}}^{-1} = 10.5\phi_0^{-1}$. The number of sites contained in the system used for the LDOS calculation is $N_L \approx 5 \times 10^5$. The number of sites contained in the system used for the transmission calculation is $N_T \approx 1.5 \times 10^5$.

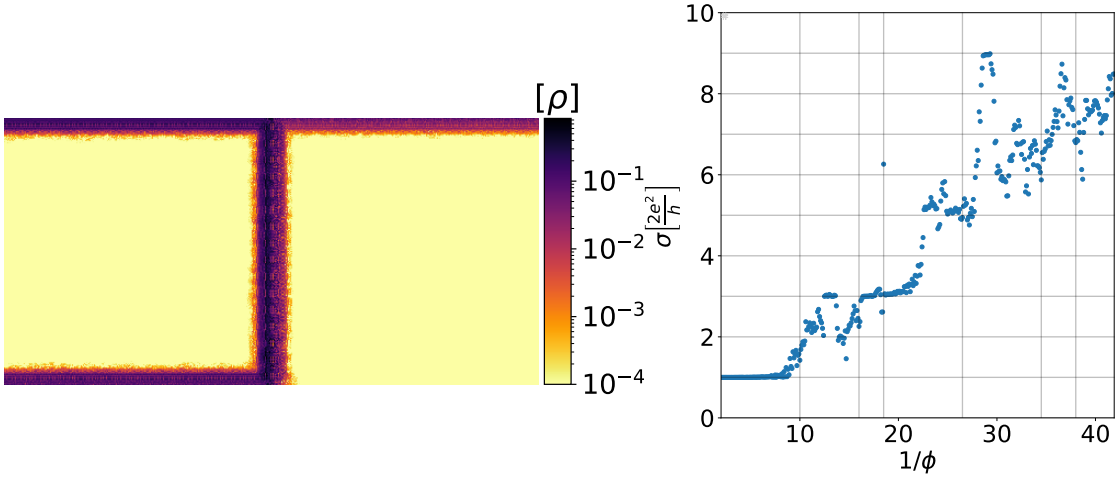

Figure 9.6: **Slab plot**, see Figure 9.4, for a system with HLSW. The LDOS calculation is performed at an external magnetic field $\phi_{\text{LDOS}}^{-1} = 10.5\phi_0^{-1}$. The lower layer is fully coupled $t_{\text{LSW}}^{(1)} = t$. The upper layer is decoupled $t_{\text{LSW}}^{(2)} = 0$. The number of sites contained in the system used for the LDOS calculation is $N_L \approx 6.5 \times 10^5$. The number of sites contained in the system used for the transmission calculation is $N_T \approx 6.5 \times 10^5$.

be expected for the IQHE and the reason can be seen in the LDOS plot. The edge modes of the IQHE tend to propagate along the LSW and reflect back into the left part of the system.

There is some correlation between plateaus in the homogeneous system and the structure of the transmission for this system, but the transmission function is unexpectedly chaotic and we therefore turn to the Hallbar system for more insights.

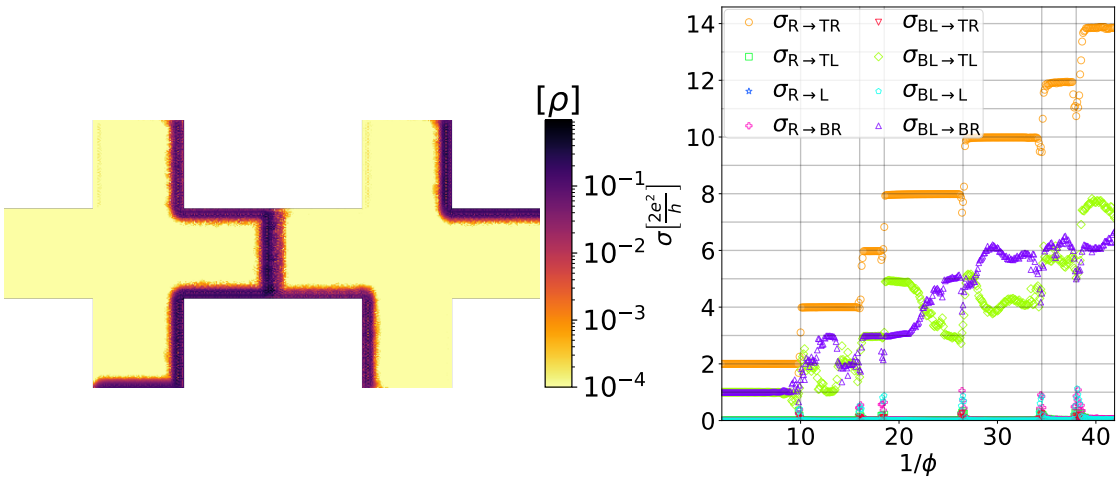

Figure 9.7: **Hallbar plot**, see Figure 9.5, for a Hallbar system with HLSW. The LDOS calculation is performed at an external magnetic field $\phi_{\mathrm{LDOS}}^{-1} = 10.5\phi_0^{-1}$. The lower layer is fully coupled $t_{\mathrm{LSW}}^{(1)} = t$. The upper layer is decoupled $t_{\mathrm{LSW}}^{(2)} = 0$. The number of sites contained in the system used for the LDOS calculation is $N_L \approx 5 \times 10^5$. The number of sites contained in the system used for the transmission calculation is $N_T \approx 1.5 \times 10^5$.

The results for the Hallbar geometry of the HLSW with decoupled upper layer are shown in Figure 9.7. Just as in the case of the slab geometry, there is clear propagation along the LSW and the mode from R to TR is unperturbed by the change in geometry, as expected. The transmission diagram confirms, that the transmission from R to TR is unperturbed.

The transmission from BL to BR and from BL to TL however, shows interesting structure. For a homogeneous BLG system, one would expect the zero energy conductance to be $\sigma_{\mathrm{BL}\to\mathrm{BR}} = 2\sigma_0$ and $\sigma_{\mathrm{BL}\to\mathrm{TL}} = 0$. In this case, both have the value σ_0, which reflects the fact, that only one of the graphene layers is coupled and the zero energy mode in the upper layer cannot propagate to BR.

As expected, the transmissions fulfill $\sigma_{\mathrm{BL}\to\mathrm{BR}} + \sigma_{\mathrm{BL}\to\mathrm{TL}} = \sigma_{\mathrm{R}\to\mathrm{TR}}$, which reinforces the intuition, that the modes propagating from BL to BR simply propagate along the introduced LSW. $\sigma_{\mathrm{BL}\to\mathrm{BR}}$ and $\sigma_{\mathrm{BL}\to\mathrm{TL}}$ have about the same magnitude averaged across a single plateau, which is reminiscent of the splitting of the zero energy modes. The propagation contributing to $\sigma_{\mathrm{BL}\to\mathrm{TL}}$ seems to be preferred in the middle of a plateau and $\sigma_{\mathrm{BL}\to\mathrm{BR}}$ at the edges of a plateau, which is likely due to a similar effect as the existence of the longitudinal conductance in a homogeneous system. At the beginning and end of the plateau, there exist states to scatter into, that are filled in the middle of the plateau thus making transmission along the LSW more likely.

In Figure 9.8, the transmission diagram for $t_{\mathrm{LSW}}^{(2)} = t$ is shown. The transmission from R to TR is unchanged, as expected. The transmissions $\sigma_{\mathrm{BL}\to\mathrm{BR}}$ and $\sigma_{\mathrm{BL}\to\mathrm{TL}}$ are in contrast entirely different. At zero energy, the zero energy states do not split as is the case for $t_{\mathrm{LSW}}^{(2)} = 0$, since there is no need for the state in the upper layer to propagate along the LSW. Similar to the previous case $\sigma_{\mathrm{BL}\to\mathrm{BR}} + \sigma_{\mathrm{BL}\to\mathrm{TL}} = \sigma_{\mathrm{R}\to\mathrm{TR}}$ near plateau centers, since the transmission either transmits across the LSW or propagates along it. The transmission $\sigma_{\mathrm{BL}\to\mathrm{TL}}$ is in general much

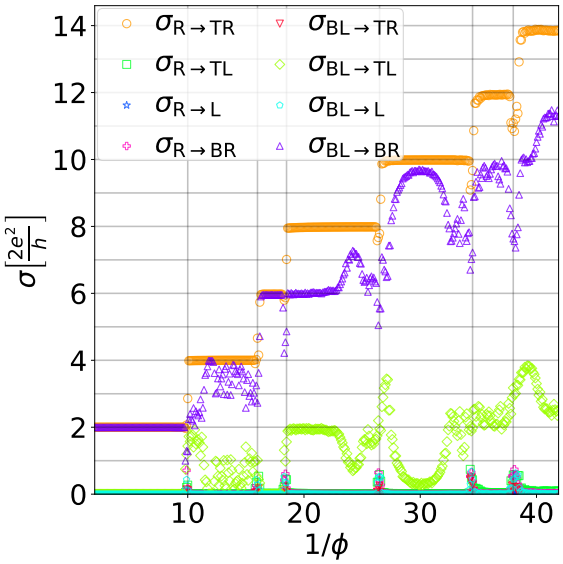

Figure 9.8: Transmission calculation like in **Hallbar plot**, see Figure 9.5, for a Hallbar system with HLSW. The lower layer is fully coupled $t^{(1)}_{\mathrm{LSW}} = t$. The upper layer is fully coupled $t^{(2)}_{\mathrm{LSW}} = t$. The number of sites contained in the system used for the transmission calculation is $N_T \approx 1.5 \times 10^5$.

,

smaller than for decoupled upper layers, propagation in the upper layer is now no longer confined to the left half of the system. Here the transmission $\sigma_{\mathrm{BL}\to\mathrm{BR}}$ is preferred in the middle of plateaus rather than at plateau transitions. A similar explanation as in the previous case is reasonable.

Thus the case $t^{(2)}_{\mathrm{LSW}} = t$ is not qualitatively different from $t^{(2)}_{\mathrm{LSW}} = 0$, but rather different in the specific numerical values of the transmissions, which is intuitive.

9.4 Results for layer switching wall due to shear

This section contains calculations for systems with SLSW depicted in Figure 9.1. Since the LSW here is along the armchair ribbon, this model is fundamentally different from all other models investigated in this thesis. The SLSW is also a good model for transitions due to TBLG and is therefore particularly interesting.

The density calculation and transmission calculation for a BLG slab with SLSW are displayed in Figure 9.9. Just as for the HLSW system the LDOS calculation shows an increased density in the region of the LSW. The transmission calculation reflects this increase. The transmission calculation resembles a conventional quantum Hall effect except for the increases and decreases in conductivity around plateau transitions. In the homogeneous system in Figure 9.4, there are seven plateaus in the interval being studied. In the calculation for the SLSW system in Figure 9.9, there are only four plateaus in this interval and the plateau transitions for the homogeneous and SLSW case do not coincide. The transmission has additional structure, which mostly corresponds to plateau transitions in the homogeneous material, where there are none in the BLG system with SLSW. In the Hallbar calculation, there is an explicit comparison to a homogeneous material, so I will continue the discussion with the Hallbar system.

The results for the equivalent Hallbar system are shown in Figure 9.10. Just as for the slab calculation the LDOS calculation for the Hallbar shows an increased density in the LSW region. Due to the small size of the LSW there is no way to distinguish contributions to the conductance due to the tranisition from AB or BA to LSW and contributions in the center of the LSW. As expected, the transmission from R to TR, $\sigma_{\mathrm{R}\to\mathrm{TR}}$, is not affected by the introduction of an SLSW into the system since AB and BA stacking are equivalent without external electric field. Just as

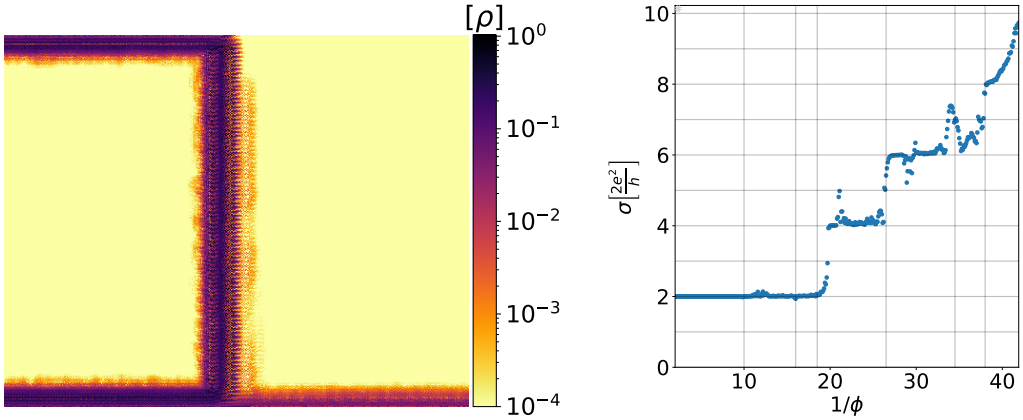

Figure 9.9: **Slab plot**, see Figure 9.4, for a SLSW system. The LDOS calculation is performed at an external magnetic field $\phi_{\text{LDOS}}^{-1} = 10.5\phi_0^{-1}$. The cutoff between the two layers in the LSW is short, $D_c = 1.3a_{cc}$. The shear width parameter is $L_S = 44$. The number of sites contained in the system used for the LDOS calculation is $N_L \approx 4.1 \times 10^5$. The number of sites contained in the system used for the transmission calculation is $N_T \approx 1.2 \times 10^5$.

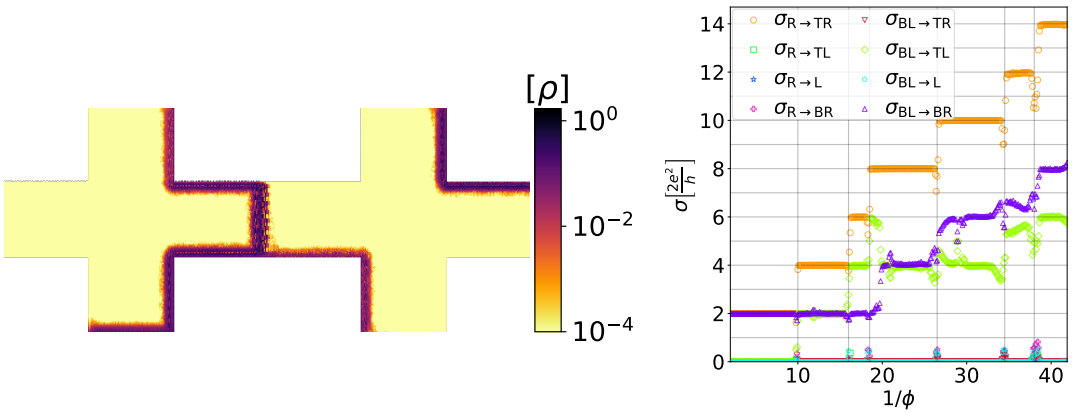

Figure 9.10: **Hallbar plot**, see Figure 9.5, for a Hallbar system with SLSW. The LDOS calculation is performed at an external magnetic field $\phi_{\text{LDOS}}^{-1} = 10.5\phi_0^{-1}$. The cutoff between the two layers in the LSW is long, $D_c = 4a_{cc}$. The shear width parameter is $L_S = 44$. The number of sites contained in the system used for the LDOS calculation is $N_L \approx 1.2 \times 10^6$. The number of sites contained in the system used for the transmission calculation is $N_T \approx 2.3 \times 10^5$.

for the HLSW case, $\sigma_{\text{BL}\to\text{BR}} + \sigma_{\text{BL}\to\text{TL}} \approx \sigma_{\text{R}\to\text{TR}}$ near plateau centers, which should be the case if there are minimal finite-size effects. The transmission function is structurally similar to the slab calculation in Figure 9.9, but there are differences between the transmission in Figure 9.9 and $\sigma_{\text{BL}\to\text{BR}}$ in Figure 9.10. I should mention, that the slab system is larger than the corresponding central region in the Hallbar system, since the simulation of more electrodes introduces more complexity into the calculation. A discussion of finite-size effects in section 9.6 will illuminate this aspect of the differences between the transmission functions. Ignoring regions close to plateau transitions in $\sigma_{\text{R}\to\text{TR}}$, both $\sigma_{\text{BL}\to\text{BR}}$ and $\sigma_{\text{BL}\to\text{TL}}$ approximately have a monotonically increasing plateau structure characteristic of an IQHE. The conductance jumps of $\sigma_{\text{BL}\to\text{BR}}$ and $\sigma_{\text{BL}\to\text{TL}}$

coincide with conductance jumps in $\sigma_{\mathrm{R}\to\mathrm{TR}}$. There is however no obvious frequency with which the conductances $\sigma_{\mathrm{BL}\to\mathrm{BR}}$ and $\sigma_{\mathrm{BL}\to\mathrm{TL}}$ jump, since they are sometimes constant over the range of two plateaus in $\sigma_{\mathrm{R}\to\mathrm{TR}}$ and sometimes only over the range of one plateau. The magnitude and structure of the conductances is more similar to the $t^{(2)}_{\mathrm{LSW}} = 0$ case than the $t^{(2)}_{\mathrm{LSW}} = t$ case, but neither have conductance functions that are particularly similar to Figure 9.10.

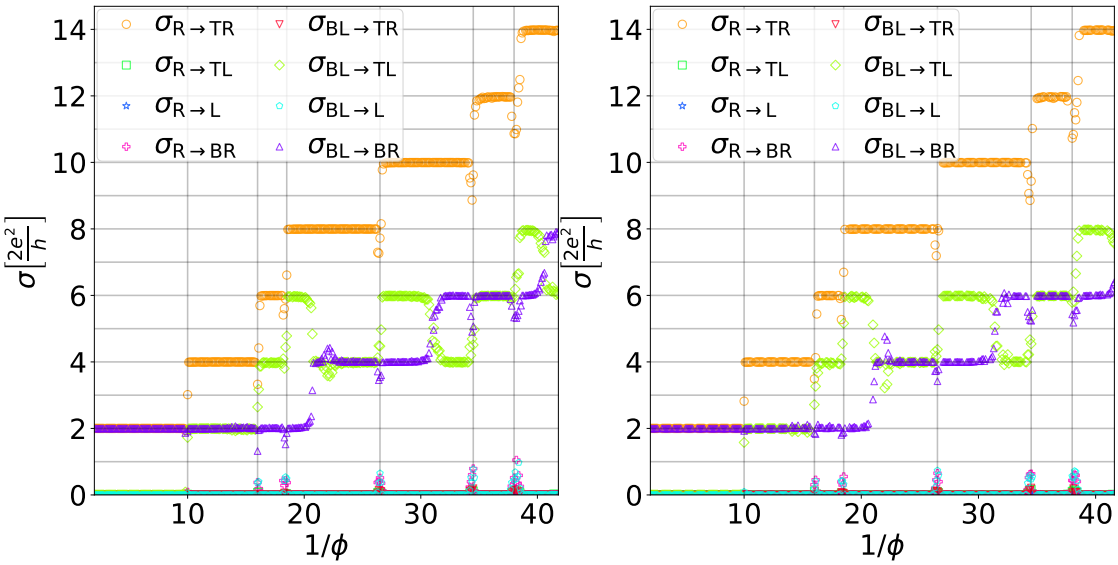

Figure 9.11: Transmission calculation like in **Hallbar plot**, see Figure 9.5, for a Hallbar system with SLSW. The cutoff between the two layers in the LSW is long, $D_c = 4a_{cc}$. On the left $L_s = 100$ and on the right $L_s = 150$. For both calculations The number of sites contained in the system used for the transmission calculation is $N_T \approx 2.3 \times 10^5$.

The case $L_s = 44$ is the intermediate length scale of a SLSW, but a particularly interesting case is the limit of an infinitely long SLSW describing a very smooth transition from AB to BA stacking. The examination of this limit is shown in Figure 9.11. Aside from the very edge of the magnetic field interval under consideration, the case $L_s = 100$ and $L_s = 150$ have essentially identical conductance diagrams. This hints towards convergence of the conductance with respect to the LSW width, which will be more thoroughly examined in section 9.10. It is also sensible, that the convergence of the conductance would depend on the value of the external magnetic field, since the magnetic length would be larger for larger ϕ^{-1}. The conductance $\sigma_{\mathrm{BL}\to\mathrm{TL}}$ is no longer approximately monotonous, but the conductance $\sigma_{\mathrm{BL}\to\mathrm{BR}}$ shows more obvious plateaus than the $L_s = 44$ case. There are still features due to plateau transitions in $\sigma_{\mathrm{R}\to\mathrm{TR}}$, where none in $\sigma_{\mathrm{BL}\to\mathrm{TL}}$ occur, but they are far less pronounced than for a smaller SLSW. Since the reduced features were increases in $\sigma_{\mathrm{BL}\to\mathrm{TL}}$ it makes sense, that they are reduced by a larger SLSW.

9.5 Results for layer switching wall due to tension

This section contains calculations for BLG systems with a TLSW depicted in Figure 9.1. One may interpret the HLSW as an effective model for the TLSW. Thus it would stand to reason to expect similar results, if the hard wall is an adequate model.

The LDOS calculation and transmission calculation for a BLG slab with TLSW are displayed

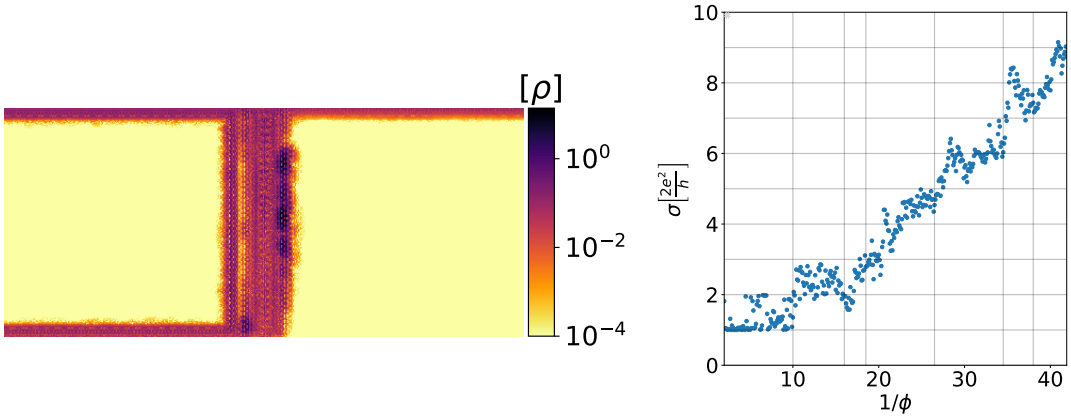

Figure 9.12: **Slab plot**, see Figure 9.4, for a tensed system. The LDOS calculation is performed at an external magnetic field $\phi_{\text{LDOS}}^{-1} = 10.5\phi_0^{-1}$. The cutoff between the two layers in the LSW is short, $D_c = 1.3a_{cc}$. The tension length parameter is $L_T = 60$. The number of sites contained in the system used for the LDOS calculation is $N_L \approx 4.7 \times 10^5$. The number of sites contained in the system used for the transmission calculation is $N_T \approx 1.4 \times 10^5$.

in Figure 9.12. The LDOS calculation also shows conductance along the TLSW, as expected by now. However, the contributions to the propagation along the LSW are now clearly extended in the entire LSW, which was not clear in the SLSW case. The contribution to the conductance due to the transition from left system side to LSW is also clearly distinguished. Considering that the propagation of modes in the applied external magnetic field must be clockwise, the only explanation for the propagation along the right side of the LSW is that the contribution was first transmitted through the LSW. The transmission function in Figure 9.12 does not show a clear plateau structure like Figure 9.9. Some features could be identified as plateaus, but the structure is mostly chaotic.

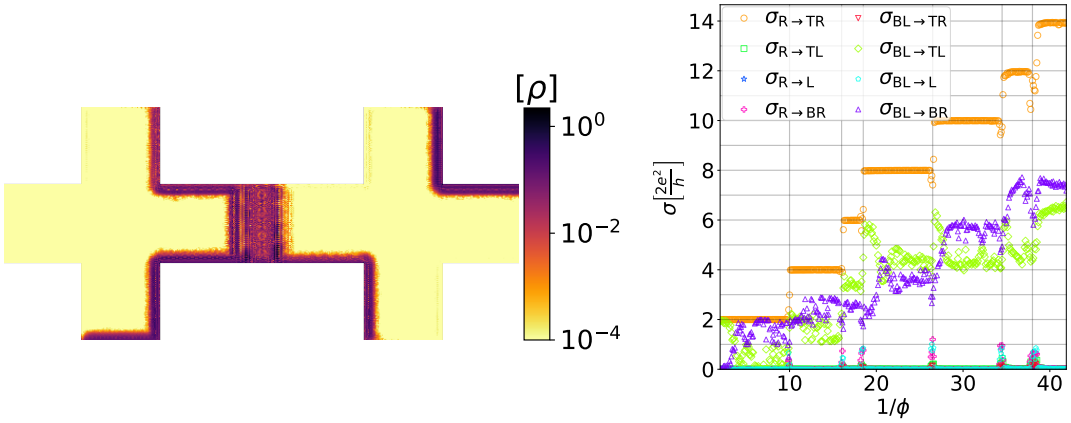

Figure 9.13: **Hallbar plot**, see Figure 9.5, for a tensed system. The LDOS calculation is performed at an external magnetic field $\phi_{\text{LDOS}}^{-1} = 10.5\phi_0^{-1}$. The cutoff between the two layers in the LSW is short, $D_c = 1.3a_{cc}$. The tension length parameter is $L_T = 60$. The number of sites contained in the system used for the LDOS calculation is $N_L \approx 8.1 \times 10^5$. The number of sites contained in the system used for the transmission calculation is $N_T \approx 2.0 \times 10^5$.

The results for the equivalent Hallbar system are shown in Figure 9.13. The LDOS calculation for the Hallbar system yields essentially the same result as shown in Figure 9.12 with an additional mode from R to TR. The conductivities $\sigma_{\mathrm{BL}\to\mathrm{TL}}$ and $\sigma_{\mathrm{BL}\to\mathrm{BR}}$ still show more chaotic structure than the SLSW system and plateaus are not as clearly distinguishable. When away from the edges of plateaus however, $\sigma_{\mathrm{BL}\to\mathrm{TL}}$ and $\sigma_{\mathrm{BL}\to\mathrm{BR}}$ are constant up to fluctuations of the order of σ_0. These deviations are significant and make the characterisation into plateaus difficult, but this points to some genericity of the development of a plateau-like structure in $\sigma_{\mathrm{BL}\to\mathrm{BR}}$ albeit with different plateau transitions than $\sigma_{\mathrm{R}\to\mathrm{TR}}$. When close to the edge of a plateau, $\sigma_{\mathrm{BL}\to\mathrm{TL}}$ increases and $\sigma_{\mathrm{BL}\to\mathrm{BR}}$ decreases due to the availability of states to scatter into, that contribute to transverse conductance. As opposed to the SLSW calculation $\sigma_{\mathrm{BL}\to\mathrm{BR}}$ is not $2\sigma_0$ across the first plateau similar to the $t^{(2)}_{\mathrm{LSW}} = 0$ case for a HLSW system. Since the classification into plateaus is not obvious for the $L_t = 60$ case, larger TLSW calculations might decrease the fluctuations just as for the SLSW system.

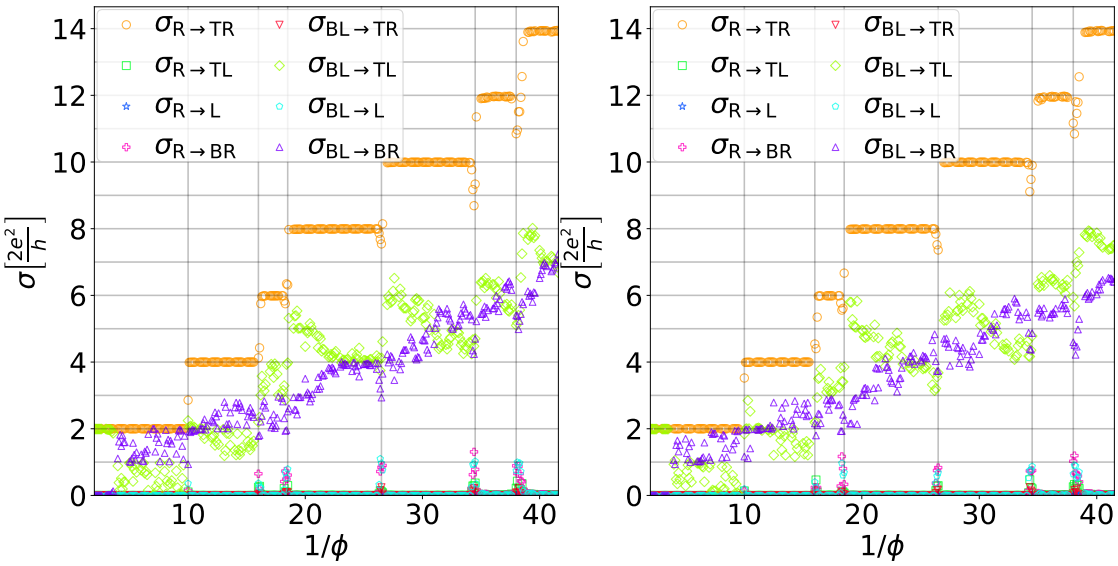

Figure 9.14: Transmission calculation like in **Hallbar plot**, see Figure 9.5, for a tensed Hallbar system. The cutoff between the two layers in the LSW is long, $D_c = 4a_{cc}$. On the left $L_t = 100$ and on the right $L_t = 100$. For both calculations The number of sites contained in the system used for the transmission calculation is $N_T \approx 2.0 \times 10^5$.

The calculation for larger TLSW widths is shown in Figure 9.14. Unlike the SLSW system, there is no obvious formation of plateaus in $\sigma_{\mathrm{BL}\to\mathrm{BR}}$ even for large values of L_t. For larger magnetic fields, there are regions where the conductances only vary between neighbouring conductance quanta. In the interval $\phi^{-1} \in [0, 10]$, $\sigma_{\mathrm{BL}\to\mathrm{BR}} \in [\sigma_0, 2\sigma_0]$ and for $\phi^{-1} \in [10, 19]$, $\sigma_{\mathrm{BL}\to\mathrm{BR}} \in [2\sigma_0, 3\sigma_0]$. The last interval where is this obvious is $\phi^{-1} \in [22, 28]$, where $\sigma_{\mathrm{BL}\to\mathrm{BR}} \in [4\sigma_0, 5\sigma_0]$. Similarly to the SLSW case it is sensible, that these properties would depend on the particular value of the external magnetic field and a more exhaustive study will be performed in section 9.11.

9.6 Discussion of finite-size effects

I have mentioned in the introduction to this chapter, that the introduction of a magnetic length scale into the system requires the definition of large systems in order to avoid finite-size effects. The magnitude of finite-size effects is clearly magnetic field dependent and it is of great importance to check the previous calculation for convergence with respect to system size. The LSW regions of the slab calculation are larger than the Hallbar system and a finite-size discussion of all Hallbar systems with LSW is sufficient. I will discuss three system sizes for TBLG with and without coupling, SLSW and TLSW each. Every system calculation has a different disorder configuration, but the results discussed in this section are largely disorder independent (not shown).

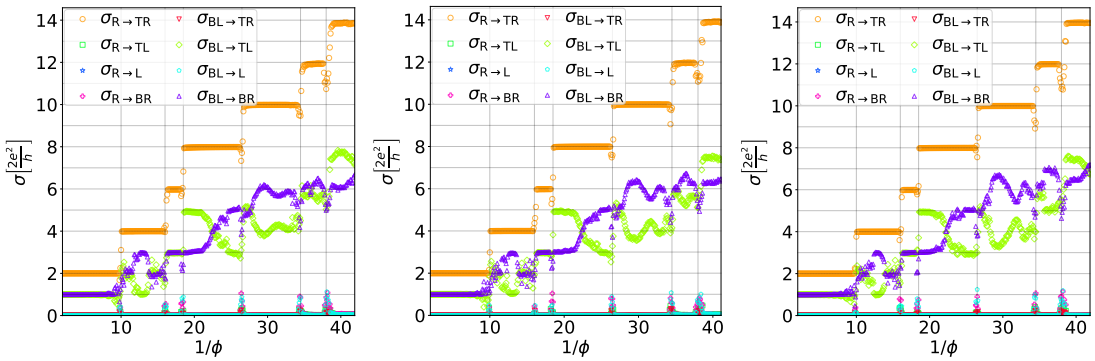

(a) $N \approx 1.6 \times 10^5$ (b) $N \approx 2.0 \times 10^5$ (c) $N \approx 2.7 \times 10^5$

Figure 9.15: HLSW Hallbar system finite-size analysis for transmission diagrams, see Figure 9.5 for a description of transmission diagrams. The lower layer is fully coupled $t^{(1)}_{\mathrm{LSW}} = t$. The upper layer is decoupled $t^{(2)}_{\mathrm{LSW}} = 0$.

A finite-size study for HLSW systems with decoupled upper layer is shown in Figure 9.15. Comparing 9.15a, 9.15b and 9.15c, it is clear that there are some finite-size effects in the calculation of smaller systems. Particularly in the transmissions $\sigma_{\mathrm{BL}\to\mathrm{BR}}$ and $\sigma_{\mathrm{BL}\to\mathrm{TL}}$ in the regime of smaller magnetic field (the last three plateaus), features are still changing with system size. Increases and decreases in the conductivity are sharper for higher system sizes in this region. For smaller plateaus however, the system has already converged to a satisfactory degree for the smallest system size. The general shape of the conductivities does also not change with system size.

A finite-size study for HLSW systems with fully coupled upper layer is shown in Figure 9.16. Increasing the coupling between left and right sheet should not affect finite-size effects and this is reflected by comparing Figure 9.16 to Figure 9.15. The finite-size analysis for systems with coupling is essentially the same. The conductance for earlier plateaus is already converged for small system sizes and the features for later plateaus become sharper with increased system size.

A finite-size study for SLSW systems is shown in Figure 9.17. The conductance functions for all three system sizes are almost identical, particularly for the first four plateaus. After that some features show minor change change with system size at plateau transitions. The increases and decreases due to plateau transition become more localized with larger system size.

A finite-size study for TLSW systems is shown in Figure 9.18. Due to the strong fluctuations of $\sigma_{\mathrm{BL}\to\mathrm{TL}}$ and $\sigma_{\mathrm{BL}\to\mathrm{BR}}$ in TLSW systems, discussing finite-size effects is more difficult than for HLSW and SLSW systems. Like for the other system types, the conductance across the first

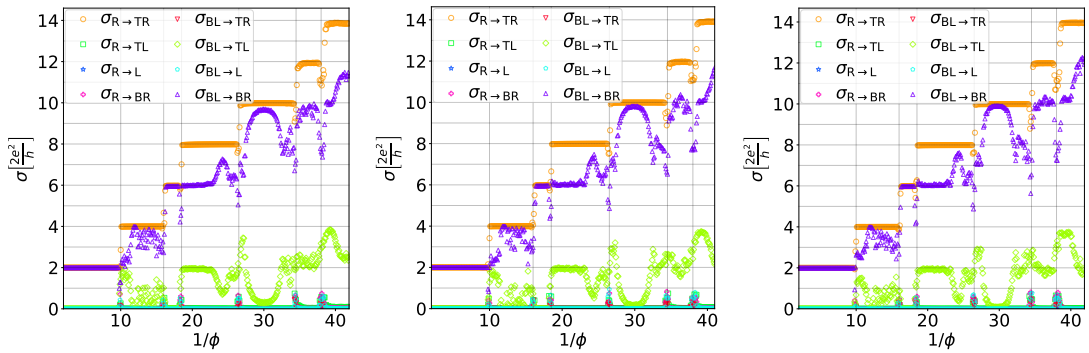

(a) $N \approx 1.6 \times 10^5$ (b) $N \approx 2.0 \times 10^5$ (c) $N \approx 2.7 \times 10^5$

Figure 9.16: HLSW Hallbar system finite-size analysis for transmission diagrams, see Figure 9.5 for a description of transmission diagrams. The lower layer is fully coupled $t^{(1)}_{\mathrm{LSW}} = t$. The upper layer is fully coupled $t^{(2)}_{\mathrm{LSW}} = t$.

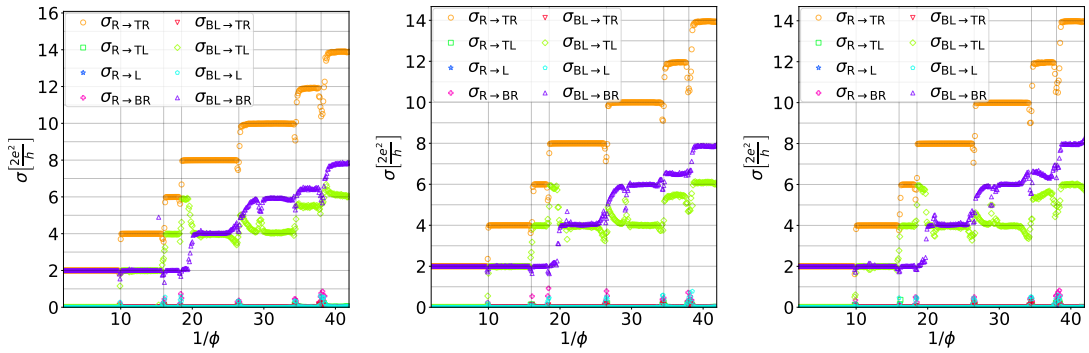

(a) $N \approx 1.4 \times 10^5$ (b) $N \approx 1.8 \times 10^5$ (c) $N \approx 2.3 \times 10^5$

Figure 9.17: SLSW Hallbar system finite-size analysis for transmission diagrams, see Figure 9.5 for a description of transmission diagrams. The cutoff between the two layers in the LSW is long, $D_c = 4a_{cc}$. The shear width parameter is $L_S = 44$

four plateaus is similar for all system sizes. But even for large external magnetic fields, there are differences between 9.18b and 9.18c close to plateau transitions. In particular the shape of $\sigma_{\mathrm{BL}\to\mathrm{TL}}$ and $\sigma_{\mathrm{BL}\to\mathrm{BR}}$ differs near the third plateau. These changes however are fairly small in magnitude and given the satisfactory convergence of all other system types for these system sizes, using either the system size in 9.18b or the one in 9.18c should be fine in the parameter range under consideration. The existence of finite-size effects for these systems however cannot be ruled out as confidently as for the other system types and finite-size effects should be kept in mind when discussing TLSW systems in other sections.

Generically, systems in the regime of 1×10^5 to 2×10^5 sites are sufficient to discuss the first four plateaus of the magnetoconductance and systems of the order 2×10^5 to 3×10^5 are required to discuss the full range of magnetic field shown in previous calculations. Even for larger plateaus, smaller system sizes should be sufficient to determine generic features of the conductivity shapes, but finite-size effects must be considered if such calculations are discussed.

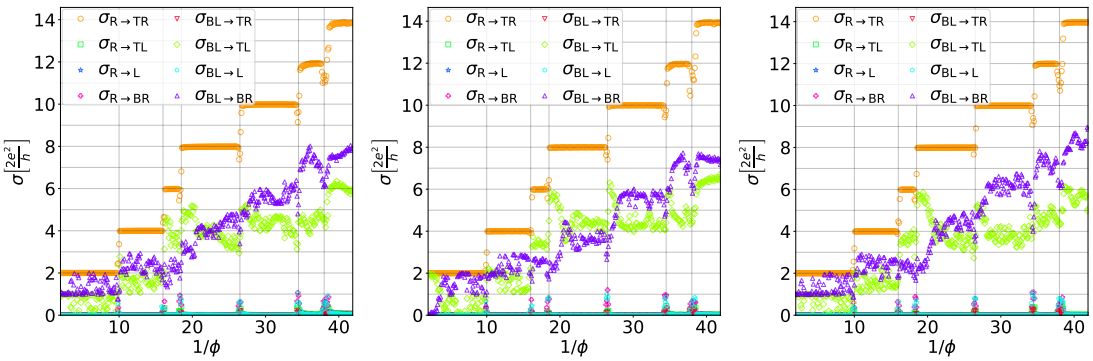

(a) $N \approx 1.6 \times 10^5$ (b) $N \approx 2.0 \times 10^5$ (c) $N \approx 3.0 \times 10^5$

Figure 9.18: TLSW Hallbar system finite-size analysis for transmission diagrams, see Figure 9.5 for a description of transmission diagrams. The cutoff between the two layers in the LSW is long, $D_c = 4a_{cc}$. The tension length parameter is $L_T = 60$.

9.7 Discussion of interaction cutoff effects

Another important parameter of the simulation is the cutoff distance D_c. For regular BLG and HLSW systems I chose D_c, such that only nearest neighbour hopping terms are nonzero. This should be adequate to discuss the IQHE. For TBLG systems and systems with shear and tension however such an early cutoff might not model the physics properly. Thus convergence with respect to D_c should be checked for SLSW and TLSW systems.

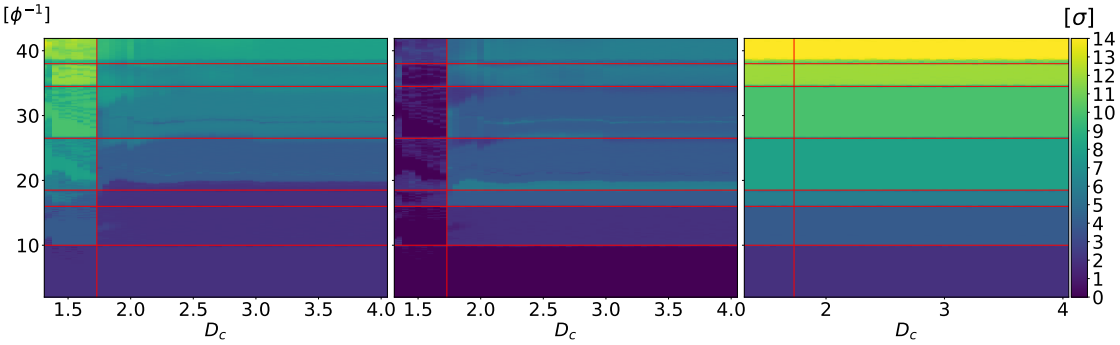

Figure 9.19: Parameter study of the cutoff distance D_c for different external magnetic fields ϕ^{-1} for a SLSW system. The three plots show the conductance in color with the cutoff distance D_c on the y-axis and the magnetic field on the x-axis. On the left is $\sigma_{\mathrm{BL}\to\mathrm{BR}}$, in the middle is $\sigma_{\mathrm{BL}\to\mathrm{TL}}$ and on the right is $\sigma_{\mathrm{R}\to\mathrm{TR}}$. The number of sites in the system used for the transmission calculations is $N_T \approx 2.3 \times 10^5$. The shear width parameter is $L_S = 44$.

In Figure 9.19 a calculation of different cutoff distances for SLSW systems is shown. The magnetoconductance shows a large jump at the value $D_c \approx 1.73$ (position of red line). In the interval $D_c \in [0, 1.73]$, the contribution to $\sigma_{\mathrm{BL}\to\mathrm{BR}}$ in the right plot is much larger and the contribution to $\sigma_{\mathrm{BL}\to\mathrm{TL}}$ much smaller than to the right of the jump. The dependence on the cutoff distance to the right of the jump is strong and there is no obvious plateau structure for $\sigma_{\mathrm{BL}\to\mathrm{BR}}$ in this regime. To the right of the jump, in the interval $D_c \in [1.73, 4.0]$, the magnetoconductance

changes less rapidly with D_c and there is a more apparent plateau structure when near the plateau centers of $\sigma_{\mathrm{R}\to\mathrm{TR}}$. The magnetoconductance functions show good convergence for values of $D_c > 3.0$. The reference parameter study of $\sigma_{\mathrm{R}\to\mathrm{TR}}$ is independent of D_c, as it should be. Ultimately the structure of the calculation in Figure 9.10 is well converged and a choice of $D_c = 4.0$ is adequate for all further studies.

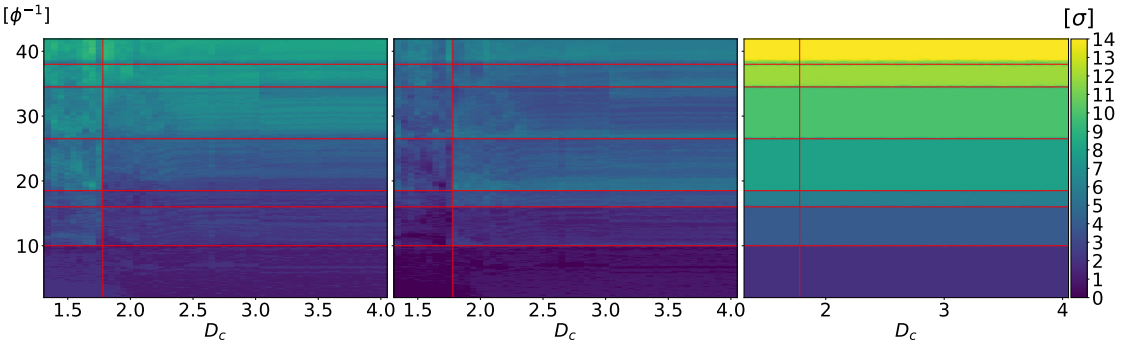

Figure 9.20: Parameter study of the cutoff distance D_c for different external magnetic fields ϕ^{-1} for a SLSW system. The three plots show the conductance in color with the cutoff distance D_c on the y-axis and the magnetic field on the x-axis. On the left is $\sigma_{\mathrm{BL}\to\mathrm{BR}}$, in the middle is $\sigma_{\mathrm{BL}\to\mathrm{TL}}$ and on the right is $\sigma_{\mathrm{R}\to\mathrm{TR}}$. The number of sites in the system used for the transmission calculations is $N_T \approx 2.0 \times 10^5$. The tension length parameter is $L_T = 60$.

In Figure 9.20 a calculation of different cutoff distances for TLSW systems is shown. Just as for all calculations, the magnetoconductance for this system types shows much stronger fluctuations than for the SLSW systems. Similarly to the SLSW case, there is a strong jump in the transmission function for a particular value of the cutoff distance. For the TLSW system this value is $D_c \approx 1.78$ (position of red line). The change in transmission however is not as pronounced as in the SLSW case and the plateaus one to four are most affected, whereas the larger plateaus do not exhibit such a jump. There is a strong dependency on D_c in both $\sigma_{\mathrm{BL}\to\mathrm{BR}}$ and $\sigma_{\mathrm{BL}\to\mathrm{TL}}$ below $D_c \approx 2.3$. After that, there is another minor change in conductance at $D_c = 3.0$, where the decrease due to the fourth plateau transition in $\sigma_{\mathrm{R}\to\mathrm{TR}}$ becomes larger. After $D_c = 3.0$ however, the magnetoconductance is well converged keeping in mind the usual conductance fluctuations. As such the calculation for $D_c = 4.0$ in Figure 9.13 and all other studies of the system presented in this thesis should be appropriately converged with respect to the numerical hopping integral cutoff D_c.

The strong changes in the structure of the magnetoconductance calculations at particular values of D_c make sense, since they correspond to the inclusion of particular hopping elements in the BLG lattice. In the case of the $D_c \approx 1.7$ jump hoppings between sites of the same sublattice are added respectively.

9.8 Systems at other Fermi energies

As mentioned in the discussion of the parameters for all previous calculations, the Fermi energy of all systems under consideration was $0.95\,\mathrm{eV} \approx 0.35t$. To identify energy dependencies a small study of the Fermi energy as system parameter is performed for HLSW with fully coupled upper sheet, SLSW and TLSW systems. A small Fermi energy is difficult to investigate, since it requires smaller magnetic fields and thus larger length scales to suppress finite-size effects. Thus a large

parameter study of very low-energy properties with a discrete model is currently not feasible due to computing time constraints.

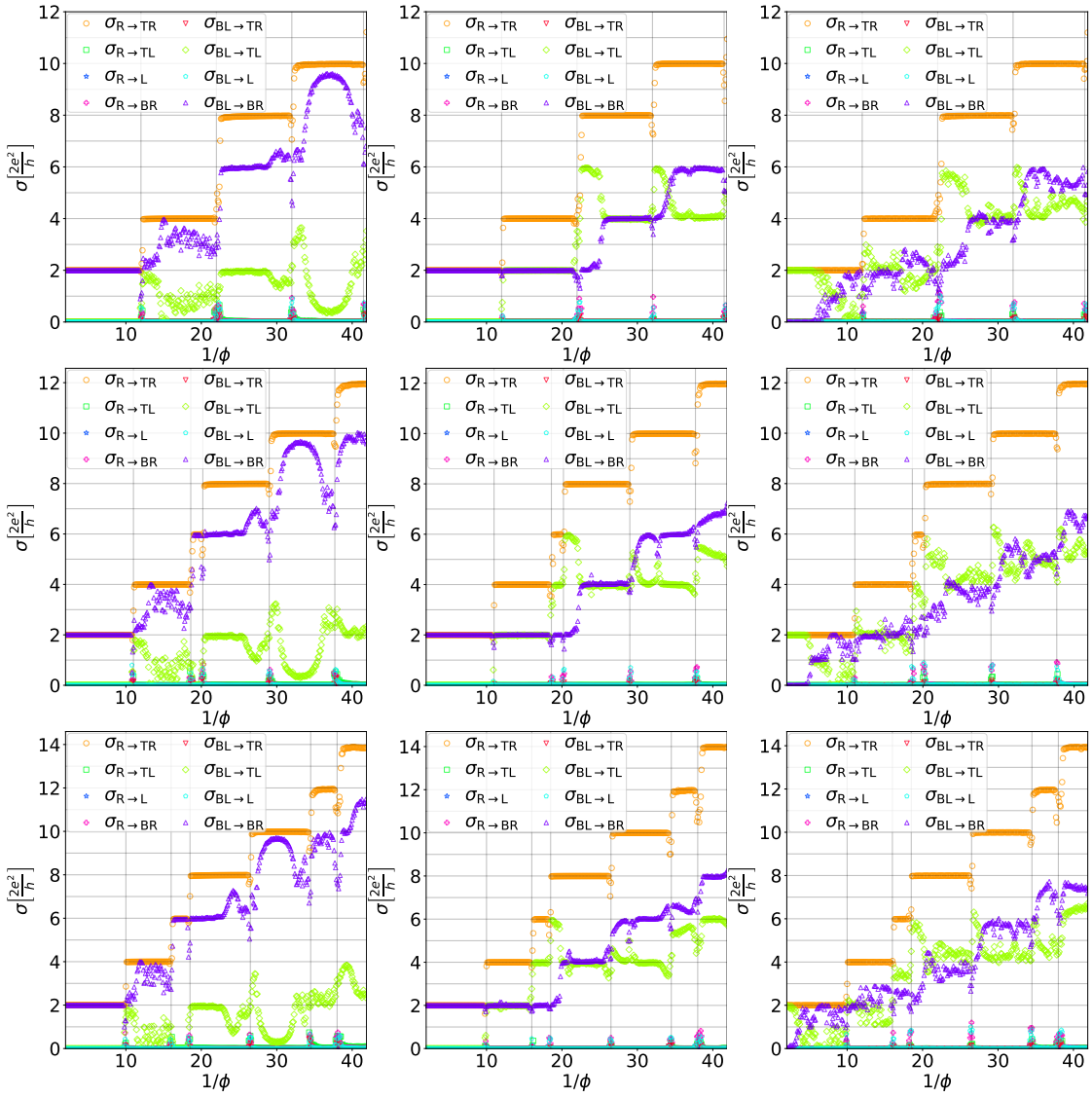

Figure 9.21: Fermi energy study. Transmission for HLSW $N \approx 1.6 \times 10^5$ (left), SLSW $N \approx 1.7 \times 10^5$ (middle), TLSW $N \approx 1.8 \times 10^5$ (right) systems. The energies are $E_F = 0.85\,\mathrm{eV}$ (top), $E_F = 0.9\,\mathrm{eV}$ (middle), $E_F = 0.95\,\mathrm{eV}$ (bottom).

The Fermi energy study is shown in Figure 9.21. The first obvious observation for all three system configurations is the difference in the Landau level filling for different Fermi energies. At lower energies and the same magnetic field, fewer bands will be filled and thus an analysis of the same region of magnetic field values at smaller Fermi energies will show a smaller number of plateaus. This is the essential reason why a large Fermi energy was used to perform calculations. To observe larger fillings for smaller energies, one would require smaller magnetic fields and thus

larger systems to avoid finite-size effects.

There are changes to the plateau structure of $\sigma_{\mathrm{R}\to\mathrm{TR}}$ at different energies, but that is to be expected, since a different underlying band structure at a particular Fermi energy without magnetic field leads to different plateau transition positions. In particular, the width of the third plateau in $\sigma_{\mathrm{R}\to\mathrm{TR}}$ decreases for smaller Fermi energies.

For all three system configurations under consideration the general shapes of $\sigma_{\mathrm{BL}\to\mathrm{BR}}$ and $\sigma_{\mathrm{BL}\to\mathrm{TL}}$ are remarkably similar for different energies supporting the generality of the discussed results. Although the generic shapes of $\sigma_{\mathrm{BL}\to\mathrm{BR}}$ and $\sigma_{\mathrm{BL}\to\mathrm{TL}}$ are energy independent, there are also features, that warrant closer inspection.

For the HLSW systems on the left, the conductivities under consideration are largely the same except for two particular structures. The increase of $\sigma_{\mathrm{BL}\to\mathrm{BR}}$ and decrease of $\sigma_{\mathrm{BL}\to\mathrm{TL}}$ at the transition from fourth to fifth plateau are attenuated for smaller energies. The transition from a smaller peak in $\sigma_{\mathrm{BL}\to\mathrm{BR}}$ to a larger one from $E_F = 0.85\,\mathrm{eV}$ to $E_F = 0.9\,\mathrm{eV}$ and finally to $E_F = 0.95\,\mathrm{eV}$ is apparent. There is also a decrease in $\sigma_{\mathrm{BL}\to\mathrm{TL}}$ at the transition from second to third plateau for $E_F = 0.95\,\mathrm{eV}$, whose width decreases for $E_F = 0.9\,\mathrm{eV}$ and has entirely vanished for $E_F = 0.85\,\mathrm{eV}$

For the SLSW systems, the plateau structure is preserved in the range of interest. The conductance $\sigma_{\mathrm{BL}\to\mathrm{BR}}$ is shifted to larger ϕ^{-1} for smaller Fermi energies. This causes structure in the conductance $\sigma_{\mathrm{BL}\to\mathrm{TL}}$, namely peaks around $\phi^{-1} = 22$ and $\phi^{-1} = 32$, due to the offset between plateau transitions in $\sigma_{\mathrm{R}\to\mathrm{TR}}$ and $\sigma_{\mathrm{BL}\to\mathrm{BR}}$. The two conductances for the Fermi energy $E_F = 0.95\,\mathrm{eV}$ merely seem to be well aligned such that $\sigma_{\mathrm{BL}\to\mathrm{TL}}$ has a plateau structure as well. Thus the plateau structure in $\sigma_{\mathrm{BL}\to\mathrm{BR}}$ is generic for energies in the considered range, but the plateau structure of $\sigma_{\mathrm{BL}\to\mathrm{TL}}$ is not. The width change of the third plateau is also reflected in the width of the peak in $\sigma_{\mathrm{BL}\to\mathrm{TL}}$ near that transition.

Just as for the previous two system types, the general shape of the conductance calculations is similar for all three energies considered aside from the change in filling due to changed electron density at any particular value of ϕ^{-1}. Like for the HLSW calculations the change in width of the third plateau causes changes in the conductances $\sigma_{\mathrm{BL}\to\mathrm{TL}}$ and $\sigma_{\mathrm{BL}\to\mathrm{BR}}$. Aside from that the general shape of the conductances is energy independent, but the particular fluctuations do change with energy. For example, the exact structures of $\sigma_{\mathrm{BL}\to\mathrm{TL}}$ and $\sigma_{\mathrm{BL}\to\mathrm{BR}}$ around the fifth plateau clearly show a small energy dependence. However, the instability of this system type with respect to parameter changes has already been established and this behaviour is not surprising.

For all three system types, changes of features in the region between $\phi^{-1} = 15$ and $\phi^{-1} = 23$ for $E_F = 0.95\,\mathrm{eV}$ coincide with the decrease in the width of the third plateau for smaller Fermi energies. It seems reasonable, that the magnetoconductivity for LSW systems would reflect the changes in the homogeneous systems.

In conclusion, there are changes in the conductivities with Fermi energy. This behaviour however is not unexpected, since the homogeneous system conductance also changes with energy. These changes however do not fundamentally change the previous discussions of these systems and this is a good indicator that the discussed properties like plateau formation are generic, at least in the energy range investigated.

9.9 Parameter study of the hard wall coupling strength

The most physically relevant factor in the HLSW system is the coupling strength between regions. Thus I performed a parameter study of the coupling strength $t^{(2)}_{\mathrm{LSW}}$ for these systems. Up until now, only $t^{(2)}_{\mathrm{LSW}} = 0$ and $t^{(2)}_{\mathrm{LSW}} = t$ as limiting cases haven been considered and they yielded significantly different results. Thus a strong dependence of the conductance on $t^{(2)}_{\mathrm{LSW}}$ is expected.

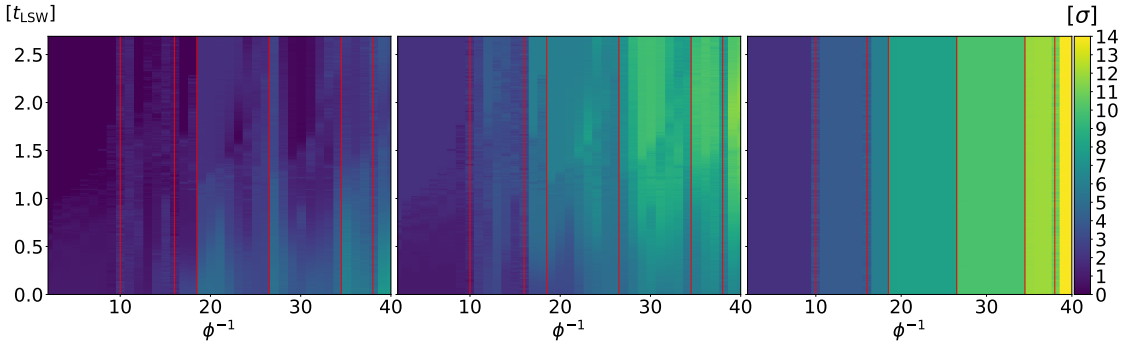

Figure 9.22: Parameter study of the HLSW interaction strength $t^{(2)}_{\mathrm{LSW}}$ for different external magnetic fields ϕ^{-1} for a HLSW system. The three plots show the conductance in color with the HLSW interaction strength $t^{(2)}_{\mathrm{LSW}}$ on the y-axis and the magnetic field on the x-axis. On the left is $\sigma_{\mathrm{BL}\to\mathrm{BR}}$, in the middle is $\sigma_{\mathrm{BL}\to\mathrm{TL}}$ and on the right is $\sigma_{\mathrm{R}\to\mathrm{TR}}$. The number of sites in the system used for the transmission calculations is $N_T \approx 1.6 \times 10^5$.

The dependence of the conductance on $t^{(2)}_{\mathrm{LSW}}$ for various external magnetic fields is shown in Figure 9.22. Only $\sigma_{\mathrm{R}\to\mathrm{TR}}$, $\sigma_{\mathrm{BL}\to\mathrm{BR}}$ and $\sigma_{\mathrm{BL}\to\mathrm{TL}}$ are shown, since they are the only relevant elements of the conductance tensor when not at a transition between plateaus. The behaviour of the other conductivities at the plateau transition is not of interest, since they strongly depend on the particular geometry and disorder configuration of the system. On the right of Figure 9.22 is a calculation of $\sigma_{\mathrm{R}\to\mathrm{TR}}$, which is independent of the coupling strength between upper layers. This quantity serves as a reference to the plateau structure in a homogeneous system where plateau transitions are indicated by red stripes.

In the middle plot in Figure 9.22, $\sigma_{\mathrm{BL}\to\mathrm{BR}}$ is shown. It does not seem as if the limiting cases $t^{(2)}_{\mathrm{LSW}} = 0$ and $t^{(2)}_{\mathrm{LSW}} = t$ have special properties, that differentiate them from the other values of $t^{(2)}_{\mathrm{LSW}}$. Generically, $t^{(2)}_{\mathrm{LSW}}$ is larger for larger $t^{(2)}_{\mathrm{LSW}}$, but the increase is not monotonous for all external magnetic field values. Notably, $\sigma_{\mathrm{BL}\to\mathrm{BR}} = \sigma_0$ for values around $t^{(2)}_{\mathrm{LSW}} = 0$ and $\sigma_{\mathrm{BL}\to\mathrm{BR}} = 2\sigma_0$ for values around $t^{(2)}_{\mathrm{LSW}} = t$ for the first plateau confirming the results from the magnetoconductance discussion of the limiting cases. Since there was no obvious plateau structure for any of the limiting cases, this calculation confirms that there is no plateau structure for any value of $t^{(2)}_{\mathrm{LSW}} \in [0, t]$. The tendency of a larger magnitude in $\sigma_{\mathrm{BL}\to\mathrm{BR}}$ close to the centers of plateaus also persists for all $t^{(2)}_{\mathrm{LSW}}$ under consideration.

On the left of Figure 9.22 is the calculation of $\sigma_{\mathrm{BL}\to\mathrm{TL}}$, which is redundant since $\sigma_{\mathrm{BL}\to\mathrm{BR}} + \sigma_{\mathrm{BL}\to\mathrm{TL}} = \sigma_{\mathrm{R}\to\mathrm{TR}}$. The features of $\sigma_{\mathrm{BL}\to\mathrm{TL}}$ are thus simply an inversion the the features of $\sigma_{\mathrm{BL}\to\mathrm{BR}}$, being larger closer to plateau transitions, decreasing for larger $t^{(2)}_{\mathrm{LSW}}$ and showing no obvious plateau structure.

9.10 Parameter study of the shear layer switching wall width

For SLSW and TLSW systems, the parameter of greatest physical interest is the extent of the LSW region.

Thus an extensive parameter study of L_s for different magnetic fields is shown in Figure 9.23.

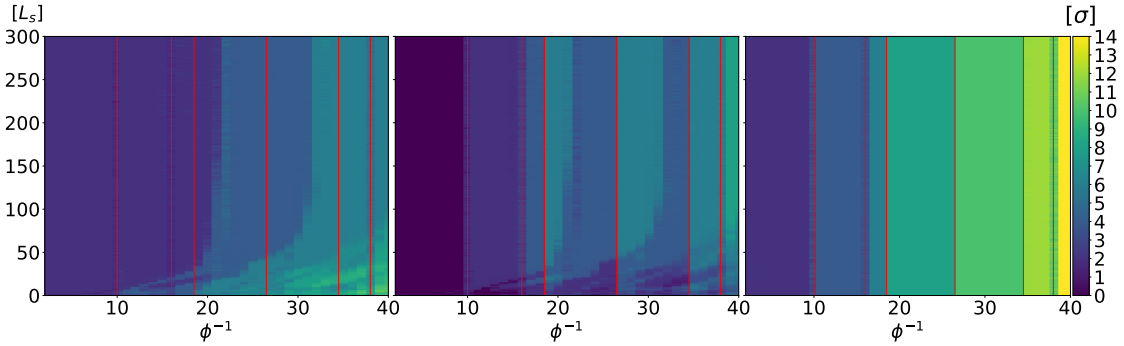

Figure 9.23: Parameter study of the SLSW width L_s for different external magnetic fields ϕ^{-1} for a SLSW system. The three plots show the conductance in color with the SLSW width L_s on the y-axis and the magnetic field on the x-axis. On the left is $\sigma_{\mathrm{BL}\to\mathrm{BR}}$, in the middle is $\sigma_{\mathrm{BL}\to\mathrm{TL}}$ and on the right is $\sigma_{\mathrm{R}\to\mathrm{TR}}$. The number of sites in the system used for the transmission calculations is $N_T \approx 2.3 \times 10^5$. The cutoff between the two layers in the LSW is long, $D_c = 4a_{cc}$.

On the right is the calculation of $\sigma_{\mathrm{R}\to\mathrm{TR}}$ for different shear widths. As one would expect, the calculation reveals a plateau structure, that is independent of the shear width, since, the contribution from R to TR is spatially far away from the SLSW. There are some fluctuations in the conductance for values of the external magnetic field ϕ^{-1} where plateau transitions occur, but this is also expected since states actually delocalize and the particular structure of the SLSW can influence the propagation.

On the left in Figure 9.23 is the equivalent calculation for $\sigma_{\mathrm{BL}\to\mathrm{BR}}$. As expected the conductance varies strongly with L_s. The features due to plateau transitions are also visible here and look similar to the ones in $\sigma_{\mathrm{R}\to\mathrm{TR}}$. The hypothesis of convergence for large L_s is also confirmed by these calculations. At a value of approximately $L_s = 100$ there are no longer any major changes near the center of plateaus. This calculation also confirms that the convergence depends on the external magnetic field, converging earlier for a stronger external magnetic field and later for a weaker external magnetic field. These convergence features are not clear enough to definitively classify them as parabolic, as they should be if they are proportional to the magnetic length, or some other functional dependence. The non-converged values in the small shear width limit are generically smaller than the values in the large shear width limit. This is sensible, if the SLSW were to be modeled by some potential wall that is thicker for a wider SLSW.

In the middle in Figure 9.23 is the study of $\sigma_{\mathrm{BL}\to\mathrm{TL}}$. This is of course redundant, since for all values of ϕ^{-1} except plateau transitions, $\sigma_{\mathrm{BL}\to\mathrm{TL}} + \sigma_{\mathrm{BL}\to\mathrm{BR}} = \sigma_{\mathrm{R}\to\mathrm{TR}}$. This calculation confirms, that the large shear width limit of $\sigma_{\mathrm{BL}\to\mathrm{TL}}$ is not a monotonous plateau structure. However, since the limits of $\sigma_{\mathrm{BL}\to\mathrm{TL}}$ and $\sigma_{\mathrm{R}\to\mathrm{TR}}$ both have plateau structure, so does $\sigma_{\mathrm{BL}\to\mathrm{TL}}$, just not a monotonous one.

9.11 Parameter study of the tension layer switching wall width

Similar to the shear width parameter analysis, this section contains a tension width parameter discussion. In particular differences and similarities between the two system types are of interest.

The parameter study of L_t is shown in Figure 9.24. The calculation on the right for $\sigma_{\mathrm{R}\to\mathrm{TR}}$ is equivalent to the one in Figure 9.23 and the discussion is also the same. The results for $\sigma_{\mathrm{BL}\to\mathrm{BR}}$

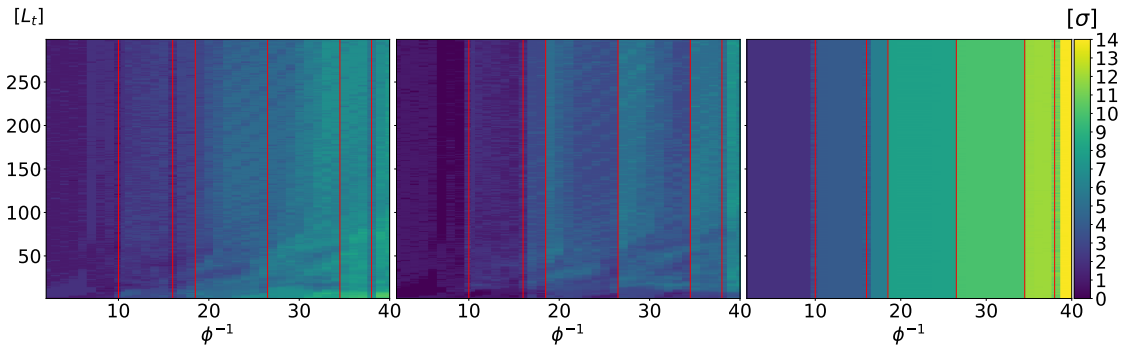

Figure 9.24: Parameter study of the TLSW width L_t for different external magnetic fields ϕ^{-1} for a TLSW system. The three plots show the conductance in color with the TLSW width L_t on the y-axis and the magnetic field on the x-axis. On the left is $\sigma_{\mathrm{BL}\to\mathrm{BR}}$, in the middle is $\sigma_{\mathrm{BL}\to\mathrm{TL}}$ and on the right is $\sigma_{\mathrm{R}\to\mathrm{TR}}$. The number of sites in the system used for the transmission calculations is $N_T \approx 2.0 \times 10^5$. The cutoff between the two layers in the LSW is long, $D_c = 4a_{cc}$.

and $\sigma_{\mathrm{BL}\to\mathrm{TL}}$ however differ from the SLSW results significantly, as the previous discussions already suggested. The fluctuations that were visible in the magnetoconductance calculations are also present in the left and middle images shown in Figure 9.24.

The left image in Figure 9.24 shows $\sigma_{\mathrm{BL}\to\mathrm{BR}}$. The conductance has the value σ_0 for large values of L_t, but the value $2\sigma_0$ for the small L_t limit on the first plateau. Just as for the SLSW system, $\sigma_{\mathrm{BL}\to\mathrm{BR}}$ is generically larger for larger L_t with the same physical interpretation. The TLSW system also has the magnetic-length dependent convergence structure, similar to what was described for the SLSW systems. The stripes due to plateau transitions in $\sigma_{\mathrm{R}\to\mathrm{TR}}$ are also visible. There is however no obvious limit for large L_t, since there are persistent fluctuations in $\sigma_{\mathrm{BL}\to\mathrm{BR}}$, even for large L_t. Within the range of these fluctuations, which are of the order σ_0, $\sigma_{\mathrm{BL}\to\mathrm{BR}}$ assumes a plateau structure for large L_t.

The conclusions for $\sigma_{\mathrm{BL}\to\mathrm{TL}}$ in the middle of Figure 9.24 are essentially the same as for the SLSW system, considering the fluctuations which seem natural to the system type. There is a non-monotonous plateau structure within the range of the fluctuations mentioned for large L_t.

Chapter 10

Summary and Outlook

10.1 Summary

I will begin the summary of this thesis with a short physical motivation of the discussed topics. Recently, interest in BLG systems has increased rapidly for various reasons. One is the existence of anomalous superconductivity at magic twist angles. Another is the natural formation of topologically conducting channels in epitaxially grown BLG. The latter is what motivated this thesis. An external electric field induces interesting properties in BLG systems with LSW and there exists an anomalous IQHE for BLG. This naturally lead to the question, how BLG systems with LSWs would behave when subjected to an external magnetic field. That is the fundamental question of this thesis.

To answer this question, various computational tools were developed. One method to identify different properties of systems in the IQHE regime is the calculation of transport properties, see chapter 2, which is possible for very large system sizes. Various numerical methods, all roughly based on the recursive Green's function method, were implemented in chapter 3. Another method for system classification is the calculation of topological invariants for the relevant systems. Two methods were implemented, the Wannier charge center method and the Bott index method, in order to calculate the Chern number for systems in the IQHE regime. Refer to chapter 4 for the theoretical background and chapter 5 for the implementation details. All methods were first tested on a simple trial system with analytical solution but nontrivial topology, the Haldane model.

The invariant calculations were successful for the trial case of the Haldane model defined in chapter 6. I performed Wannier charge center and Bott index invariant calculations for a Haldane model with multiple unit cells in section 6.2. Both methods produced the usual Haldane phase diagram. The Bott index calculation required a larger system size to converge than the Wannier charge center method, which only required the definition of a single unit cell. For equal system sizes, the Bott index method however proved to be much faster. The second system type investigated was a Haldane system with a domain wall between magnetic flux regions. Transport calculations for both system types produced the anticipated number of edge modes with some expected numerical instability in the small energy gap regime.

The invariant calculations for the BLG systems were not successful. This is due to the large system size, that is required for the suppression of finite size effects. Both invariant calculation techniques require dense matrix operations with matrices of the order of the size of the system. These operations are not feasible on current computers and I am not aware of any purely sparse methods at half filling. Thus it is currently not possible to perform the calculation of topological

invariants on the BLG systems presented in this thesis.

The main results of thesis are the LDOS and transmission calculations for various BLG systems including studies of physically relevant parameters in chapter 9. Both of these calculations were performed for two transport experiment setups. The first transport experiment is the calculation for a simple rectangular two-terminal setup I called a *Slab*. The second transport experiment was a six terminal setup, which is illustrated in Figure 9.3, that I called a *Hallbar*. Both of these correspond to different real experiments, but the *Hallbar* geometry is optimal to analyze BLG systems with LSW in the IQHE regime.

Three BLG systems were introduced to model LSWs in epitaxial BLG. The first was a simple hard wall transition between AB and BA stacking along the zigzag nanoribbon. The second is a smooth transition due to shear in the upper layer leading to an LSW along the armchair nanoribbon. The third system is a smooth LSW due to tension implying a transition along the zigzag nanoribbon.

First, a homogeneous BLG system was considered and magnetoconductance calculations and LDOS calculations for both setups were performed in section 9.2. The results showed, as expected, an anomalous IQHE and localized edge modes.

After confirming the appropriate results for the homogeneous model, the simplest mode was investigated first, the hard wall model. Calculations for fully coupled and decoupled upper layer were performed in section 9.3 (for explanation of terminology, refer to BLG system description). The LDOS calculation showed increased density at the material edge and in the region of the LSW due to conductance parallel to the LSW. The decoupled case showed generally smaller conductance $\sigma_{\mathrm{BL}\to\mathrm{BR}}$ (contributions to the conductance through the LSW) than the coupled case. There was no obvious plateau formation in any of the elements of the conductance tensor. Generally $\sigma_{\mathrm{BL}\to\mathrm{BR}}$ was larger in the center of a plateau and smaller to the edge of one. The explanation of this was deduced to be the same argument as for the increased cross conductance at transitions between plateaus. Availability of states, that are delocalized, increases close to plateau transitions.

The next system discussed was the one, where the LSW was due to a shear in the upper graphene layer in section 9.4. Just as in case of the hard wall model, there was increased density in the LSW region leading to conductance parallel to the LSW. The conductance element $\sigma_{\mathrm{BL}\to\mathrm{BR}}$ however exhibits plateau-like structure in the limit of very large LSW regions. The exact nature of this plateau formation however is unclear.

The last system type investigated was the BLG model with an LSW due to tension in section 9.5. As for the previous two cases, there is an increase in density in the LSW region and a contribution to $\sigma_{\mathrm{BL}\to\mathrm{BR}}$. The conductance was generally much more chaotic than in the previous two cases. There is generic plateau formation for large LSW regions just like for the shear LSW system, but even for very large LSWs, there were still fluctuations of the order of σ_0.

After the discussion of all three system types I made sure, none of the discussed features was a finite-size effect. For this purpose magnetoconductance calculations were performed for all system types and for three different system sizes in section 9.6. The magnetoconductance did still have some minor changes in the size regime investigated, but the generic shape of the magnetoconductance plots had already converged for the smallest system size. I concluded, that the system sizes chosen for the parameter studies in the other sections were adequate.

Another important numerical system parameter is the cutoff distance for the modeled hopping integral in the LSW region. In the region of Bernal stacked BLG a nearest neighbour model is adequate to discuss the IQHE, but in the case of sheared or tensed BLG this was not obvious ab into. Thus I conducted a parameter study of the cutoff radius for hopping integrals for sheared and tensed systems in section 9.7. For both sheared and tensed systems, there was a cutoff distance at which a sudden change in the magnetoconductance occurred, around $1.7a_{cc}$ (where a_{cc}

is the carbon-carbon distance in graphene). After this sudden change there were still changes in the magnetoconductance with the cutoff distance, but the convergence after the jump was smooth. For both system types, the conductance was approximately converged after $3.0a_{cc}$, justifying the choice of $4.0a_{cc}$ for all other calculations.

All calculations up to this point were performed at the Fermi energy $E_F = 0.95\,\mathrm{eV}$. This choice was due to the stronger finite size effects for choices of smaller Fermi energy. For the same reason, the study of the Fermi energy dependence was performed in a limited energy range in section 9.8. For all system types, magnetoconductance computations at $E_F = 0.85\,\mathrm{eV}$, $E_F = 0.9\,\mathrm{eV}$ and $E_F = 0.95\,\mathrm{eV}$ were compared. Aside from the change in filling of Landau levels due to a different Fermi energy, the homogeneous system also showed a modification of the IQHE plateau structure with energy: A shrinking in width of the third plateau. This change also manifested in the conductances across and parallel to the LSW. Aside from these changes there were minor changes in magnetoconductance with energy, but the general features like plateau formation remained invariant under change of Fermi energy.

After the discussion for hard wall, sheared and tensed system the physically most relevant parameter of each of these systems was investigated in more detail. For the hard wall system this is the coupling strength in section 9.9, for the sheared system and the tensed system it is the extent of the respective LSW in section 9.10 and section 9.11. The results of this section essentially reinforced the ones deduced in the previous sections. The sheared and tensed system both converge for very large LSW widths. Both exhibit plateau formation in this regime. The plateau formation in the shear system case is not as chaotic as the tensile system case, where the fluctuations of order σ_0 are persistent even in the large LSW limit. There is no obvious plateau formation for the HLSW case and the simple hard wall model does not seem to model either the sheared or the tensed model particularly well.

10.2 Outlook

As of now, there is no apparent method of extending the invariant calculations to bilayer graphene systems with external magnetic field.

The investigation of the systems proposed is by no means exhaustive. What follows is a list of possible examinations, that might yield interesting results, also highlighting the limitations of this research:

- More than one LSW in a system should be thoroughly investigated.
- Modelling entire defect networks is most likely not feasible due to the required system size being far larger than that of a single defect, which is already quite large.
- Calculations for even larger systems to examine higher Landau levels.
- Interaction between electrons [64] [65] [66] and an eventual investigation of the fractional quantum Hall regime would be of interest. These discussions, however are not feasible for large system sizes.
- Calculations for a hard wall model along the armchair nanoribbon and a comparison to the SLSW system.
- Calculations for an LSW due to a change in numerical interaction cutoff for an otherwise homogeneous system.

Bibliography

[1] M. Z. Hasan and C. L. Kane. Colloquium: Topological insulators. *Rev. Mod. Phys.*, 82:3045–3067, Nov 2010.

[2] Xiao-Liang Qi and Shou-Cheng Zhang. Topological insulators and superconductors. *Rev. Mod. Phys.*, 83:1057–1110, Oct 2011.

[3] A. H. Castro Neto, F. Guinea, N. M. R. Peres, K. S. Novoselov, and A. K. Geim. The electronic properties of graphene. *Rev. Mod. Phys.*, 81:109–162, Jan 2009.

[4] Charles L Kane and Eugene J Mele. Quantum spin hall effect in graphene. *Physical review letters*, 95(22):226801, 2005.

[5] Edward McCann and Mikito Koshino. The electronic properties of bilayer graphene. *Reports on Progress in Physics*, 76(5):056503, apr 2013.

[6] Taisuke Ohta, Aaron Bostwick, Thomas Seyller, Karsten Horn, and Eli Rotenberg. Controlling the electronic structure of bilayer graphene. *Science*, 313(5789):951–954, 2006.

[7] E. Suárez Morell, J. D. Correa, P. Vargas, M. Pacheco, and Z. Barticevic. Flat bands in slightly twisted bilayer graphene: Tight-binding calculations. *Phys. Rev. B*, 82:121407, Sep 2010.

[8] Yuan Cao, Valla Fatemi, Shiang Fang, Kenji Watanabe, Takashi Taniguchi, Efthimios Kaxiras, and Pablo Jarillo-Herrero. Unconventional superconductivity in magic-angle graphene superlattices. *Nature*, 556(7699):43–50, March 2018.

[9] W_P Su, JR Schrieffer, and Ao J Heeger. Solitons in polyacetylene. *Physical review letters*, 42(25):1698, 1979.

[10] Yuanbo Zhang, Tsung-Ta Tang, Caglar Girit, Zhao Hao, Michael C. Martin, Alex Zettl, Michael F. Crommie, Y. Ron Shen, and Feng Wang. Direct observation of a widely tunable bandgap in bilayer graphene. *Nature*, 459(7248):820–823, 2009.

[11] Ferdinand Kisslinger, Christian Ott, Christian Heide, Erik Kampert, Benjamin Butz, Erdmann Spiecker, Sam Shallcross, and Heiko B Weber. Linear magnetoresistance in mosaic-like bilayer graphene. *Nature Physics*, 11(8):650, 2015.

[12] Peter Rickhaus, John Wallbank, Sergey Slizovskiy, Riccardo Pisoni, Hiske Overweg, Yongjin Lee, Marius Eich, Ming-Hao Liu, Kenji Watanabe, Takashi Taniguchi, et al. Transport through a network of topological channels in twisted bilayer graphene. *Nano letters*, 18(11):6725–6730, 2018.

[13] Yasuhiro Hatsugai. Edge states in the integer quantum Hall effect and the Riemann surface of the Bloch function. *Physical Review B*, 48(16):11851–11862, October 1993.

[14] Dong-Keun Ki and Hu-Jong Lee. Quantum Hall resistances of a multiterminal top-gated graphene device. *Physical Review B*, 79(19), May 2009.

[15] Zhong Wang and Shou-Cheng Zhang. Simplified topological invariants for interacting insulators. *Physical Review X*, 2(3), August 2012.

[16] Zhidan Li and Qiang Han. Topological invariants in terms of Green's function for the interacting Kitaev chain. *arXiv:1805.02537 [cond-mat]*, May 2018.

[17] Jun-Hui Zheng and Walter Hofstetter. Topological invariant for two-dimensional open systems. *Physical Review B*, 97(19), May 2018.

[18] Julio Cesar Avila, Hermann Schulz-Baldes, and Carlos Villegas-Blas. Topological invariants of edge states for periodic two-dimensional models. *Mathematical Physics, Analysis and Geometry*, 16(2):137–170, June 2013.

[19] Yasuhiro Hatsugai. Chern number and edge states in the integer quantum Hall effect. *Physical Review Letters*, 71(22):3697–3700, November 1993.

[20] Takahiro Fukui, Yasuhiro Hatsugai, and Hiroshi Suzuki. Chern Numbers in Discretized Brillouin Zone: Efficient Method of Computing (Spin) Hall Conductances. *Journal of the Physical Society of Japan*, 74(6):1674–1677, June 2005.

[21] Christoph W Groth, Michael Wimmer, Anton R Akhmerov, and Xavier Waintal. Kwant: a software package for quantum transport. *New Journal of Physics*, 16(6):063065, 2014.

[22] L. V. Keldysh. Diagram technique for nonequilibrium processes, 1964.

[23] J. Rammer and H. Smith. Quantum field-theoretical methods in transport theory of metals. *Reviews of Modern Physics*, 58(2):323–359, April 1986.

[24] Alessandro Cresti, Riccardo Farchioni, Giuseppe Grosso, and Giuseppe Pastori Parravicini. Keldysh-Green function formalism for current profiles in mesoscopic systems. *Physical Review B*, 68(7), August 2003.

[25] Stefan Rotter, Jian-Zhi Tang, Ludger Wirtz, Johannes Trost, and Joachim Burgdörfer. Modular recursive Green's function method for ballistic quantum transport. *Physical Review B*, 62(3):1950–1960, July 2000.

[26] Alexey A. Soluyanov and David Vanderbilt. Computing topological invariants without inversion symmetry. *Phys. Rev. B*, 83:235401, Jun 2011.

[27] Daniele Toniolo. On the equivalence of the Bott index and the Chern number on a torus, and the quantization of the Hall conductivity with a real space Kubo formula. *arXiv e-prints*, page arXiv:1708.05912, Aug 2017.

[28] Gerald D Mahan. *Many-particle physics*. Springer Science & Business Media, 2013.

[29] Murray Gell-Mann and Francis Low. Bound states in quantum field theory. *Physical Review*, 84(2):350, 1951.

[30] Hartmut Haug and Antti-Pekka Jauho. *Quantum kinetics in transport and optics of semiconductors*, volume 2. Springer, 2008.

[31] Takeo Matsubara. A new approach to quantum-statistical mechanics. *Progress of theoretical physics*, 14(4):351–378, 1955.

[32] Ho-Fai Cheung, Yuval Gefen, Eberhard K Riedel, and Wei-Heng Shih. Persistent currents in small one-dimensional metal rings. *Physical Review B*, 37(11):6050, 1988.

[33] Caio H Lewenkopf and Eduardo R Mucciolo. The recursive green's function method for graphene. *Journal of Computational Electronics*, 12(2):203–231, 2013.

[34] Kyryl Kazymyrenko and Xavier Waintal. Knitting algorithm for calculating green functions in quantum systems. *Physical Review B*, 77(11):115119, 2008.

[35] Dan Erik Petersen, Hans Henrik B Sørensen, Per Christian Hansen, Stig Skelboe, and Kurt Stokbro. Block tridiagonal matrix inversion and fast transmission calculations. *Journal of Computational Physics*, 227(6):3174–3190, 2008.

[36] DH Lee and JD Joannopoulos. Simple scheme for surface-band calculations. ii. the green's function. *Physical Review B*, 23(10):4997, 1981.

[37] MP Lopez Sancho, JM Lopez Sancho, JM Lopez Sancho, and J Rubio. Highly convergent schemes for the calculation of bulk and surface green functions. *Journal of Physics F: Metal Physics*, 15(4):851, 1985.

[38] Françoise Tisseur and Karl Meerbergen. The quadratic eigenvalue problem. *SIAM review*, 43(2):235–286, 2001.

[39] PA Khomyakov, G Brocks, Volodymyr Karpan, M Zwierzycki, and Paul J Kelly. Conductance calculations for quantum wires and interfaces: Mode matching and green's functions. *Physical Review B*, 72(3):035450, 2005.

[40] Hans Henrik B Sørensen, Per Christian Hansen, Dan Erik Petersen, Stig Skelboe, and Kurt Stokbro. Krylov subspace method for evaluating the self-energy matrices in electron transport calculations. *Physical Review B*, 77(15):155301, 2008.

[41] Petr A Khomyakov and Geert Brocks. Real-space finite-difference method for conductance calculations. *Physical Review B*, 70(19):195402, 2004.

[42] P. A. Khomyakov, G. Brocks, V. Karpan, M. Zwierzycki, and P. J. Kelly. Conductance calculations for quantum wires and interfaces: Mode matching and green's functions. *Phys. Rev. B*, 72:035450, Jul 2005.

[43] Klaus von Klitzing. The quantized hall effect. *Rev. Mod. Phys.*, 58:519–531, Jul 1986.

[44] E. Witten. Three lectures on topological phases of matter. *Nuovo Cimento Rivista Serie*, 39(7):313–370, Jul 2016.

[45] Roger S. K. Mong and Vasudha Shivamoggi. Edge states and the bulk-boundary correspondence in dirac hamiltonians. *Phys. Rev. B*, 83:125109, Mar 2011.

[46] Takahiro Fukui, Ken Shiozaki, Takanori Fujiwara, and Satoshi Fujimoto. Bulk-edge correspondence for chern topological phases: A viewpoint from a generalized index theorem. *Journal of the Physical Society of Japan*, 81(11):114602, 2012.

[47] Jeffrey C. Y. Teo and C. L. Kane. Topological defects and gapless modes in insulators and superconductors. *Phys. Rev. B*, 82:115120, Sep 2010.

[48] Terry A. Loring. K-theory and pseudospectra for topological insulators. *Annals of Physics*, 356:383 – 416, 2015.

[49] Dominik Gresch, Gabriel Autès, Oleg V. Yazyev, Matthias Troyer, David Vanderbilt, B. Andrei Bernevig, and Alexey A. Soluyanov. Z2pack: Numerical implementation of hybrid wannier centers for identifying topological materials. *Phys. Rev. B*, 95:075146, Feb 2017.

[50] Terry A. Loring. A Guide to the Bott Index and Localizer Index. *arXiv e-prints*, page arXiv:1907.11791, Jul 2019.

[51] Daniele Toniolo. On the equivalence of the Bott index and the Chern number on a torus, and the quantization of the Hall conductivity with a real space Kubo formula. *arXiv e-prints*, page arXiv:1708.05912, Aug 2017.

[52] Topological aspects of band theory. 2012.

[53] F Duncan M Haldane. Model for a quantum hall effect without landau levels: Condensed-matter realization of the" parity anomaly". *Physical review letters*, 61(18):2015, 1988.

[54] Pekka Koskinen, Sami Malola, and Hannu Häkkinen. Evidence for graphene edges beyond zigzag and armchair. *Physical Review B*, 80(7):073401, 2009.

[55] DA Bahamon, ALC Pereira, and PA Schulz. Third edge for a graphene nanoribbon: a tight-binding model calculation. *Physical Review B*, 83(15):155436, 2011.

[56] VP Gusynin and SG Sharapov. Unconventional integer quantum hall effect in graphene. *Physical review letters*, 95(14):146801, 2005.

[57] Yuan Cao, Valla Fatemi, Shiang Fang, Kenji Watanabe, Takashi Taniguchi, Efthimios Kaxiras, and Pablo Jarillo-Herrero. Unconventional superconductivity in magic-angle graphene superlattices. *Nature*, 556(7699):43, 2018.

[58] Kostya S Novoselov, Edward McCann, SV Morozov, Vladimir I Fal'ko, MI Katsnelson, U Zeitler, D Jiang, F Schedin, and AK Geim. Unconventional quantum hall effect and berry's phase of 2π in bilayer graphene. *Nature physics*, 2(3):177, 2006.

[59] Pilkyung Moon and Mikito Koshino. Energy spectrum and quantum hall effect in twisted bilayer graphene. *Phys. Rev. B*, 85:195458, May 2012.

[60] Fan Zhang, Allan H MacDonald, and Eugene J Mele. Valley chern numbers and boundary modes in gapped bilayer graphene. *Proceedings of the National Academy of Sciences*, 110(26):10546–10551, 2013.

[61] Florian Speck, Markus Ostler, Jonas Röhrl, Johannes Jobst, Daniel Waldmann, Martin Hundhausen, Lothar Ley, Heiko B Weber, and Thomas Seyller. Quasi-freestanding graphene on sic (0001). In *Materials Science Forum*, volume 645, pages 629–632. Trans Tech Publ, 2010.

[62] Ch Riedl, C Coletti, T Iwasaki, AA Zakharov, and U Starke. Quasi-free-standing epitaxial graphene on sic obtained by hydrogen intercalation. *Physical review letters*, 103(24):246804, 2009.

[63] Jonathan S. Alden, Adam W. Tsen, Pinshane Y. Huang, Robert Hovden, Lola Brown, Jiwoong Park, David A. Muller, and Paul L. McEuen. Strain solitons and topological defects in bilayer graphene. *Proceedings of the National Academy of Sciences*, 110(28):11256–11260, 2013.

[64] Aryan Afzalian. Computationally efficient self-consistent born approximation treatments of phonon scattering for coupled-mode space non-equilibrium Green's function. *Journal of Applied Physics*, 110(9):094517, November 2011.

[65] Jesse A. Vaitkus and Jared H. Cole. B\"uttiker probes and the Recursive Green's Function; an efficient approach to include dissipation in general configurations. *Physical Review B*, 97(8), February 2018.

[66] Dmitri Nikonov, George Bourianoff, Paolo Gargini, and Himadri Pal. Scattering in NEGF: Made simple. page 54.

Acknowledgments

To structure the acknowledgments, define the following group assignment:

- Dr. Kai Phillip Schmidt: Professor.
- Max Hörmann: Work group and office neighbour.
- Sebastian Fey: Work group and office neighbour.
- Jan Koziol: Work group and office neighbour.
- Robert Weigel: Office neighbour.
- Felix Winterhalter: Office neighbour and admin.
- Johannes Hielscher: Admin.
- Mathias Walther: Work group.
- Mathias Mühlhauser: Work group.
- Patrick Adelhardt: Work group.
- Lea Lenke: Work group.
- Carolin Boos: Work group.

I thank the respective groups for

- Professor: Kai for his guidance and patience.
- Work group: For the very friendly atmosphere and discussions.
- Admin: For keeping things running and very friendly customer service.
- Office neighbour: For day to day discussions and entertainment, physical and nonphysical.

and of course everyone I forgot to mention for whatever there is to thank.

Erklärung

Ich versichere, dass ich meine Masterarbeit ohne Hilfe Dritter und ohne Benutzung anderer als der angegebenen Quellen und Hilfsmittel angefertigt habe und die aus benutzten Quellen wörtlich oder inhaltlich entnommenen Stellen als solche kenntlich gemacht habe. Diese Arbeit hat in gleicher oder ähnlicher Form noch keiner Prüfungsbehörde vorgelegen.

Erlangen, 13. März 2020

Nico S. Baßler